Master's thesis

NTNU
Norwegian University of Science and Technology
Faculty of Engineering
Department of Mechanical and Industrial Engineering

Jakob Deraas Grimsgaard

# Efficiency Testing of The Kindernay XIV Gearhub

## In Cooperation With Kindernay Corporation

Master's thesis in Engineering and ICT
Supervisor: Olav Egeland and Knut Tore Ljøsne
July 2020

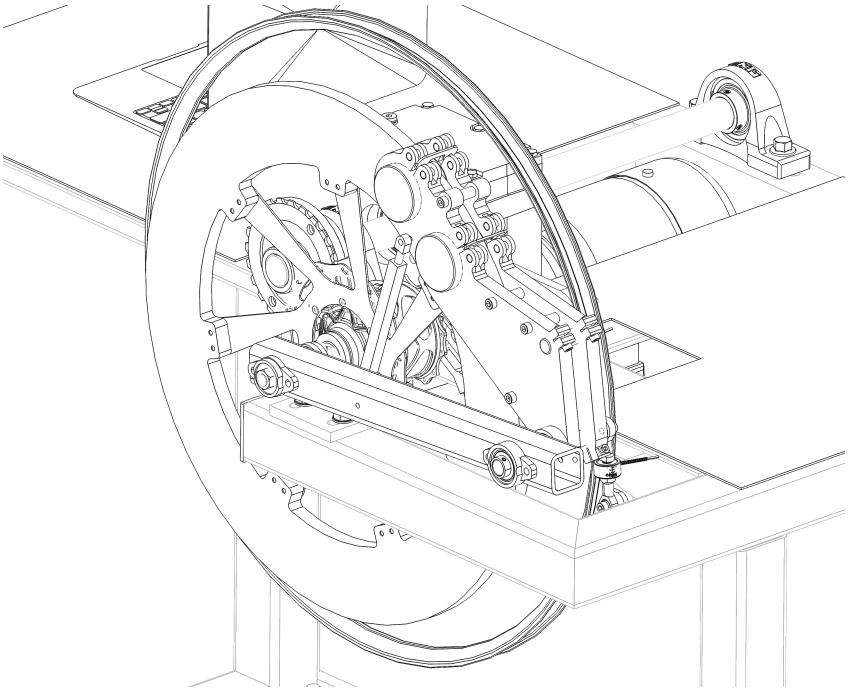

NTNU
Norwegian University of Science and Technology

Jakob Deraas Grimsgaard

# Efficiency Testing of The Kindernay XIV Gearhub

In Cooperation With Kindernay Corporation

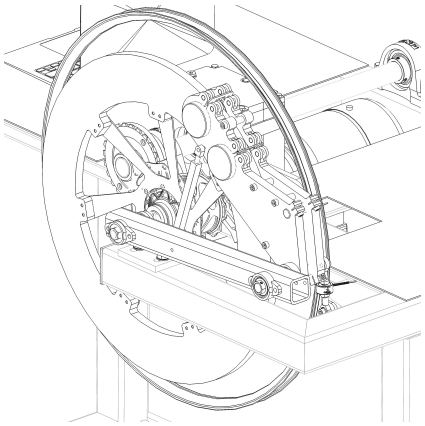

Master's thesis in Engineering and ICT
Supervisor: Olav Egeland and Knut Tore Ljøsne
July 2020

Norwegian University of Science and Technology
Faculty of Engineering
Department of Mechanical and Industrial Engineering

NTNU
Norwegian University of
Science and Technology

# Abstract

Drivetrain efficiency, defined as the power output divided by the power input, is an important measure in bicycle drivetrains and especially relevant in the field of bicycle gearhubs. CA Technology Systems is a Norwegian company specializing in bicycle gearhubs for regular and electric bicycles. The company started developing an efficiency testing rig together with a master student in 2018, but did not complete the rig to a functional state.

The present project was conducted from January to July of 2020 with the objectives of bringing the testing rig to a functional state, and test the efficiency of the Kindernay XIV gearhub. Through systematic troubleshooting of the original rig design, it became evident that the problems with the testing rig were more severe than first assumed. The previous belt transmission system from the gearhub to the braking system was unstable and disadvantageous in terms of compatibility with different rim sizes and profiles. While other solutions were explored, the troubleshooting clarified that a directly coupled braking system was favourable, as it was not dependent on the remaining wheel components.

Two direct mounted brake solutions were conceptualized and fabricated; a friction brake and an eddy current brake (ECB) with permanent magnets. Both braking systems were based on a large rotor diameter and a caliper pivoting around the center of the gearhub on a solid arm. The force measurement was done by attaching an axial force sensor to the arm. The caliper could be adjusted in the radial direction to allow for wheel removal and installation.

Testing showed that the friction brake was highly unstable, and was therefore not suited for the testing rig. The ECB was underpowered relative to the specified requirements, but superior in terms of stability and usability. It therefore became the preferred solution to be used in the subsequent efficiency testing.

The testing rig had constant losses resulting from the driving axle bearings and chain transmission. These losses were measured using a regular bicycle rearhub, with roller bearings whose dust covers and grease were removed prior to testing. The Kindernay XIV was tested at 100 W power with 60 rpm input cadence and 32/16 sprocket combination. The efficiency was obtained by subtracting the constant losses from the calculated gearhub losses, and ranged from 94.4% for 1st gear to 99.5% in 11th gear. The results correlated well with planetary drivetrain theory – the efficiency seemed to be dependent on the number of active planetary gear sets, as well as the rotational speed of the gearhub.

In summary, the results from the implemented improvements demonstrated that the testing rig has reached a high functional level, already of value to the company. Further work should include continued study and improvement of the ECB performance, as well as further automation of the control system to improve the usability of the testing procedure.

# Sammendrag

Drivverkstap er definert som utgående effekt dividert med inngående effekt, og er et viktig parameter for sykkeldrivverk og interne girnav. CA Technology Systems AS er et norsk firma som spesialiserer seg i utvikling og produksjon av girnav for trå- og el-sykler. Selskapet startet utviklingen av en testrigg for å måle effektivitetstap i samarbeid med en masterstudent i 2018, men fullførte ikke prosjektet.

Dette prosjektet ble gjennomført fra januar til juli 2020 med mål om å videreutvikle testriggen til funksjonell tilstand, og deretter teste effektiviteten til selskapets eget navgir, Kindernay XIV. Gjennom systematisk feilsøking av den opprinnelige testriggen viste det seg at problemene var forårsaket av flere undersystemer. Overføringen mellom sykkelhjulet og bremsesystemet var ustabil og hadde begrenset kompatibilitet med ulike felgstørrelser og profiler. Etter omfattende testing ble det derfor besluttet å konstruere et nytt, direktemontert bremsesystem.

To direktemonterte bremsekonsepter ble utviklet og fabrikkert; en friksjonsbrems og en virvelstrømsbrems med permanente magneter. Begge systemene var basert på stor skivediameter og en kalipper som roterte rundt akslingen til girnavet på en solid arm. Effektmåling ble gjort ved å måle kreftene på den roterende armen, og radiell justering av kalipperen muliggjorde rask installasjon av hjulet.

Testing viste at friksjonsbremsen hadde ustabil funksjon under last, og derfor var uegnet for testriggen. Virvelstrømsbremsen viste mindre effekt enn kravspesifikasjonen, men hadde til gjengjeld overlegen stabilitet og brukervennlighet sammenlignet med både det originale bremsesystemet og friksjonsbremsen. Virvelstrømsbremsen ble derfor brukt i den påfølgende effektivitetstestingen.

Testriggen hadde konstante tap relatert til flenslagerne for drivakslingen og den inngående kjedetransmisjonen. Disse tapene ble målt med et standard baknav for sykkel med maskinlager, hvor tetninger og fett ble fjernet for å minimere rullemotstand. Kindernay XIV ble testet på 100 W effekt med 60 rpm inngående kadens og en drevkombinasjon på 32/16. Effektiviteten ble kalkulert ved å trekke fra det konstante tapet til testriggen, og varierte da mellom 94.4% for 1. gir til 99.5% for 11. gir. Resultatene hadde god overenstemmelse med planetgir- og drivverksteori, da effektivitetsstapet så ut til å øke med antall aktive planetgir og rotasjonshastigheten til girnavet.

Oppsummert viste resultatene av de gjennomførte forbedringene at testriggen har nådd et høyt funksjonelt nivå og allerede er av verdi for bedriften. Videreutvikling bør ivareta ytterligere undersøkelser og forbedring av ytelsen til virvelstrømsbremsen, samt videre automatisering av kontrollsystemet for økt brukervennlighet.

# Preface

This thesis was written as part of the final delivery for the Master of Science degree in Engineering and ICT, with specialization in Product Development and Materials. The thesis was written during the spring semester of 2020 for the Department of Mechanical and Industrial Engineering at the Norwegian Institute of Science and Technology (NTNU), and is meant to represent a workload of 30 ECTS.

The thesis was done in cooperation with CA Technology Systems AS, a Norwegian company based in Oslo. The subject and scope of the project were defined in collaboration with my company supervisor Knut Tore Ljøsne and my supervisor at NTNU, Olav Egeland. I would like to thank you both for helpful advice and solid guidance throughout the semester.

As the subject was of a practical nature, a large part of the thesis work was conducted and written at the company premises in Oslo. This has given me invaluable insight into the inner workings of an ambitious startup company, with an undoubtedly bright future. A special thanks is therefore directed to the company founder Christian Antal and the employees at CA-Tech for giving me this opportunity.

# Contents

# List of Figures

# List of Tables

## Abbreviations

| Abbreviation | Description |
|---|---|
| ABS | Anti-lock Braking System |
| CVT | Continously variable transmission |
| DAQ | Data aquisition device |
| DOF | Degree of freedom |
| ECB | Eddy current brake |
| ELCB | Earth leakage circuit breaker |
| FEA | Finite element analysis |
| FEM | Finite element model |
| ISO | International Organization for Standardization |
| IS | International standard |
| ISD | Sensorless current vector control |
| MIG | Metal inert gas |
| MTB | Mountain Bike |
| NI | National Instruments |
| NOK | Norwegian krone |
| RBE | Rigid body element |
| TIG | Tungsten inert gas |
| VFC | Voltage governed flux |
| VI | LabView Virtual Instrument |

# Chapter 1

# Introduction

This chapter gives a brief introduction to the background and motivation of the master project and its stakeholders.

## 1.1 Background

With increased focus on micro-mobility and environmentally friendly transport, the bicycle is becoming an essential commuting aid for many people. Recent advantages in battery technology has expanded the market to also include electric bicycles, making commuting on two wheels a desirable option for more people than before.

Electric bicycles can easily triple the power of an average commuting cyclist, and therefore puts increasing stress on drivetrain components. This is especially true for external gear systems that are exposed to the environment. Combined with frequent use, often also in the winter months, drivetrain longevity and reliability has become an increasing problem. External drivetrains on electric bicycles therefore require more maintenance than any other components on the bicycle.

In contrast to external gear systems, bicycle gearhubs are situated in the rear wheel and offer different gear speeds by actuating an internal mechanism. Gearhubs are therefore protected from the external environment and usually see increased longevity and reliability. The primary market for gearhubs was for a long time centered around city and commuting bicycles with high weight and slow performance. Today, the improved reliability that gearhubs offer is becoming increasingly attractive in the electrical bicycle market.

The adoption of gearhubs to electric bicycles has not been without issues, however – the problem with many common gearhubs is their limited torque capacity. This is due to the fact that most gearhubs on the market build on old technology that was developed long before the dawn of electric bicycles, and therefore with limited torque demands.

In contrast to derailleur systems, gearhubs tend to have larger efficiency variations for the different gears. The variations don't necessarily follow the change in gear ratio, but rather depend on the active internal mechanisms in each gear. The efficiency loss of the hub is added on top of the chain- or belt-transmission from the pedals to the rear wheel. The total drivetrain efficiency of bicycles with gearhubs is therefore worse compared to bicycles with external drivetrains.

For this reason, the manufacturers, and often also the customers, are interested in knowing the

efficiency data for a gearhub system. Because the efficiency losses are on the order of a few percent, accurate efficiency measurements require high accuracy testing equipment because of the small relative differences in power output.

This project was done in cooperation with CA Technology Systems AS who proposed the subject of the project. The author has been working as a trainee engineer for the company since the spring of 2019, primarily assembling, testing and participating in the development of the gearhub. This has provided valuable insight into the world of bicycle gearhubs and their function on regular and electric bicycles.

## 1.2 Company introduction

CA Technology Systems AS is a Norwegian company that specializes in bicycle gear hubs for regular and electric bicycles. The company has 10 employees and is situated in Stanseveien 16, Oslo. The company founder Christian Antal had long envisioned a more robust drivetrain solution for bicycles, after being continuously frustrated with the poor reliability of external drivetrain products. He therefore engaged engineer Knut Tore Ljøsne, and in 2010 they started the company.

The first prototype gearhub came together in 2012 and the first production gearhubs started shipping in early 2019, after being through multiple testing regimes. Today, the company has a running production and is also engaged in developing future drivetrain solutions for regular- and electric bicycles. The company's facilities in Oslo combines gearhub assembly and servicing, R&D engineering as well as sales and marketing.

## 1.3 Objectives and research questions

The company has together with a previous master student started the development an electromechanical testing rig for efficiency testing purposes. The testing rig is not complete, and has issues related to instability, compatibility and performance. It therefore needs hardware and software improvements to deliver results that can be used for future development and commercial applications. When in operation, the testing rig should be used to compute efficiency data for company products like the Kindernay XIV gear hub, as well as new prototypes and competitive solutions.

The project scope was defined in early January of 2020 together with the company, and included the following objectives:

- **Objective 1:** Investigate the functionality of the current testing rig and determine areas of improvement.
  - *Research Question 1.1:* Which subsystems cause the observed instability and compatibility issues?
  - *Research Question 1.2:* How can these subsystems be improved?
- **Objective 2:** Improve or redesign the necessary subsystems such that the necessary performance, stability and compatibility requirements are satisfied.
  - *Research Question 2.1:* How can the in-going and out-going power be measured in an accurate and repeatable manner?

  - *Research Question 2.2:* Which requirements are necessary to ensure compatibility with the most common gearhub systems on the market?
  - *Research Question 2.3:* How can the suggested solutions be implemented in accordance with these requirements?

- **Objective 3:** Develop a control system where the user can test and verify gear hub efficiency in a straightforward manner.
  - *Research Question 3.1:* How is the control system hardware coupled together?
  - *Research Question 3.2:* How should the testing rig be calibrated to deliver accurate results?
  - *Research Question 3.3:* How is the testing rig accuracy affected by the measuring equipment?

- **Objective 4:** Produce and verify efficiency data for the Kindernay XIV.
  - *Research Question 4.1:* How can mechanical losses in the testing rig be accounted for?
  - *Research Question 4.2:* How does the gearhub efficiency vary in different gears of the gearhub?
  - *Research Question 4.3:* Why does the gearhub efficiency vary in different gears of the gearhub?

## 1.4 Project process

The process stages of the project are illustrated in Figure 1.1, and can be described as follows:

1. Theory and background: Relevant theory of bicycle drivetrains, gearhubs and planetary transmissions will be studied to better understand the mechanisms in the Kindernay XIV gearhub.
2. Requirements analysis: A new requirement analysis will be performed based on considerations from the previous master project, relevant gearhubs for testing and other relevant requirements
3. Function test: A function test will be performed on the original testing rig setup to evaluate the performance of its subsystems compared to the requirements defined previously.
4. Solution selection: With basis in the findings from the function test, solutions to improve the testing rig will be considered and decided upon.
5. Solution implementation: The selected solutions will be conceptualized with respect to the design space resulting from the previous requirement analysis
6. Fabrication and assembly: The individual components resulting from the previous process will then be manufactured, assembled and installed
7. Function test 2: The second function test will evaluate the implemented solutions versus the requirements. Depending on the outcome, the process may iterate back to the solution processes to further improve one or more subsystems
8. Control system implementation: Because the control system depends on the design of the solutions defined previously, it will be implemented after the functionality of the testing rig is verified.

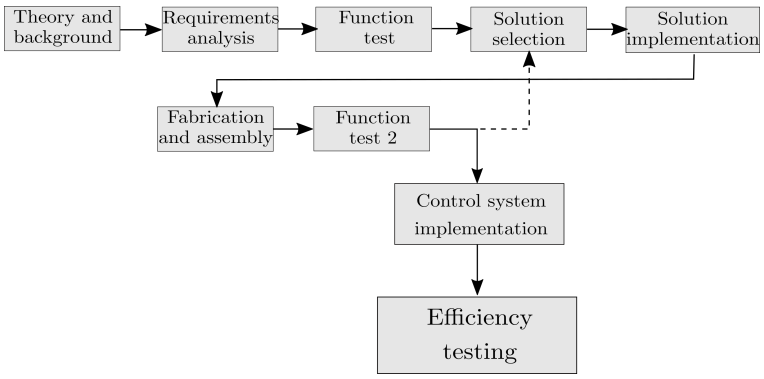


**Figure 1.1:** The process stages of the specialization and master project.

9. Gearhub efficiency testing: The gearhub efficiency testing will be performed once the rig is in operational order

### 1.4.1 Project plan

The project processes were divided into more detailed tasks and compiled in a project plan, shown in Figure 1.2. The completion status for each task was updated to keep track of progress during the project. The project plan was revised several times due to component delivery delays caused by the covid-19 situation that unfolded during the spring and summer. Originally, it was planned to test multiple and different gearhub systems, but because central components for the control system were received late in the project period there was little time for optimizing the testing rig and perform efficiency tests.

| | Month | Januar | | | | Februar | | | Mars | | | | | | April | | | | Mai | | | | Juni | |
|---|---|---|---|---|---|---|---|---|---|---|---|---|---|---|---|---|---|---|---|---|---|---|---|---|
| Task | Status (%) | 2 | 3 | 4 | 5 | 6 | 7 | 8 | 9 | 10 | 11 | 12 | 13 | 14 | 15 | 16 | 17 | 18 | 19 | 20 | 21 | 22 | 23 | 24 |
| T1 Project start | 100% | | | | | | | | | | | | | | | | | | | | | | | |
| T2 Parts fabrication | 60% | | | | | | | | | | | | | | | | | | | | | | | |
| T3 Thesis: Structure | 100% | | | | | | | | | | | | | | | | | | | | | | | |
| T4 Control system planning | 100% | | | | | | | | | | | | | | | | | | | | | | | |
| T5 Rig assembly | 70% | | | | | | | | | | | | | | | | | | | | | | | |
| T6 Thesis: Theory section | 20% | | | | | | | | | | | | | | | | | | | | | | | |
| T7 Rig calibration/testing | 0% | | | | | | MS1 | | | | | | | | | | | | | | | | | |
| T8 Time buffer 1 (rig) | 0% | | | | | | | | | | | | | | | | | | | | | | | |
| T9 Thesis: Method | 0% | | | | | | | | | | | | | | | | | | | | | | | |
| T10 Control system implementation | 0% | | | | | | | | | | | | | | | | | | | | | | | |
| T11 Final calibration and testing | 0% | | | | | | | | | | | | MS2 | | | | | | | | | | | |
| T12 Test protocol planning | 0% | | | | | | | | | | | | | | | | | | | | | | | |
| T13 Adapter components fabrication | 0% | | | | | | | | | | | | | | | | | | | | | | | |
| T14 Gearhub testing | 0% | | | | | | | | | | | | | | | | | | | | | | | |
| T15 Results analysis | 0% | | | | | | | | | | | | | | | | MS3 | | | | | | | |
| T16 Thesis: Results and discussion | 0% | | | | | | | | | | | | | | | | | | | | | | | |
| T17 Thesis: Conclusion | 0% | | | | | | | | | | | | | | | | | | | | | | | |
| T18 Complete thesis | 0% | | | | | | | | | | | | | | | | | | MS4 | | | | | |
| T19 Proofreading | 0% | | | | | | | | | | | | | | | | | | | | | | | |
| T20 Time buffer 2 | 0% | | | | | | | | | | | | | | | | | | | | | | | |
| T21 TMM4112 Exam preparations | 0% | | | | | | | | | | | | | | | | | | | | | | | |
| T22 Final delivery | 0% | | | | | | | | | | | | | | | | | | | | | | | MS5 |

**Figure 1.2:** The project plan for the master project.

# Chapter 2

# Theory and background

This chapter gives an overview of relevant theory behind efficiency testing, as well as the technical fundamentals behind modern bicycle gearhubs. The mechanisms behind the Kindernay XIV gearhub is analyzed in detail, and hypotheses on the expected efficiencies in various gears are given based on the resulting findings. An analysis of previous gearhub studies is also outlined, along with the current testing equipment.

## 2.1 Efficiency in drivetrains

Figure 2.1 shows a basic relationship that can be related to many modern vehicles and machines, with a powerplant (input), transmission and output. Because the powerplant often has a limited speed interval, a transmission can be used to vary the output speed from the input speed and thereby moving, or extending, the output speed interval. In its most basic form, a transmission consists of a housing and two external shafts (input and output) which are internally connected through a gear mechanism.

Considering the simple single-ratio transmission in Figure 2.2, the most important characteristic is the speed ratio. It is defined as:

$$i = \frac{\omega_1}{\omega_2} = \text{const.} \tag{2.1}$$

with $\omega_1$ and $\omega_2$ being the speed of the input and output shaft, respectively. If the output shaft

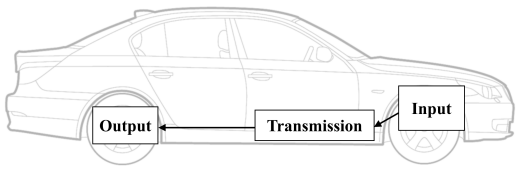


**Figure 2.1:** A vehicle with a motor (input), a transmission and an output.

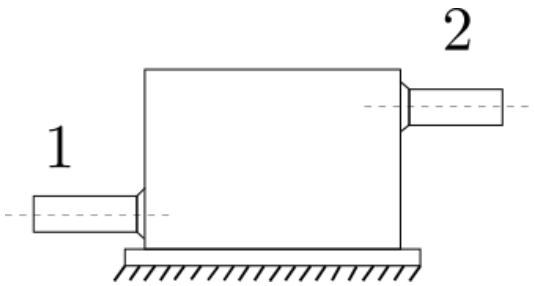


**Figure 2.2:** A simple single-ratio transmission with the input shaft (1) and output shaft (2).

has an opposite direction of rotation from the input shaft, this is indicated with negative sign, $-\omega_2$. Most modern vehicles have multi-ratio transmissions with multiple different speed ratios. For example, an 8-speed transmission has eight different speed ratios and is therefore not only moving the output speed range, but also expanding it.

Another important characteristic of a transmission is the ratio of the torque which is acting on the external shaft. The following is true about the torque on a rotating shaft:

- If a shaft is driven (for instance a transmission input shaft), the torque is acting in the same direction as the shaft rotation
- If a shaft is driving (for instance a transmission output shaft), the torque is acting in the opposite direction of the shaft rotation

We define the power being transmitted through a shaft as

$$P = \tau_{\text{shaft}} \cdot \omega_{\text{shaft}} \tag{2.2}$$

where $\tau$ and $\omega$ denotes the torque in Nm and rotational speed in rad/s, respectively.

Müller [1] defines the sum of all input powers as

$$\sum P = P_1 + P_2 + P_L \tag{2.3}$$

where $P_1$ and $P_2$ are the powers of the input and output shaft respectively, and $P_L$ designates the power loss in the transmission. Thus, considering the above principles, the input power becomes positive and the output power and power loss becomes negative, cancelling each other out. This is in agreement with the principle of energy conservation, stating that the sum of all input powers for a system in an equilibrium state is zero [2]. Hence, the ratio of the external shaft torques can be calculated on the basis of the transmission speed ratio and the mechanical efficiency.

In its most basic form, the mechanical efficiency is simply the measure between power input and power output, or

$$\eta = \frac{-P_{\text{in}} - P_L}{P_{\text{in}}} = \frac{-P_{\text{out}}}{P_{\text{in}}} = \frac{-\tau_{\text{out}} \cdot \omega_{\text{out}}}{\tau_{\text{in}} \cdot \omega_{\text{in}}} \tag{2.4}$$

In multistage transmissions, where the power flows in series through multiple stages $1 \rightarrow n$, the power loss is the sum of the power losses that occur in each stage, or

**Figure 2.3:** A chain-derailleur transmission on a road bicycle. Picture from road.cc [3].

$$P_L = P_{L_1} + P_{L_2} + P_{L_n} \tag{2.5}$$

The overall mechanical efficiency $\eta_{\text{tot}}$ can then be defined as

$$\eta_{\text{tot}} = \frac{-P_{\text{out}}}{P_{\text{in}}} = \frac{-P_{\text{out}_1}}{P_{\text{in}_1}} \cdot \frac{-P_{\text{out}_2}}{P_{\text{in}_2}} \cdot \frac{-P_{\text{out}_n}}{P_{\text{in}_n}} \tag{2.6}$$

In other words, the overall mechanical efficiency describes the total energy loss between the input and output of the transmission, usually dissipated as heat because of various friction losses. In a car this can impact gas mileage and on a bicycle it simply affects the average speed and/or the battery capacity, the latter if considering an electric bicycle.

### 2.1.1 Bicycle drivetrains

Drivetrain systems on modern bicycles have become increasingly complex, and can be divided into the following categories:

- Chain-derailleur transmissions
- Internal gearhub transmissions
- Internal gearbox transmissions

The chain-derailleur transmission, shown in Figure 2.3, is found on most modern bicycles. It consists of multiple sprockets with different tooth counts, and a derailleur to move the chain between the sprockets to obtain different gearing ratios. Chain-derailleur systems are recognized as very efficient in their basic form and Spicer et al. [2000] found the efficiency of generally around 98% [5], but also dependant on:

- The selected gear and resulting chainline (straight chainline yields better efficiency)
- The size of the sprockets (larger sprockets yields better efficiency)

Internal gearhub and gearbox systems differ from chain-derailleur transmissions in that the transmission mechanisms are internal. These systems often rely on the similar technical principles, but differ in the physical location on the bicycle – the gearhub is part of the rear wheel, whereas the gearbox is a part of the bicycle frame, as shown in Figure 2.4. Bicycle gearhubs are therefore highly universal, as they can be fitted to most rear frame dropouts. Gearboxes on the other hand, require


(a) (b)

**Figure 2.4:** Comparison of bicycle gearhub and gearbox.

specially developed frames with gearbox mounting points. The following discussion will therefore be centered around bicycle gearhubs, although much of the following discussion also applies for bicycle gearboxes.

Bicycle gearhubs and gearboxes are known to be less efficient than derailleur transmissions, simply because of the additional losses from internal mechanisms that are added on top of the losses from the chain transmission:

$$P_L = P_{\text{L,gearbox}} + P_{\text{L,chain}} \tag{2.7}$$

The efficiency data for a given gearhub or gearbox is therefore an important attribute and something that customers often value in a decision making process.

Relative to the aforementioned nomenclature, most bicycle gearhubs and gearboxes are both multi-ratio and multi-stage. The power loss in the gearhub or gearbox, $P_{\text{L,gearbox}}$, is therefore not constant across all gear ratios because different stages of mechanisms are acting in different gears. Hence, the efficiency of a bicycle gearhub cannot be described by a single number.

Bicycle gearhubs come in many variants, some with up to 14 gear speeds and consequently wide gear ranges over 500%. The combination of wide gear ranges and strict spacial constraints put great demands on the internal mechanisms in bicycle gearhubs. Most bicycle gearhubs therefore rely on the principle of epicyclic gearing, which allows for tight packing of multiple gear ratios and shifting mechanisms in limited space, whilst maintaining the necessary torque capacity.

The theory behind epicyclic gearing will therefore be discussed next.

## 2.2 Epicyclic gearing

For the equilibrium conditions of an object to be satisfied, the total forces and total torque acting on the object must equal zero. Consider again equation 2.2 and 2.4. For a drivetrain with gear ratio $i \neq 1$, the torques on the input and output shafts are not equal.

This implies that there is a residual torque $\tau_R$ acting on the transmission housing so that

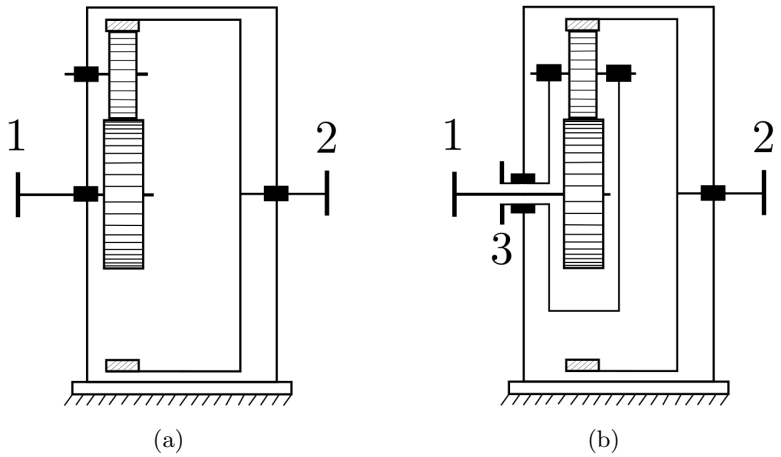


**Figure 2.5:** The evolution of a simple single-ratio transmission with two shafts (a) to a simple planetary transmission with three shafts (b).

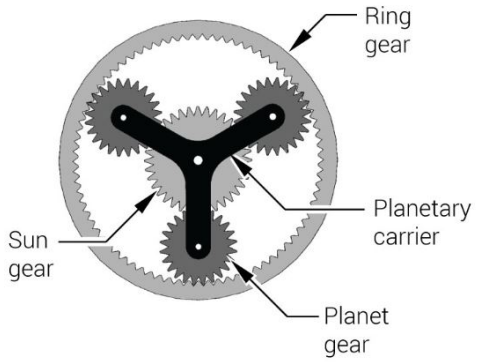


**Figure 2.6:** The main components of a planetary gear set [6].

$$\sum \tau = \tau_1 + \tau_2 + \tau_R \tag{2.8}$$

If the transmission housing is instead allowed to rotate around a concentric axis, it effectively becomes a third shaft that can transfer power, as shown in Figure 2.5. Actual planetary transmissions originate from this principle, and have three main components, as shown in Figure 2.6:

1. The central "sun gear"
2. The planet carrier with planet gears
3. The ring gear

The planet carrier is essentially the rotating gear housing, but is reduced to a carrier that only supports the planet shafts. The planets connect the sun gear with the ring gear, effectively enclosing the gear mechanism in a housing which does not require a support.

The revolving planets are usually arranged symmetrically so that the rotating mass does not cause imbalance. The power transfer from the sun gear to the ring gear is therefore distributed between several planets.

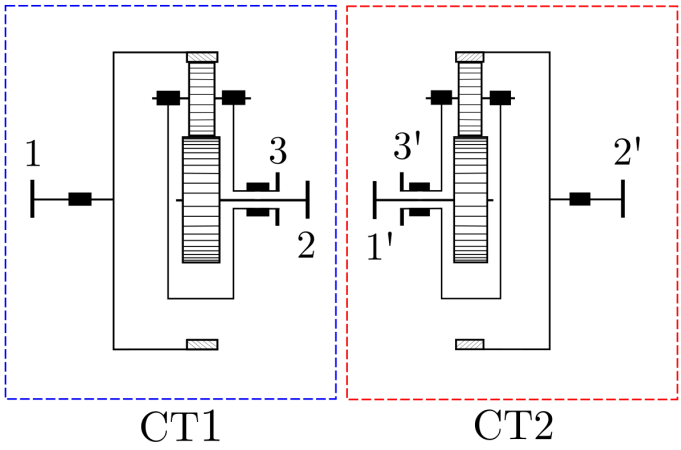


**Figure 2.7:** The main components of a planetary gear set [6].

### 2.2.1 Degrees of freedom

The degree of freedom (DOF) for a transmission indicates the number of independent variables that must be specified in order to describe the state of the system, as defined by Müller [1]. Considering again the simple transmission in Figure 2.2, the transmission has only one degree of freedom, namely the shaft speed.

In a planetary transmission, the previous gear housing becomes a third shaft, effectively adding another degree of freedom. The degree of freedom can be reduced to one in two ways, namely:

1. By constraining some of the shafts to a fixed housing
2. By linking some of the shafts to each other

Building on this theory, a compound transmission consisting of two planetary gear sets, as shown in Figure 2.7, with a total of four DOF's can be reduced to one DOF with the above methods, given that they are coupled. Hence, the degree of freedom for a compound transmission can be defined as

$$F = \sum F_i - h - l \tag{2.9}$$

where $F_i$ is the degree of freedom for the i'th component transmission, $h$ and $l$ is the number of constraints and linkages, respectively.

### 2.2.2 Efficiency planetary transmissions

It is often assumed that the basic efficiency for a transmission is independent of the direction of power flow [1], so that

$$\eta = \eta_{12} = \eta_{21} \tag{2.10}$$

where 1 and 2 designates the input and output shafts, respectively. Actual efficiency measurements on basic transmissions indicate that the total power loss $P_L$ from equation 2.4 has several contributing factors [1]:

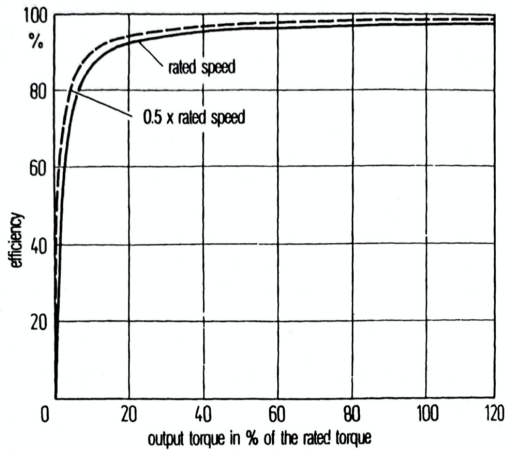


**Figure 2.8:** Efficiency as a function of output torque for a heavy duty planetary transmission. Illustration borrowed from Müller [1].

$$P_L = P_{\text{L,load}} + P_{\text{L,idle}} \tag{2.11}$$

where $P_{\text{L,load}}$ is the load dependent part that mainly consists of the tooth friction losses. $P_{\text{L,idle}}$ on the other hand represents the no-load, or idling losses. The idling losses can be further separated into constant losses and speed dependant losses, like ventilation and splash losses.

Hence, the efficiency for a given gear combination is therefore rarely constant, but dependant on the load on the transmission and the speed it is running at. Depending on the no-load losses, the efficiency may even decrease to a theoretical zero with decreasing output torque.

According to Müller [1], planetary transmissions have two additional sources of losses:

- Speed-dependant ventilation and splash losses caused by the planet carrier motion
- Speed- and load-dependant friction losses in the planet bearings caused by centrifugal forces

If considering roller planet bearings, the losses are minor and can normally be neglected. Still, planetary transmissions are expected to have differing no-load losses compared to conventional transmissions. Calculating efficiency for planetary transmissions therefore involve a larger measure of uncertainty compared to conventional transmissions. As depicted in Figure 2.8, we can assume that:

- The efficiency increases with increasing torque, as the magnitude of the constant no-load losses become smaller
- The efficiency decreases with increasing speed because of the ventilation/splash losses and planet bearing losses
- For a given speed, the efficiency stabilizes at a limit $\eta_{\text{lim}}$ when $\tau_{\text{input}} \longrightarrow \infty$

The aforementioned theory is highly relevant when studying the internals of the Kindernay XIV gearhub, which is presented in the following.

## 2.3 The Kindernay XIV gearhub

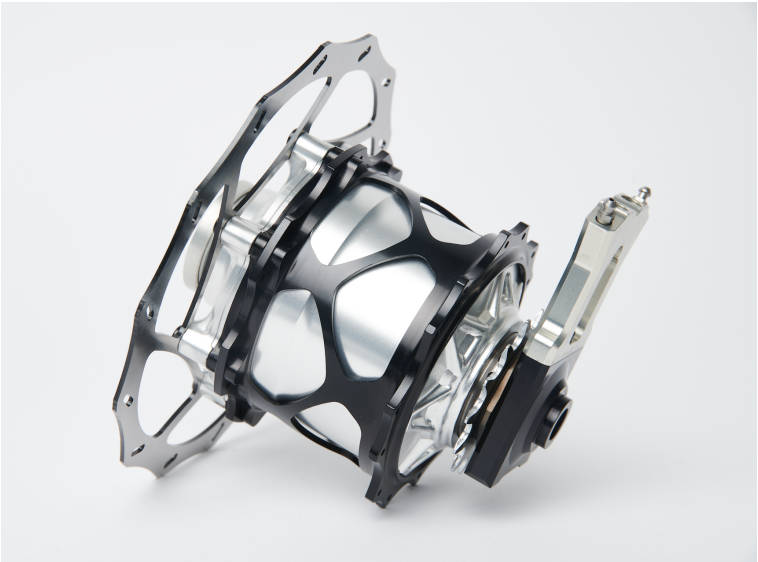

**Figure 2.9:** The Kindernay XIV gearhub, shown with its hub cage and shifting actuator.

An important part in working with drivetrain efficiency is knowledge about the working mechanisms between input and output. In case of the Kindernay XIV, this comes down to the internal mechanism of the gearhub. An overview of the gearhub's features and its internal mechanisms is therefore given next.

The Kindernay XIV gearhub is situated in the rear wheel and offers 14 gears, hydraulically controlled from two shifters at the handlebar. The gearhub is one of few gearhubs on the market that is properly dimensioned for the increased torque from electric bicycles. It is a maintenance free, "set and forget" solution. In contrast, external derailleur systems found on today's e-bikes are exposed, unreliable and fast-wearing.

As shown in Figure 2.9, the Kindernay XIV gearhub has a single speed cog on the right side that is driven by a bicycle chain, similar to a chain-derailleur transmission. By shifting the internal mechanisms, the rider can regulate the rotational speed of the gearhub housing (and therefore also the wheel) versus the input cog.

Like most gearhubs, the Kindernay XIV relies on the principle of multiple planetary gear sets. The basic principle behind the internal mechanisms in the Kindernay XIV is three planetary gear sets in series between the input (single speed cog) and output (gearhub housing). By regulating the input and output of the first two planetary gear sets, one can achieve seven speeds. The last planetary gear is used as a reduction gear, thus doubling the number of combinations to obtain 14 gear speeds. Hence, the reduction gear is enabled during the first seven (easiest) gears and disabled for the last seven gears.

Using the terminology from section 2.2, we can divide the first two planetary series into two component transmissions, CT1 and CT2, as shown in Figure 2.10. The letters A-C designate the shafts for CT1, and D-F for CT2. If first treating the input transmissions as separate entities, we see that each transmission has a total of two degrees of freedom:

- DOF1: Input speed (on desired input shaft)

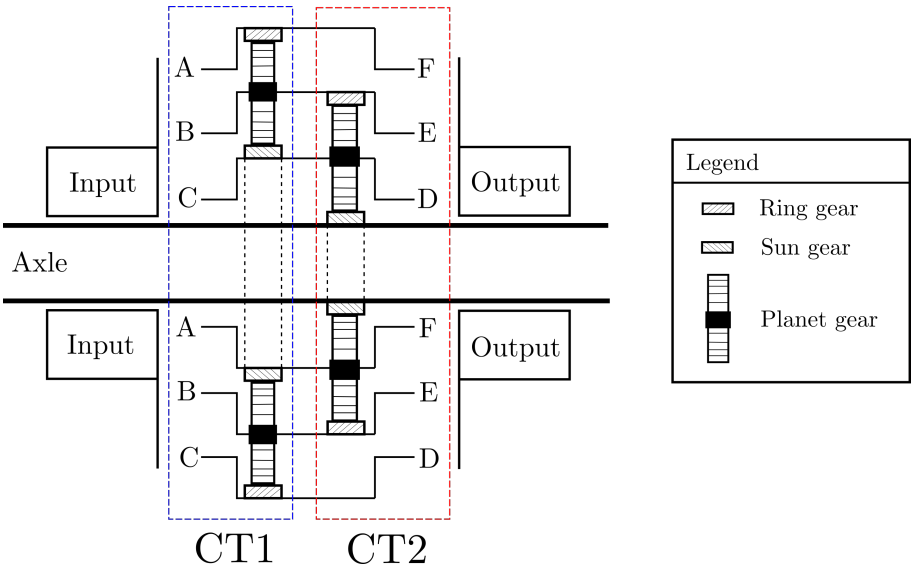


**Figure 2.10:** The first two planetary series in the Kindernay XIV gearhub.

- DOF2: Coupling or constraining any of the three shafts

Hence, we have a total of 4 DOF's before combining the component transmissions. The DOF's are then reduced in the following way:

1. Coupling the B shaft with the E shaft
2. Coupling the C shaft with the D shaft
3. Fixing the sun in CT2

The sun gear in CT2 is part of the hub axle, which is locked in the frame upon tightening the thru-axle in the bicycle frame. This leaves one DOF left to be determined, namely the input speed on any of the shafts A, B or C. Hence, if setting the speed for any of these shafts (A-C), the speed of all the other shafts (A-F) are determined. The next step is then to determine which output shaft (D-F) to couple to the reduction gear.

In summary, the gear ratio of combined transmission CT1-CT2 is determined by the following:

- The desired input shaft (A-C)
- The desired output shaft (D-F)

The result is visualized in Figure 2.11(a), which represents a simplified view of Figure 2.10. The coupled shafts are illustrated as a continuous tooth rack, separated by the planets that connect them. The input section (shaft A-C) is positioned on the left and the output section on the right. Figure 2.11(b) shows the corresponding speed for each shaft, given an input on (A-C). For example, shaft AF is spinning at four times the speed of shaft CD. The exact speed ratio between the shafts is determined by the number of teeth and diameters on the gears, but due to company secrecy this is not discussed further.

From table 2.1, we can see that a total of 7 gear ratios are achieved by combining different input and output shafts – for instance, gear 1 has input on the AF shaft and output on the CD shaft,

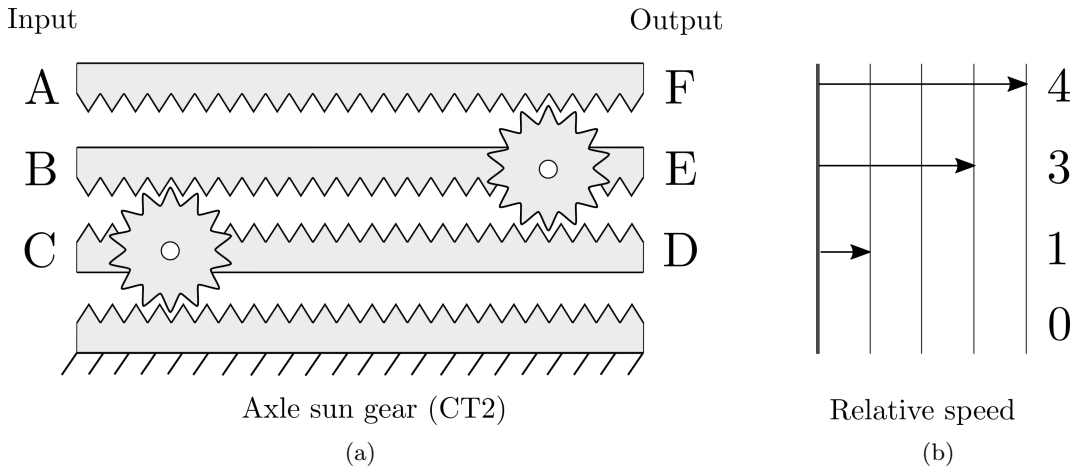


**Figure 2.11:** A simplified view of the first two planetary series in the XIV gearhub (a) and their speeds relative to each other (b).

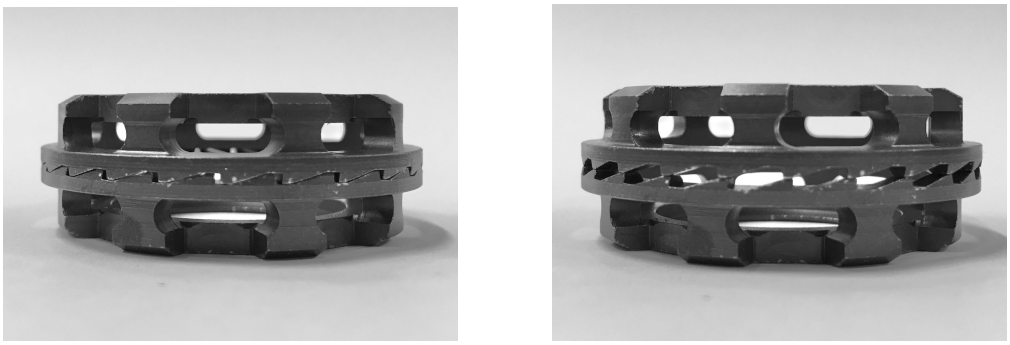

(a) Engaged

(b) Disengaged or freewheeling

**Figure 2.12:** Dog clutches in the Kindernay XIV.

giving a gear ratio of $i_1 = \frac{4}{1}$. Gear 4 uses the same shaft input and output, simply giving a gear ratio of $i_4 = 1$.

The output from CT2 is then input into the sun of the reduction gear. The reduction gear consists of a single planetary gear set, where the planetary carrier is coupled to the gearhub housing, and consequently the wheel as shown in Figure 2.13. Just like the compound transmissions previously discussed, the reduction gear on its own has 2 DOF's. The following constraints are then implemented:

- Gear 1-7 (enabled state): Fixing the ring gear to the axle. The power flows from the sun, to the planets and subsequently the planet carrier.
- Gear 8-14 (disabled state): Fixing the sun gear to the ring gear. The planetary gear is locked, and power flows directly from the sun to the gearhub housing

While the idea of combining planetary gear sets is pretty straightforward, the real complexity lies in shifting the various inputs and outputs in a robust and repeatable manner – and with limited space. In the XIV, this is accomplished by using several ratcheting dog-clutches in various shapes

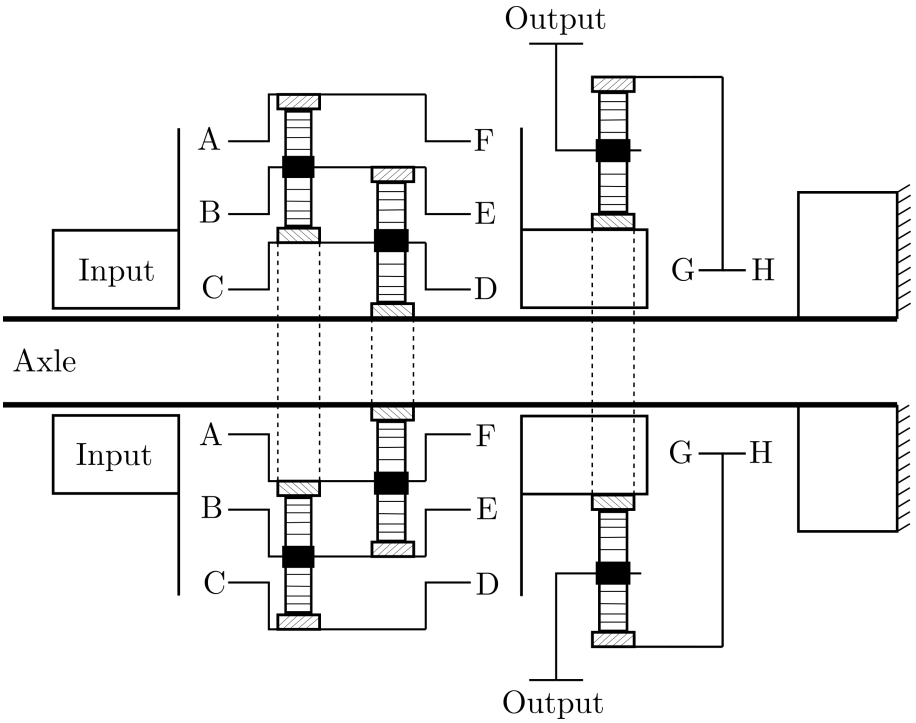


**Figure 2.13:** The first two planetary series, combined with the reduction planetary series in the Kindernay XIV gearhub.

and arrangements, as shown in Figure 2.12. Each shaft from Figure 2.13 has two complementary clutches for input and output, simply designated by the letters A-H for their respective shafts. For example, shaft AF has clutch A for input and clutch F for output. The dog-clutches are spring loaded and can transmit load in one direction of rotation and freewheel (slip) in the opposite direction. The inputs and outputs are adjusted by moving the axial position of the dog-clutches, resulting in engagement or disengagement. Clutches that spin slower than the engaged clutch simply freewheel and do not need to be disengaged. As a result, each of the 14 gears has its unique combination of engaged, disengaged and freewheeling clutches.

Each of the 14 gears will therefore have a slightly different efficiency, resulting from multiple variables:

- Number of active planetary gear sets
- Speed of the active planetary gear sets
- Engagement of reduction gear
- Speed of reduction gear
- Number of freewheeling dog clutches

Hence, there will be supplementary losses related to the reduction gear, yielding worse efficiency for the first seven gear speeds when it is enabled. Due to the internal construction of the XIV, the reduction gear likely has considerably worse efficiency compared to the first two planetary gear sets. This is largely due to a sub-optimal sun gear size and tooth profile that was necessary to fulfill the spacial constraints, while outputting the desired gear ratio.

| Gear | Number of active planetary gear sets | Reduction gear | Engaged clutches | Freewheeling clutches |
|---|---|---|---|---|
| 1 | 3 | Enabled | AD | - |
| 2 | 2 | Enabled | BD | A |
| 3 | 3 | Enabled | AE | D |
| 4 | 1 | Enabled | AF | DE |
| 5 | 3 | Enabled | BF | ADE |
| 6 | 2 | Enabled | CE | ABD |
| 7 | 3 | Enabled | CF | ABDE |
| 8 | 2 | Disabled | AD | G |
| 9 | 1 | Disabled | BD | AG |
| 10 | 2 | Disabled | AE | DG |
| 11 | 0 | Disabled | AF | DEG |
| 12 | 2 | Disabled | BF | ADEG |
| 13 | 1 | Disabled | CE | ABDG |
| 14 | 2 | Disabled | CF | ABDEG |

**Table 2.1:** An overview of the clutch engagement in the different gears of the Kindernay XIV.

Reliable efficiency data for the Kindernay XIV does not exist and the absolute efficiency has too many variables to be approximated analytically. However, one can estimate the relation between the efficiencies of the various gears based on the relative speed and the mechanisms in operation. A comparison of all 14 gears that builds on these parameters is shown in Table 2.1.

As an example, one would expect worse efficiency in CT1-2 for gear 1 compared to gear 4, because gear 1 involves more active planetary gear sets. On the other hand, the reduction gear is spinning faster gear 4, yielding worse efficiency. Gear 7 stands out as the gear with poorest efficiency, due to the combination of 3 active planetary gear sets, an enabled reduction gear with high input speed and two freewheeling clutches. On the other hand, gear 11 will probably be one of the better performing gear combinations, due to no active planetary gear sets and no reduction gear. These relations will be important to revisit when the efficiency testing rig is in operation.

## 2.4 Previous testing rigs and experiments

Several studies on gearhub efficiency testing exist, with a varying degree of scientific consensus. No study has so far included the Kindernay XIV gearhub – mainly due to the fact that it only recently became available to the public market. A review of the most important, existing gearhub efficiency studies is given next.

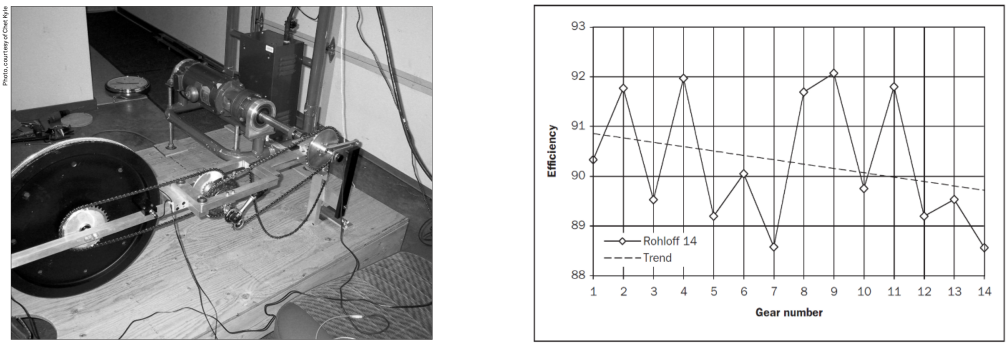


(a) (b)

**Figure 2.14:** The testing rig used by Chester R. Kyle, Ph. D and Frank Berto [7] (a) and the efficiency results for the Rohloff Speedhub gearhub (b).

### 2.4.1 Chester R. Kyle, Ph. D and Frank Berto

This study dates back to 2001 [7], and can be assumed as one of the first scientific gearhub efficiency studies. Many of the gearhubs on the market today build on long-established principles and the data from gearhubs tested in this study is still relevant today. The study is seemingly unbiased and objective, but lacks detail related to uncertainty and data processing.

The testing rig consisted of a frame with a driving motor, dropout for the gearhub and a flywheel with a nylon string – the latter was wrapped around the flywheel twice, acting as a friction brake. The testing rig employed two chain transmissions to connect the motor to the hub, and the hub to the brake, as shown in Figure 2.14(a). Measurements were done with one load cell mounted to the motor housing (preventing rotation) and one load cell connected to the nylon string on the flywheel. Measurements were conducted at 80 W, 150 W and 200 W. The power losses from the other drivetrain components (chains and bearings) were subtracted from the results. The testing protocol is not well documented, and there is no information about measurement accuracy or confidence intervals. Furthermore, some of the results have questionable validity. An example of this is the 3-speed Sachs gearhub which showed worse efficiency in the direct drive (2nd) gear compared to 1st and 3rd gear.

The study tested 11 gearhubs in total, the most interesting one being the Rohloff Speedhub with an efficiency result between 88.5% and 92% as shown in Figure 2.14(b). This was naturally bad PR for Rohloff, who followed up with an independent study to disapprove the results.

### 2.4.2 Rohloff's independent study

The Rohloff study [8] is special in that it is sparingly documented, in fact there is no information on the testing rig setup other than it having a chain transmission. The tests were allegedly performed at power between 300-400 W, thus notably higher than Kyle and Berto's test. The results were also noticeably better, ranging from 96-99% as shown in Figure 2.15(a).

Rohloff's argumentation for performing the tests at higher power levels is based on the variable torque seen through one crank revolution, as shown in Figure 2.15(b). Rohloff justified this because they had seen that the same relation modelled real world chain wear in their chain wear test. The tests where therefore run at a constant power level twice the theoretical input power, hence a 400 W test at constant power was ment to correspond to a rider pedalling 200 W.

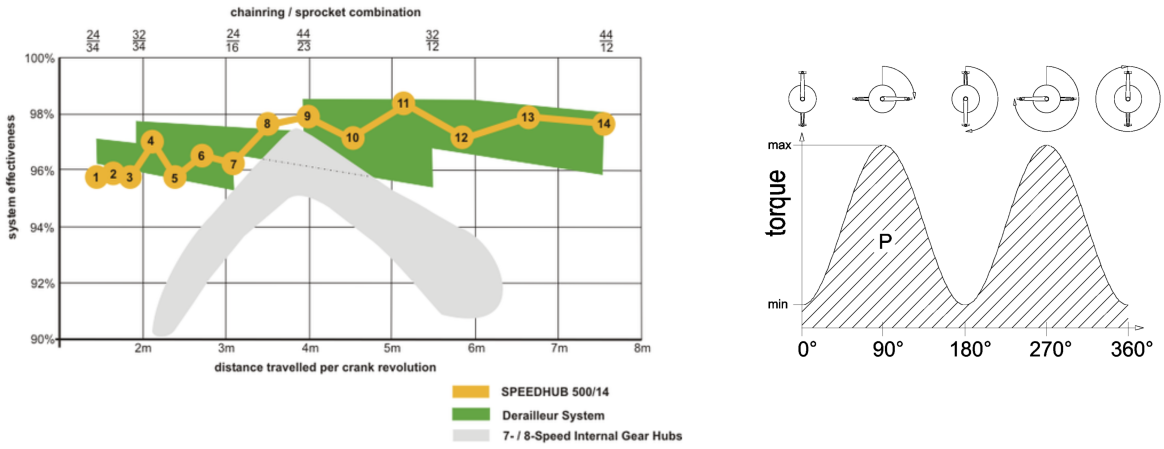


(a) (b)

**Figure 2.15:** The results from Rohloffs independent study[8], allegedly compared with a 9-speed chain-derailleur transmission

### 2.4.3 The American society of mechanical engineering (ASME)

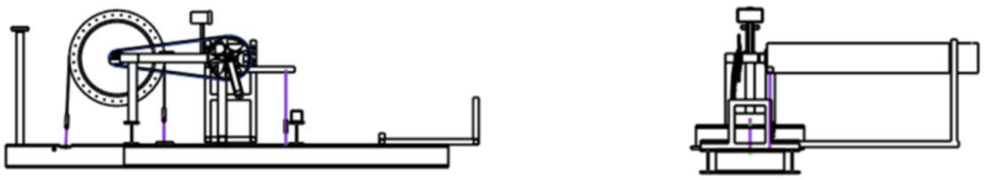

(a) (b)

**Figure 2.16:** The basic illustrations for the ASME-study testing rig [5]

The ASME study [5] was published in 2013, testing the efficiency of four different hub gears, a 9-speed chain-derailleur transmission and single speed chain and belt drive transmissions. It is to this date the most well documented gearhub efficiency study, and is therefore throughly reviewed. The testing rig was based on an ergo-meter bike frame, thus being relatively similar to the one in Chester R. Kyle and Frank Berto's study [7] – albeit with some important differences:

- The brake was directly coupled to the gearhub (no chain transmission)
- The friction brake was only wrapped around half of the flywheels circumference and had one load cell in each end

The motor was free to rotate around its own axis and was supported by a force transducer that measured the input torque. The motor power was then transmitted to the gearhub by a chain transmission, with a length similar to a normal bicycle frame. Notably, the sprocket size used for the gearhubs was not constant, but varied between 16T and 25T. Each gearhub was laced to a custom steel flywheel, with the friction belt surrounding the top half circumference. Other than the

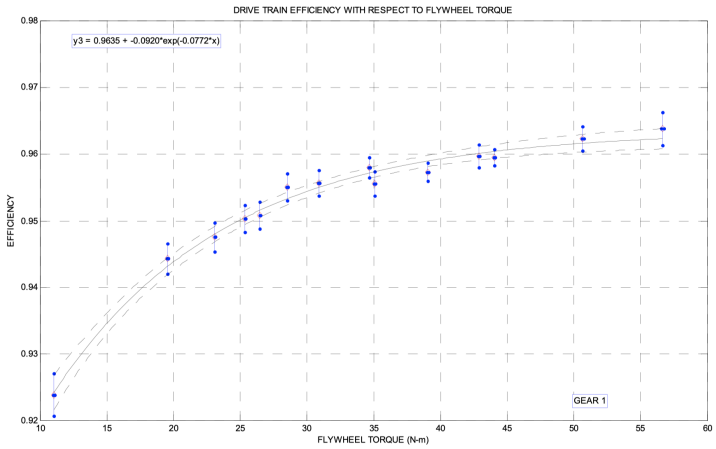


**Figure 2.17:** Exponential curve fitted to the measured efficiency data

illustrations shown in Figure 2.16, no additional details or actual pictures of the testing rig were given.

The test was run at various power levels from 180 W to 450 W, with a total of fourteen different power and speed combinations. The standard deviation was then combined with the calculated measurement uncertainty, giving 95% confidence intervals for each measurement. An exponential function was then fitted to the results, as shown in Figure 2.17. The reported efficiencies essentially represent the value that the exponential function stabilizes to for "infinite" torque. Thus, the results provide a comparison between the tested transmissions, but cannot be directly compared to the aforementioned tests.

The results can be summed up as follows:

- Rohloff Speedhub 500/14: Reported efficiencies from 95.7% to 99.5%, with 11th gear (direct drive) having the best efficiency and 5th having the worst efficiency. Gear 1-7 had notably worse efficiency, due to the use of a reduction gear.
- Shimano Alfine 11: Efficiency ranging from 90.4% to 96.6%, with the best efficiency in seventh gear and the worst efficiency in fourth gear (generally not a clear trend).
- Sturmey Archer X-RK8(W): Efficiency ranging from 84.6% to 99.84% with the best efficiency in first gear and then gradually decreasing.
- SRAM-dual drive 3-speed gearhub: Stable, high efficiency of 98.38% to 99.82%.
- Ultegra RD6500 9-speed chain-derailleur transmission: Only seven gears were tested, ranging from 97.69% to 99.37%. The efficiencies seemed to be dependant on the sprocket size and the chain alignment, giving best efficiency for the middle gears with a straight chainline and reasonably large sprockets.
- Single speed chain: Efficiency of 99.7%, similar to the best efficiency of the Ultegra transmission.
- Gates belt drive transmission: Efficiency of 98.3% to 98.0%, where more belt tension yielded slightly worse efficiency. Belt tensions were not measured.

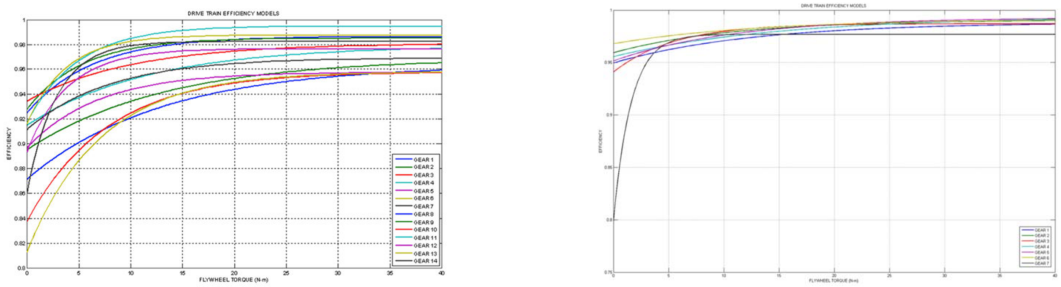

(a) (b)

**Figure 2.18:** A comparison between the efficiency results for the Rohloff Speedhub and Ultegra chain derailleur transmission [5]

The study does not mention whether the chain loss was subtracted from the gearhub data, although the results indicate this due to some efficiencies being higher than the single speed chain transmission. The validity of comparing the "infinite torque" results between systems is a highly debatable – for example, the chain-derailleur transmission efficiency curves flat out much sooner than the gearhub curves, as shown in Figure 2.18. This indicates that the disparity between gearhub/derailleur efficiency is much larger for lower, and perhaps more realistic torque values. The steep, initial slopes of the Rohloff curves could therefore also explain the contrasting results in Kyle/Berto's and Rohloff's own study.

### 2.4.4 Comment from the author

A manufacturer can very easily configure a test to obtain desirable numbers, that not necessarily depict the reality. Many of the losses in a gearhub are independent of the input power and one can therefore run tests at higher power to obtain better efficiency results. It is believed that the high dispersion between Kyle and Berto's non-biased study and Rohloffs independent study is largely due to Rohloff running the tests at much higher power levels. In addition, the validity of running the tests at double power values is questionable and not proven by any means. The results from the ASME study [5] support this theory. Moreover, any of these tests would be hard to reproduce due to the limited information about the testing rig hardware and testing procedures. The ASME study is by far the best documented study, with calculated uncertainties and statistical confidence intervals for each measurement. Still, the validity of comparing "infinite torque" efficiencies is not straightforward.

## 2.5 Overview of the current testing rig

This section intends to give an overview of the testing rig and its technical components at the time of project startup in January 2019.

Myklestad [9] conceptualized and built the first iteration of the efficiency testing rig during the spring of 2018, with supervision from company engineer Knut Tore Ljøsne and supervisor Geir Terjesen from Norwegian University of Life Sciences (NMBU). The overall goal of Myklestads thesis was to calculate, construct and build the mechanical foundation of an efficiency testing rig. The goal was not to complete the testing rig however, as the whole project was considered too extensive for one semester. The task of implementing and programming the control system for the testing

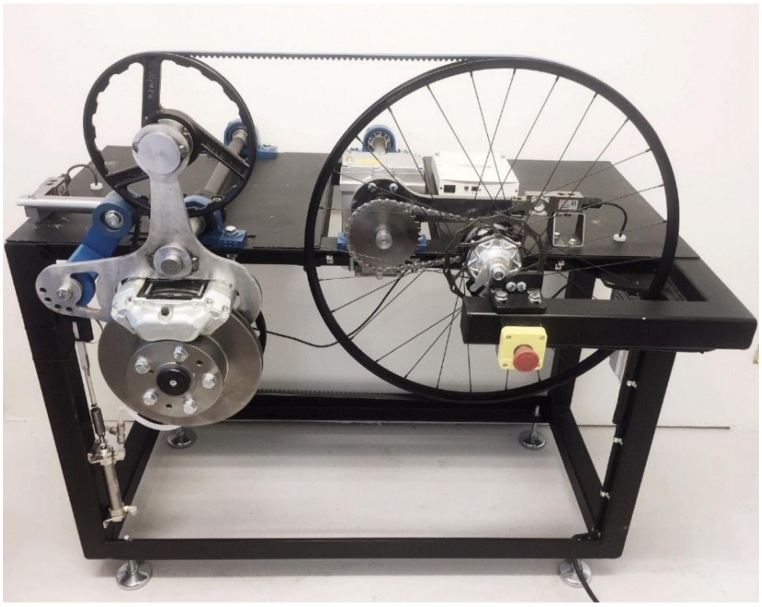

**Figure 2.19:** Overview of the testing as built by Myklestad [9]. The force transducers were later removed.

rig was therefore left to the company. This task was never completed and the testing was never brought to a working state, due to several issues detailed in the following.

### 2.5.1 Overall geometry and design

The testing rig was built around a rigid steel frame with approximate dimensions 1300 x 800 x 900mm. The frame is supported by four adjustable machine feet to account for uneven flooring. The frame was designed to accommodate the motor assembly and wheel in one end, and the brake system in the other end, as shown in Figure 2.19.

The motor and brake systems were designed to pivot around two separate axles, each with a separate arm extending from the center of the axle. Each arm was connected to its own force transducer. This way one could compare the in-going motor load with the outgoing brake load and thereby compute the efficiency of the gearhub. Constant losses related to the chain and V-belt transmissions, bearings etc. would be accounted for by calibrating the rig against a single speed rear wheel (1:1) with no internal mechanisms.

The rig was built with an extended profile with a 90° angle that creates a U-formed dropout where the wheel could be installed, shown in Figure 2.20(a). Each side of the dropout had its own bracket that held a standard bicycle dropout, and by swapping the dropouts in the bracket one could adapt the testing rig to fit different hub and axle standards.

The sub-components of the testing rig are described next.

### 2.5.2 Motor

The testing rig was built with a NORD SK80 3-phase motor connected to a NORD SK500e frequency inverter, run on standard 230V mains supply. The motor was connected to a 26:1 gearbox, and the whole unit was hung on the axle from the gearbox output. The motor was therefore free to rotate

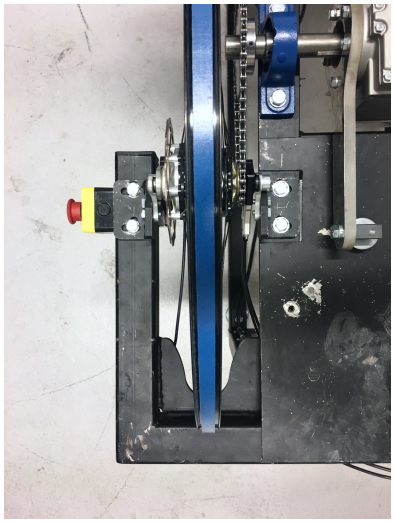

(a) The dropout geometry on the testing rig.

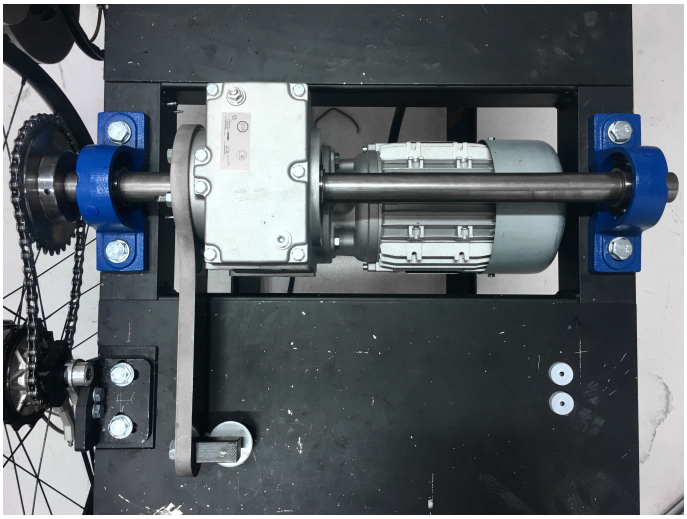

(b) The gearbox axle

**Figure 2.20:** Components on the testing rig.

around the axle from the gearbox, as shown in Figure 2.20(b).

### 2.5.3 Transmission system

The rig was built with two different power transmissions systems, namely

- A chain connecting the motor axle to the input cog on the gearhub
- A V-belt routed from the bicycle rim (gearhub output) to the brake

A belt tensioner was installed on the brake side to accommodate different rim sizes and keep the desired preload on the belt.

### 2.5.4 Braking system

The brake system unit was composed of two pulleys with an equal offset from the brake pivot axle. The bottom pulley was connected to a brake disc which sitting inside a brake caliper, as shown in Figure 2.19. The brake caliper was in turn actuated by a master cylinder that was operated by a linear actuator, connected to a control board. The control board was operated by a simple potensiometer, but had the capability of connecting to a PC via USB.

### 2.5.5 Sensors and control system

Per January of 2019 there was no control system installed on the testing rig. Consequently, the rig was simply run at a set frequency in the inverter. The testing rig was also missing its force transducers. The company originally used a National Instruments DAQPad 6015 for control and data-logging and Flintec SB6 beam force transducers on in-going and out-going measurements. All of these devices were lent from his university and therefore had to be returned after finishing the project.

# Chapter 3

# Requirements study

The company established a requirements specification for the testing rig during the previous project phase. This requirements specification is shown in Table 3.1, translated from Norwegian by the author.

Many of the requirements related to dimensions and practicality were already "set" as the basic structure was already built. The strategy was to develop a new requirements specification based on the old one, but with more emphasis on compatibility and ease of use during operation.

As explained in Section 2.4, a manufacturer can very easily manipulate such an efficiency test to obtain desirable numbers, that not necessarily depict the reality. It is therefore important to have the ability of running multiple hubs on the same testing rig, to get a true comparison.

A key task would therefore be to examine the properties of relevant gearhubs. Myklestad did not go in-depth in this subject and a more comprehensive study is therefore done in the following.

| **Requirement** | **Value/explanation** |
|---|---|
| Total measurement sensitivity | $\pm 0.5$ |
| Compatibility | All gearhubs used on traditional bicycles with 10- and 12 mm axles. |
| Power | Adjustable with $P_{\max} = 400$ W |
| Torque | $T_{\max} = 130$ Nm |
| Motor output speed | $\omega_{\text{motoroutput}} = 30 - 120$ rpm |
| Construction | The machine should be designed as a stationary device, requiring little setup time |
| Lifting handles | The machine should be easily movable, either by lifting handles or pallet jack |
| Space efficiency | The machine should be space efficient, although no specific requirements were set |
| Budget | Material cost including control system should not exceed 50 000 NOK |

**Table 3.1:** The requirements for Myklestads testing rig [9]

## 3.1 Study of relevant gearhub systems

The current testing rig had been designed primarily around the Kindernay XIV hub system and compatibility with other gearhubs was somewhat undetermined. It would therefore be important to ascertain the current state of compatibility. Furthermore, in the event that the testing rig needed more substantial modifications, it would be equally important to be aware of the constraints imposed by different gearhubs.

The efficiency tests outlined in Section 2.4 were conducted several years ago and the gearhub market has seen several new products since their publication, many of which are relevant for efficiency testing. A list of relevant gearhubs was decided on in cooperation with the company and these gearhubs were studied with attention to the following five parameters: axle standard, in-going sprocket interface, brake disc compatibility, torque arm geometry and shifting mechanism.

These parameters are highly relevant in designing a universal testing rig, as will be explained next.

#### Axle standard

The hub axle is the interface that connects the hub, and thereby the wheel, to the bicycle frame. Rear axle standards are wider than front axle standards because they also have to accommodate drivetrain components. The number of axle standards have evolved considerably in later years, usually with a guiding goal of increasing stiffness (in frame/hub and wheel) and/or tire clearance. An overview of rear axle standards is given below.

- 5×130 mm (open dropout): Quick release axle that only provides axial clamping force on the frame and hub. The hub axle has a 10mm outer diameter that provides radial support in the frame dropouts, and a 5 mm internal diameter for the quick release axle. Commonly used for road bikes with rim brakes.
- 5×135 mm (open dropout): Commonly used for older mountain bikes, similar to 5×130 mm except being 5 mm wider.
- 10×135 mm (open dropout): Solid hub axle (not hollow) with a 10 mm outer diameter and is threaded in both ends. Axle nuts (one on each side) provide axial clamping while the hub axle provides radial support. Used on most gearhubs.
- 10×135 mm thru-bolt (open dropout): Rare and not found on many modern hubs or bicycles. The hub axle has a 10 mm inner diameter, complemented by a removable 10 mm axle provides axial clamping as well as radial support.
- 12×142 mm (closed dropout): Popularly called "thru-axle" and widely adopted. The axle must be completely removed to remove the wheel because the dropouts are "closed", i.e. without slots.
- 12×148 mm (closed dropout): The successor to 12×142 mm, designed to provide wider hub flanges (stiffer wheel) and increased tire clearance.
- 12×150 mm (closed dropout): Older thru-axle standard for downhill bicycles.
- 12×157 mm (closed dropout): Proposed successor to 12×148 mm, designed to provide even wider hub flanges (stiffer wheel) and increased tire clearance. Used on modern DH-bikes, otherwise not widely adopted.

Axle standards for gearhubs are normally either 5×135 mm quick release or 10×135 mm solid axles.


(a) Standard sprocket interface

(b) Proprietary sprocket interface for Shimano Nexus gearhub

**Figure 3.1:** Various sprocket interfaces.

(a) Kindernay XIV with 7-bolt brake rotor

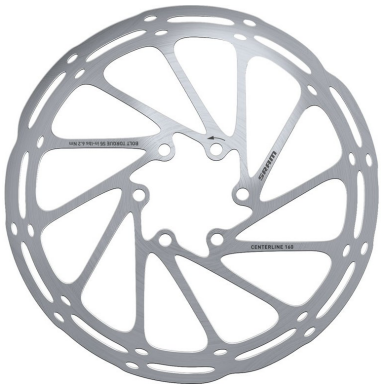

(b) Standard IS 6-bolt brake rotor

**Figure 3.2:** Various rotor interfaces

### In-going sprocket interface

All gearhubs has some variant of a single speed sprocket on the drive side that takes input from the bicycle chain. Some hubs are also compatible with special sprockets designed for belt drive systems. Sprockets come in various sizes, with different tooth counts to adjust the gear ratio. The outer tooth profile is standardized, but the splined interface that connects to the hub differs between different gearhub systems, as shown in Figure 3.1.

The sprocket spline interface is relevant if considering a direct drive motor coupling, e.g. a motor that attaches directly to the gearhub.

### Brake rotor mounting interface

Most new gearhubs are compatible with disc brakes, but as Figure 3.2 shows there are variations in brake disc bolt patterns.

The two most common brake rotor mounting interfaces today are:

- 6-bolt IS: The international standard, most common.
- Centerlock®: A splined connection with a lockring, developed by Shimano but also used by

(a) The shifting axle on the drive side

(b) The Kindernay XIV SWAP hub shell.

**Figure 3.3:** Components of the Kindernay XIV.

other hub manufacturers. Can be converted to IS 6-bolt with adapter.

In addition, gearhubs like the Kindernay XIV and Rohloff Speedhub have their own proprietary rotor interfaces. The brake disc interface is relevant if considering a direct drive brake system.

#### Torque arm geometry

In gearhub systems, torque on the wheel does not always equal torque to the road because of of the different gearing ratios – the leftover torque must therefore be taken up by the bicycle frame. This is usually accomplished with a torque arm that connects the gearhub to the frame, one example shown in Figure 3.2(a). The torque arm is usually placed on the non-drive side of the hub, but several variations exist and this should be taken into consideration.

#### Shifting mechanism

The external mechanism with the greatest diversity in gearhub systems is perhaps the shifting mechanism. Depending on the gearhub, it can be positioned on the drive- or non-drive side and have different actuation mechanisms. The most common mechanisms are:

- Cable-actuated with double gear cables (one cable for shifting up, one for shifting down)
- Cable-actuated with a single cable and a spring return inside the gearhub (the cable is pulled to shift up and released to shift down)

The Kindernay gearhubs have a less common hydraulic shifting actuator.

Having the ability to shift gears during efficiency testing is highly desirable, especially if considering fully automating the testing process down the road.

### 3.1.1 Relevant gearhubs

A quick overview of the relevant gearhubs is given in the following.

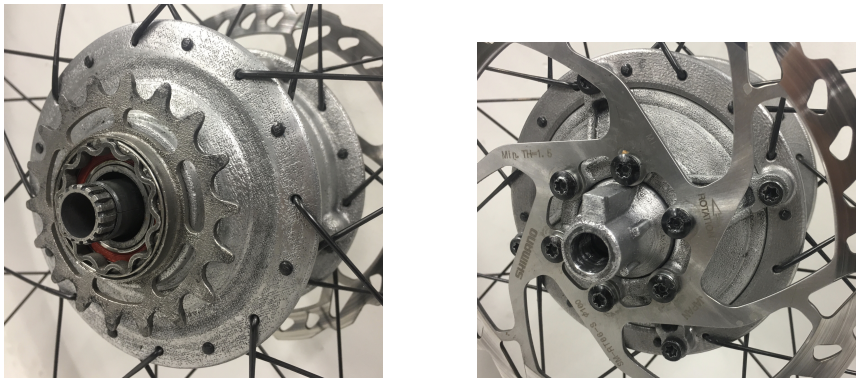

(a) Drive side (b) Non-drive side

**Figure 3.4:** The Kindernay VII gearhub (prototype).

### Kindernay XIV

The Kindernay XIV is a two-piece system, consisting of the gearhub and a shell with hub flanges and spoke holes. This allows the gearhub to be separated from the rim and spokes without rebuilding the wheel, as shown in Figure 3.3. The bolts connecting the hub and shell are also used to fixate the braking rotor. Because of this, it has a proprietary 7-bolt brake disc that is not seen on any other hub system. A note on the expected efficiency of the XIV gearhub is given in Section 2.3

Another important feature is the hollow 12 mm axle, supporting standard 12×142 mm and 12×148 mm thru-axle systems as well as 10×135 mm thru-bolt systems by the use of different adapters.

The shifting on the XIV is hydraulically actuated from the drive side of the hub. The shifter actuator slides on the gearhub when inserting the wheel into the frame, and locks into place when the thru axle is tightened. Furthermore, it is a structural part of the gearhub and therefore necessary to include when mounting the gearhub in a testing rig. The actuator has two toothed racks that move up and down to rotate the shifting axle, shown in Figure 3.3(a). The torque arm is on the non-drive side as shown in Figure 3.2(a). Lastly, the gear hub has a standard sprocket interface as depicted in Figure 3.1(a).

### Kindernay VII

The Kindernay VII is essentially a simplified version of the Kindernay XIV. It is a one-piece system (no removable hub flange) where the rim is built directly onto the hub. The braking rotor interface is a standard 6-bolt IS. The VII does not have a reduction gear set and therefore only seven speeds, although the rest of the internal mechanism is similar. Thus, it is reasonable expect better overall efficiency compared to the XIV, especially in the first 7 gears when the XIV's reduction gear is enabled.

The VII supports the same axle standards as the XIV, but has a slightly different torque arm that is integrated into the non-drive side end cap, as shown in Figure 3.4(b). The shifting mechanism is identical to the XIV and is a structural part of the gearhub. The sprocket is a proprietary design however, with a custom spline pattern and a circular snap ring to lock it in place, shown in Figure 3.4(a).

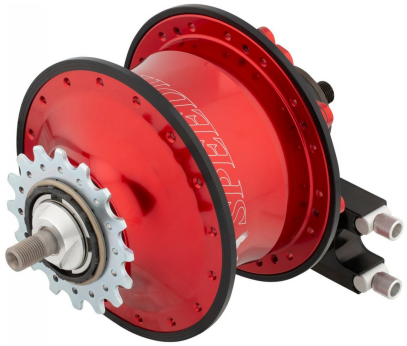

(a) Rohloff Speedhub 14

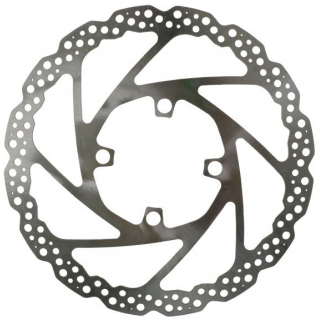

(b) Proprietary 4-bolt rotor interface

**Figure 3.5:** The Rohloff Speedhub and its brake rotor.

### Rohloff Speedhub

The Rohloff Speedhub is was launched back in 1996 [10], but has seen several updates since – including a disc-brake and a fatbike version. The internal mechanism, however, has largely stayed the same. The Speedhub has three planetary gear sets in series, but unlike the XIV it also relies on compound planets. The two first gear sets combined achieve seven speeds and the last set acts as a reduction gear, doubling the number of speeds to 14. Shifting is achieved by locking the sun gears with pawls and/or locking any of the two first planetary gear sets to direct drive with an axial clutch. Because the pawls for the sun gears are positioned close to the axle, the space in the center of the hub is limited and the Speedhub is therefore only available with a 5 mm quick release or a 10×135 mm solid axle. The hub itself is a one-pice system. It can be converted to modern axle standards with proprietary adapters, depending on the exact axle system on the frame [11].

The disc-brake version has a proprietary 4-bolt brake disc as shown in Figure 3.5. The shifting is actuated by double gear cables, with the actuator being positioned on the non-drive side of the hub, together with the torque arm. The sprocket is a custom design.

### Enviolo/Nuvinci

The Envilo gearhub [12] (previously called Nuvinci) stands out from other gearhubs in that it does not have sequential gearing, but operates like a continuous variable transmission (CVT). It is based on a set of rotating, tilting steel balls fitted between two rings (input and output) as shown in Figure 3.6(b). The speed ratio between input and output is controlled by adjusting the angle of the ball axles. Torque is transmitted by the use of a so-called "traction fluid" between the moving components. The Enviolo hub is famously known for its low efficiency (allegedly between 80-90%, a direct cause of the losses related to the friction transfer).

The hub, shown in Figure 3.6(a) is a one-piece system with a solid 10×135 mm axle and support for IS 6-bolt brake rotors. It relies on no-turn (keyed) washers to prevent the axle from turning in the dropouts [13]. The shifting actuator is cable operated and works by rotating a splined axle on the drive-side. It has a standard sprocket interface.

### Shimano Nexus & Alfine

Shimano has been manufacturing gearhubs since 1957 [14] and has several gearhubs in the market. There are two main product series, Nexus (low-end, 3, 4, 5, 7 and 8 speeds) and Alfine (high-end, 8

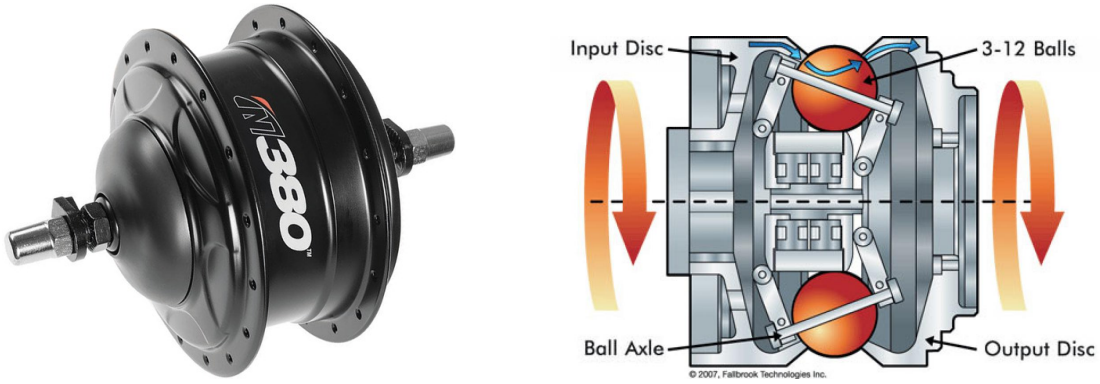


(a) Gearhub (b) Internal mechanism

**Figure 3.6:** The Enviolo gearhub with its CVT internals.


(a) Shimano Nexus (b) A newer Sturmey Archer 5-speed hub.

**Figure 3.7:** Various gearhubs.

and 11 speeds). The newer Nexus hub is shown in Figure 3.7(a). The hubs differ in geometry/weight and number of speeds but the internal mechanisms are similar.

All Shimano hubs rely on a series of planet gears to achieve different speeds. The hubs are shifted by locking one or more sun gears with moving pawls situated on the main axle, similar to the Rohloff Speedhub. The space around the axle is thus limited and all Shimano hubs therefore have a solid 10×135 mm hub axle.

The Shimano hubs all use a cable operated shifting actuator located on the drive side, with the exception of the Alfine Di2 (electronically shifted) hub. The actuators shift by rotating a splined axle on the drive-side. The shifting axle has a spring return and the actuator is therefore operated with only one cable.

The sprocket interface, shown in Figure 3.1(b), is custom but identical on all Shimano hubs. The torque arm is generally placed on the non drive side. Lastly, newer versions of both the Nexus and Alfine hub series have disc brake compatibility with Centerlock® rotor interfaces.


**Figure 3.8:** A disc brake compatible version of the SRAM G8 gearhub.

### Sturmey Archer

Sturmey Archer is a veteran in the gearhub market, having manufactured hubs since 1902 [15]. They have a multitude of versions, the most common being 3, 5 and 8 speed gearhubs. However, they all rely on similar principles for the internal mechanisms – all SA gearhubs use series of planetary gear sets of varying complexity.

Older versions of the hubs were often shifted with a toggle chain on the drive side (moving inside the hub axle), connected to a single shifting cable that was paired with the handlebar shifter. Never models, like the one shown in Figure 3.7(b) are shifted with a rotary gear selector that rotates a shifting axle on the gearhub. The shifting mechanisms all have a spring return.

Newer versions of the Sturmey Archer hubs are available with IS 6-bolt brake disc interfaces and all feature a solid 10×135 mm axle. Lastly, the sprocket interface is a proprietary design and the torque arm is located on the non-drive side.

### SRAM G8

The SRAM G8 was launched in 2013 but was discontinued in 2015 after being a complete failure in the gearhub market. SRAM sold off its gearhub division to ZF not long after, and the G8 is their latest (and last) gearhub. The G8, shown in Figure 3.8, was very heavy at 2.1 kg, expensive to manufacture and therefore a pricier option than many of the above hubs.

The G8 is (similarly to many of the previously mentioned gearhubs) composed of planetary gears sets in series and shifted by locking the one or more sun gears with pawls. The hub axle is therefore a solid 10×135 mm variant. The hub is shifted by a single cable actuator on the drive side that rotates the shifting axle, and the return is spring loaded. The G8 is available in a disc brake version, with an IS 6-bolt interface. The in-going sprocket interface is a custom interface and the torque arm is located on the non-drive side.

### 3.1.2 Summary

The relevant specifications for the chosen gearhubs are summarized in Table A.1 in Appendix A. The gearhub study outlined multiple challenges related to compatibility, leading to the following requirements:

- **Axle standards:** The testing rig should have replaceable dropouts to support 12×142 mm thru axle hubs and 5/10×135 mm hubs
- **Shifting mechanisms:** The testing rig should have clearance to accommodate the original shifting mechanisms on both sides of the hub
- **Torque arm support:** The testing rig should have clearance to accommodate torque arms in various shapes on the non-drive side.
- **Driving sprocket:** Any change to the in-going power transmission (for example a direct drive) would require supporting multiple sprocket spline designs.

## 3.2 Other relevant requirements

In addition to requirements stemming from the aforementioned gearhubs, it was necessary to define additional requirements related to compatibility and usability.

- **Quick wheel removal and insertion:** Because multiple hubs were to be tested, removing and inserting the wheel had to be a straightforward process. The need for calibration afterwards should be minimized.
- **Rim size and profile compatibility:** The current testing rig was only run with one wheel size and rim profile. Because most other gearhubs are one-piece systems (rim built onto hub), the rig would have to support various wheel sizes and rim profiles without too much modification.
- **Shifting gears during run-time:** It would be highly beneficial to be able to shift the gearhub during testing to streamline the testing process.

The following features would also be desirable, although not necessary:

- **Testing hubs without rims:** Testing hubs without having to build a wheel would greatly increase the usability of the rig
- **Wheel true dependency:** The current setup with a V-belt transmission would be highly sensitive for radial and lateral wobble in the wheel. Reducing or eliminating this weakness would also improve the usability.
- **Kindernay XIV and VII compatibility:** These hubs would be tested on a regular basis and the rig should therefore be optimized to test these hubs in an time-effective manner.

## 3.3 Requirements specification

The foregoing requirements are summarized into the total requirements specification, shown in Table 3.2. It is worth noting that the current testing rig already supported several of these requirements to some degree, but it was still important to highlight all requirements in case one or more subsystems needed improvement or replacement. The power and torque requirements that Myklestad [9] set,

were evaluated to be adequate and therefore included in the new requirements specification. It is important to emphasize that the original testing rig, while meeting many of these requirements, never produced valid efficiency data due to high instability during operation.

| No. | Requirement | Satisfied |
|---|---|---|
| 1 | Total measurement sensitivity of ±0.5% | No |
| 2 | Compatibility with 10×135 mm and 12×142 mm axles | No[1] |
| 3 | Adjustable power with $P_{max} = 400$ W | Yes |
| 4 | Max torque of $T_{max} = 130$ Nm | Yes |
| 5 | Motor output speed $\omega_{motoroutput} = 30 - 120$ rpm | Yes |
| 6 | Stationary construction requiring little setup time | Yes |
| 7 | Easily movable by pallet jack | Yes |
| 8 | Space efficient | Yes |
| 9 | Quick wheel removal/insertion | Yes |
| 10 | Rim size/profile compatibility | No |
| 11 | Clearance for shifting mechanisms | Yes[2] |
| 12 | Shifting gears during run-time | Yes[3] |
| 13 | Test hubs without rim | No |
| 14 | Wheel true dependency | No |
| 15 | Kindernay XIV/VII compatibility | Yes |

[1] Possible if replacing the sliding dropouts
[2] Not tested but seems probable
[3] Depending on the clearance for shifting mechanisms

**Table 3.2:** Complete requirements specification.

# Chapter 4

# Function test of current testing rig

A function test was performed to assess the functional state of the testing rig and its subsystems. The goal was to identify systems in need of improvement and based on this, compile task list for the next process step.

## 4.1 Known improvement potentials

Myklestad's [9] initial function test of the rig indicated several problems, some of which he corrected during his project period. These were related to

- **Brake rotor lateral trueness:** A 0.5 mm wobble was observed when measuring the laterall trueness of the brake rotor, caused by uneven gluing of the brake rotor bracket. This was corrected by regluing the parts, allegedly bringing the wobble down to less than 0.1 mm.
- **V-belt fitment:** The V-belt had a tendency to flip/turn over on the bicycle rim. This was partially remedied by evenly sanding down the belt on a belt sander, removing the toothed profile entirely. The new profile did not turn over but was still a less than ideal fit on the bicycle rim.
- **Ingoing sprocket radial trueness:** A small radial wobble was measured on the in-going sprocket mounted on the gearbox shaft. This was assumed to be caused by an uneven glue joint between the shaft and the sprocket but was not investigated further, nor corrected.

Several issues were also left unattended because of limited time. A list of known improvement potentials was therefore included, and is repeated in Table 4.1.

Other issues were also pointed out by the engineers at the company who had worked on the testing rig after Myklestad finished his project. These issues were mainly related to

- The motor running uneven, especially at low speeds
- The brake system (caliper and brake disc) provided uneven braking
- The V-belt transmission, while improved somewhat by the new profile, was still not running straight on the bicycle rim

| **Topic** | **Task** | **Comment from the author** |
|---|---|---|
| Control system | Design and implement a control system for the testing rig | As mentioned in section 2.5 this was not part of Myklestads project scope. |
| FEM analysis of bracket for ingoing load cell | The bracket is made from a square steel profile and is prone to twisting. The scale of the problem can be determined using a dial indicator during operation. | The load cell bracket will most likely be replaced. |
| Fatigue- and strength analysis of the motor axle | The motor axle is loaded in several directions and will experience dynamic loads during operation. The situation should be examined further as the deformation could affect the readings from the in-going load cell. | Highly relevant task that should be carried out if the motor and axle is reused. |
| Eigenfrequency analysis of the frame | The eigenfrequencies of the testing rig should be compared to the frequency of the operating components. This could generate unwanted vibrations and subsequent measurement error. | Highly relevant task that should be carried out if the frame is reused. |
| HSE (HMS) | The drivetrain and moving components are not protected during operation. Consequently, there are several pinch point hazards. | Important but not relevant before the testing rig is in working order (one or more components may be replaced). |
| Radius tool | Manufacture measuring tool for wheel radius. | This tool is specific for the V-belt transmission, as the radius of the wheel can vary (depending on which gear-hub/rim is tested). |

**Table 4.1:** A summary of the remaining work Myklestad [9] identified.

## 4.2 Assessment of the current testing rig

During project startup it was decided to do a new assessment of the system, mainly to get first hand experience with the above issues but also to identify any issues not recognised above. As the above systems were highly dependent on each other it was considered important to try and test the sub-systems as independently as possible. The initial impression of the testing rig was that it was very much a work in progress, with several missing components and "loose ends". Several components had to be replaced or repaired in order to test the basic functionality, among other things:

- The V-belt was broken and not usable
- The force sensors were missing, as a result the torque arms were rotating freely
- The brake system needed bleeding
- There were many loose cables to various sensors, boards and actuators

A more detailed assessment of the aforementioned subsystems is given next.

### 4.2.1 Testing rig frame

The testing rig appeared to be well built and offered good adjustability of the position of the motor axle, brake system axle and gearhub. The structure appeared to be straight and well put-together. Moreover, the fact that is was constructed using welded S355 structural steel would make any modifications relatively straightforward.

The machine feet were convenient in positioning the rig in a stable manner. Lastly, the overall dimensions would offer good adaptability if it was decided to modify any of the following sub-systems.

### 4.2.2 Motor & inverter

The initial attempt of running the testing rig turned out to be problematic, as the inverter constantly tripped the earth leakage circuit breaker (ELCB) in the power cabinet. Upon measuring the voltage in the socket, it was found that the circuit in the building had a ground fault. The issue was reported to the power company and temporarily "solved" by disconnecting the ground wire on the inverter. The inverter was now able to run the motor at various speeds, controlled by a potentiometer connected to the analog terminals on the inverter.

To exclude the possible effect of uneven braking and poor fit of the V-belt, a standard 173 mm brake rotor was attached along with an hydraulic brake caliper mounted on the wheel bracket. This brake would be able to deliver decent braking torque directly on the hub, albeit not for very long without overheating. Still, it was regarded as a decent solution for testing the motor system in a more isolated manner, without the influence of the V-belt or existing brake system. A new disc rotor and new brake pads were used, gradually bedded in by manufacturer recommendations. The setup is shown in Figure 4.1(a).

Testing with the temporary brake system revealed that the motor ran with very poor stability, especially at low speeds. The fluctuations had a very low frequency of around 1-2 Hz.. As the force sensors were missing there was no way to quantify the instability directly – it was however easily visualized by placing a rubber dome under the in-going torque arm as shown in Figure 4.1(b), acting

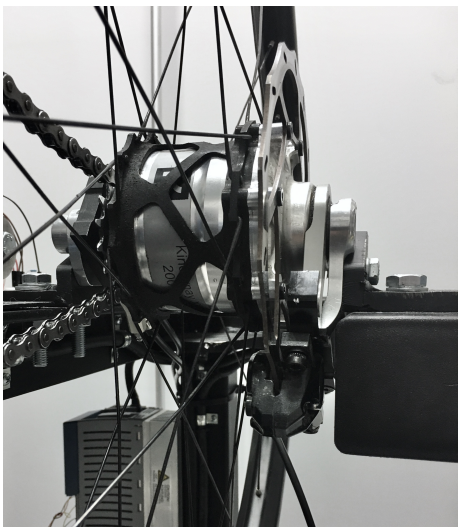

(a) Testing rig with direct mounted disc brake on 173 mm disc.

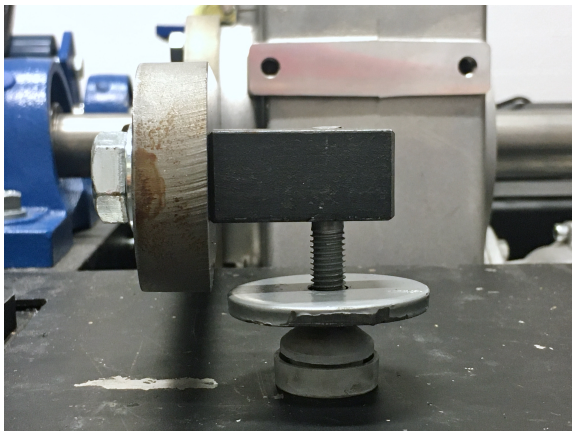

(b) Rubber dome

**Figure 4.1:** The instability of the testing rig was measured with a brake directly coupled to the gearhub and rubber dome, acting as a spring.

as a spring. This allowed the torque arm to move, depending on the braking torque. The following pattern was observed:

- The instability was worse at low speeds and low to medium braking force
- The instability was less prominent at higher speeds and higher braking forces

While the above results weren't very scientific, they still showcased that the motor ran in an inaccurate manner without the influence of the other subsystems.

### 4.2.3 Power transmission

As previously mentioned, the original V-belt was missing from the testing rig. A new V-belt was therefore installed, first with its original profile and afterwards with a modified shape.

Initial testing immediately showed the problem of the V-belt turning over, as shown in Figure 4.2. Further investigation revealed that the pulley wheels on the brake side were severely misaligned, leading to uneven feeding to the bicycle rim and probably contributing to the issue.

The rig was also, tested with a modified V-belt similarly to the one used previously. This improved the stability slightly, but the belt still had a tendency to draft to one side on the rim.

### 4.2.4 Brake system

The brake system was tested with the improved V-belt described in the previous section.

To begin with, the brake disc wobble was measured. The measurement was done at three different diameters on four points around the brake disc, using a dial indicator with a magnetic base holder as shown in Figure 4.3(a).

The measurements indicated a total run-out at around 0.15 mm, somewhat higher than what

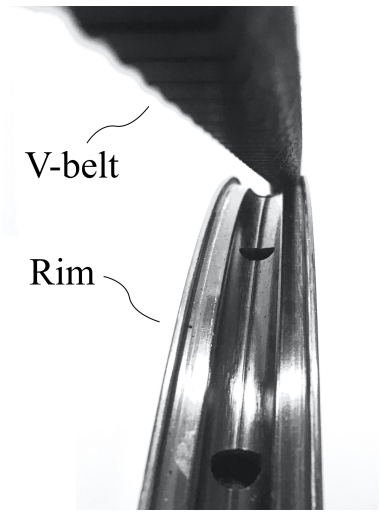


**Figure 4.2:** The V-belt had a tendency to turn of and/or pull to one side of the rim.

Myklestad [9] specified in his findings. As Figure 4.3(b) shows, the run-out was increasing linearly with the radial position.

It was therefore highly probable that the source of the wobble (still) was uneven alignment in the glued fitting between the brake rotor bracket and axle.

The brake caliper used on the rig's braking system had four pistons in total, two on each side. Testing revealed that the pistons on the outermost side were partially stuck and not contacting the pad, even when the master cylinder was fully engaged.

The brake rotor wobble naturally induced some fluctuations in the braking system. This was further complicated by the uneven brake pad pressure from the caliper, thus the brake system needed several improvements.

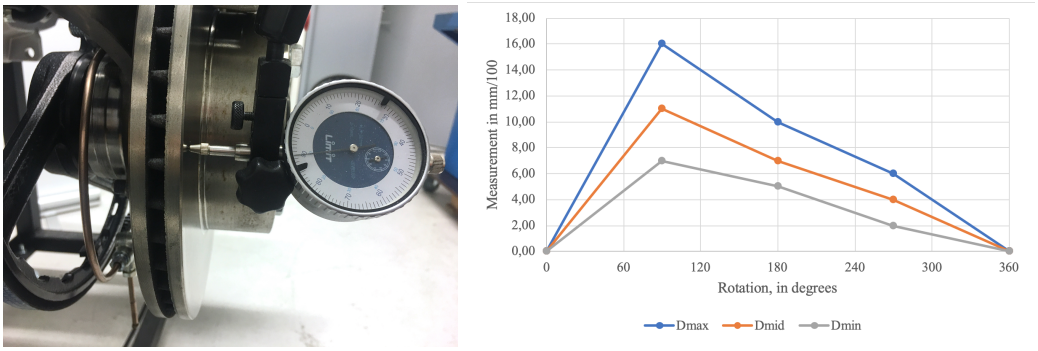


(a) Dial indicator

(b) Measurement values

**Figure 4.3:** The lateral wobble of the brake disc was measured with a dial indicator and indicated a maximum run-out of around 0.15 mm.

### 4.2.5 Force sensors and data logging

The force sensors on the testing rig where originally mounted as shown in Figure 4.4.

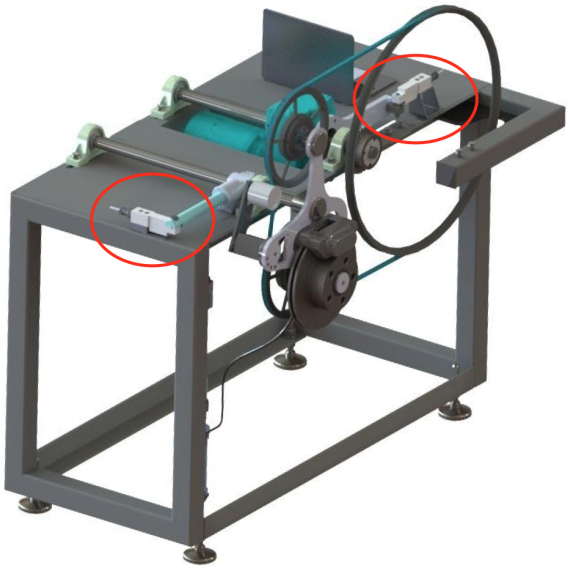

**Figure 4.4:** The location of the original force sensors on the testing rig

As noted previously, the force sensors used with the original testing rig were returned to the university and therefore missing from the current setup.

The bracket for the in-going force sensor with its thin-walled cross-section seemed unsuitable for the load scenario and could very likely be prone to twisting, as noted previously.

It was not feasible to acquire new force sensors before evaluating the rig as a whole, as any necessary modifications could call for different specifications or geometries.

## 4.3 Task list

Based on the above findings it was deemed appropriate to create a task list with priorities:

1. An eigenfrequency analysis should be performed on the frame to check for frequencies near the observed fluctuations.
2. The motor had obvious issues that would affect all the other sub-systems. It therefore seemed logical to start diagnosing the motor problems first, as it could potentially be the root cause of other issues. An obvious next step would be to explore the configuration of the motor and inverter.
3. As the brake system had high dependency on the function of the V-belt transmission, it would not be feasible to spend time on improving it before the belt system was sorted.
4. Following the same logic, the force sensor specifications for in-going and out-going measurements would depend on any changes made to the motor- and the brake system, respectively.
5. The frame would likely be compatible with any changes made to the sub-systems, requiring only little modification. At this point it therefore seemed reasonable to leave the frame unchanged.

# Chapter 5

# Solution selection

The task list in section 4.3 defined the basic priorities for this chapter, but could obviously be revised throughout the project phase as the testing rig was improved. The first step was to examine the testing rig's eigenfrequencies.

## 5.1 Testing rig frame

An eigenvalue analysis was performed on the testing rig frame, including its two top plates. The analysis was performed on using an SOL103 Real Eigenvalues solver in Siemens NX. The top plates were meshed with swept meshed with 10 mm CHEXA(8) elements and the frame was meshed with 20 mm CTETRA(10) elements (the frame was also tested with a midsurface mesh, yielding similar results). The simulation file is shown in Figure 5.1. The complete results are detailed Appendix C.3. In short, the lowest resonance frequency of 38 Hz was many times higher than the observed fluctuations in the testing rig, and probably not contributing to the observed instability.

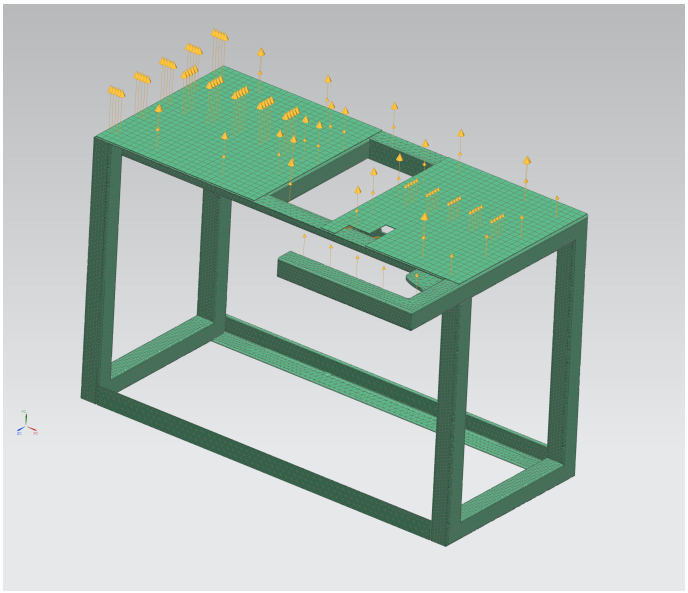

**Figure 5.1:** The .sim file for the testing rig frame with meshes and gluing.

## 5.2 Motor & inverter

The motor and inverter were supplied from the same distributor and compatible on paper. The initial function test was, however, indicating that the motor and inverter were running with a sub-optimal configuration. The first step was therefore to diagnose the motor and inverter setup.

### 5.2.1 Diagnosing motor and inverter settings

Studying the product documentation [16] for the inverter revealed that it was not correctly set up for the motor specification, but rather set up with the standard configuration.

As delivered, the inverter was configured for operation in TN or TT power networks. Investigation revealed that this was not changed, even though the workplace had an IT power network. The inverter was therefore configured to the IT-network setting by re-positioning two jumpers cables in the frequency inverter.

The inverter consisted of two parts, the inverter itself and a digital control panel. The control panel was used to configure the internal settings on the inverter, but also had a memory function for saving parameter sets. The old configuration was therefore saved before altering the original configuration, making it easier to compare settings and track progress.

The motor parameters P201 - P209 were first set manually to match the identification plate on the motor. A stator measurement was then performed by using parameter P220, as recommended by the product documentation. This lead to the following settings:

- P201: Nominal motor frequency = 50 Hz
- P202: Nominal motor speed = 1385 rpm
- P202: Nominal motor current = 3.8 A
- P204: Nominal motor voltage = 230 V
- P205: Nominal motor power = 1.10 kW
- P206: Motor cos $\phi$ = 0.78
- P207: Motor circuit = 1 (delta)
- P208: Stator resistance = 6.28 W
- P209: No load current = 3.0 A

### 5.2.2 Operation mode

After consulting the product documentation, it was discovered that the SK500e inverter only supported VFC open loop operation, popularly called ISD-control. In short, this operating mode is based on a voltage-governed flux oriented control method, without using encoders. The control is based on fixed parameters and the measurement result of actual electrical values [16].

Hence, the inverter had no option for PI-control based on motor speed data from an incremental encoder. In addition, the current motor did not have a built in encoder.

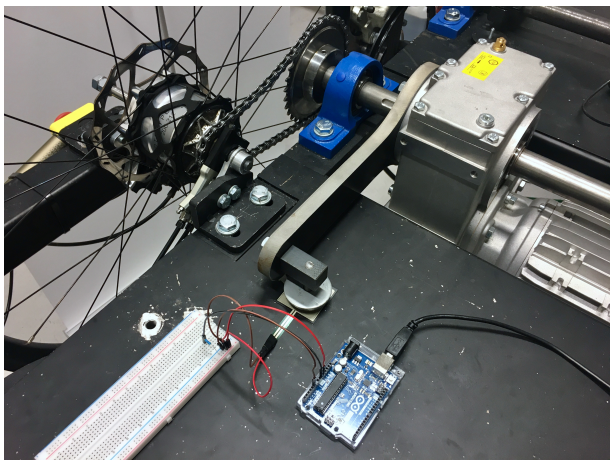

**Figure 5.2:** Measuring different motor configurations with a force sensitive resistor.

### 5.2.3 Results

The initial comparison between the original settings of the inverter and the new configuration was performed in a visual manner, by using a rubber spring as explained in Section 4.2.2. The comparison was done with a set braking force, by using a cable tie to compress the brake lever on the temporary, direct mounted disc brake.

The results indicated considerable improvement, simply observed by much less movement in the rubber dome. In addition, the motor was now much more responsive for changes in braking torque. This was also verified with the company engineers who had previous experience with the testing rig.

Because the original force sensors were missing, a quick measurement was also performed to measure the fluctuations from the in-going torque arm by using an Arduino with a force sensing resistor (FSR), as depicted in Figure 5.2.

Unfortunately, the FSR turned out to be unsuited for measuring dynamic loads because of a considerable amount of measurement noise. Plotting the results showed a slight improvement for the new invert settings, but because of the uncertainty concerning the measurements, this was not explored further.

### 5.2.4 Determining further options

While the results from the foregoing parameter adjustments seemed promising, the lack of PI-control was an evident problem. An effort was there made to determine additional options, as well as the cost of replacing the motor and inverter.

After contacting the distributor, it was confirmed that both the motor and inverter were incompatible with PI speed control. The distributor had certain add-on encoders but none where compatible with the current motor.

Exploring other markets confirmed that custom encoder solutions for motors existed, but were costly and required physically modifying the motor spindle. Moreover, this would require running an external PI-control to control the frequency setting on the inverter. The outcome would be highly uncertain and this was not examined further.

The safest solution would therefore be to replace both the current motor and inverter with and encoder-enabled motor and a PI-compatible inverter. An enquiry was therefore sent to the distributor, resulting in the following offer:

- SK80 encoder enabled motor: 4200 NOK
- SK520 (or above) PI-enabled inverter: 4500 NOK or more

Because of the high cost related to replacing the motor and inverter, it was decided to keep the current motor/inverter setup until further investigation of the testing rig was performed.

## 5.3 Power transmission

This section discusses solutions related to the two power transmissions in the testing rig, namely the chain transmission from the motor to the gearhub and the V-belt transmission from the gearhub (rim) to the braking system.

### 5.3.1 Chain transmission

While Myklestad [9] recognized the radial trueness of the motor sprocket as a potential problem, the function test did not indicate that this was an issue that contributed to the instability of the testing rig – especially after improving the motor configuration. A brief discussion on possible solutions is still appropriate.

Mounting the motor directly would always be beneficial in terms of bypassing efficiency losses and irregularities related to the chain transmission. While the chain losses could always be compensated for in calibration, irregularities from radial/lateral trueness and the variable radius of a chain sprocket would always be present as noise in the measurements. The latter is called the chain polygon effect [17]:

As a sprocket rotates, the effective radius varies between a minimum and maximum radius. This is illustrated in Figure 5.3. The sprocket rotational speed will therefore oscillate if driven by a chain with constant speed. This would visible as oscillating forces on the load cells. The effect is worse for small sprocket sizes as the ratio $\frac{r_{\max}}{r_{\min}}$ increases.

The tangential speed of a rotating object is given by:

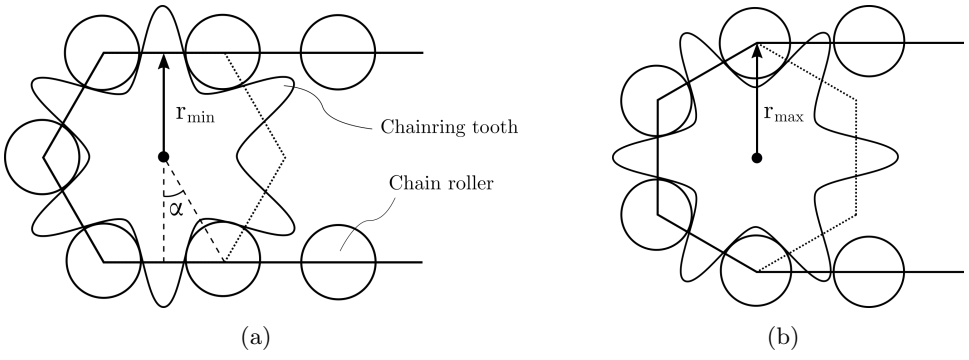


**Figure 5.3:** The chain polygon effect: the rotation of the sprocket determines the effective radius between $r_{\min}$ (a) and $r_{\max}$ (b)

$$v_{\text{tangent}} = \omega \cdot r \tag{5.1}$$

Hence, the tangential speed difference is proportional to the difference $\Delta r = r_{\max} - r_{\min}$ From Figure 5.3(b), we can see that

$$r_{\min} = cos(\alpha) \cdot r_{\max} \tag{5.2}$$

and

$$\alpha = \frac{360}{2 \cdot z} \tag{5.3}$$

, where z denotes the number of teeth for the sprocket. We can therefore write

$$\Delta r = r_{\max} \cdot (1 - cos(\frac{180}{z}) \tag{5.4}$$

For a 16 tooth cog, $r_{\max}$ was measured to 32,3 mm and consequently $\Delta r = 0.62$ mm. The tangential speed would therefore oscillate with a percentage difference of $\frac{0.62}{32.3} = 1.92\%$. The 32T sprocket would also contribute to the oscillations, albeit with a smaller contribution. The maximum tangential speed would occur when both sprockets are rotated such that $r = r_{\max}$.

Cooupling the motor directly to the gear hub would naturally avoid these oscillations. However, as discovered in the gearhub study in Section 3.1, the vast diversity of sprocket interfaces would make this modification quite complicated. Moreover, having the ability to connect the original shifting actuator would be difficult to combine with a direct drive motor solution. At the very least, this would require highly specialized hardware for each gearhub.

Consequently, this was not explored further at the current process stage.

### 5.3.2 V-belt transmission

The function test showed that the V-belt transmission on the testing rig was highly problematic in its current configuration.

Myklestad [9] explored several possible concepts related to the braking system and out-going transmission. His main findings can be summarized in the following points:

- **Torque transmission via original brake rotor (direct mount):** Heat accumulation if running over time would be a problem.
- **Torque transmission via tire (friction coupling):** Many large error sources, including slip, tire deformation, vibrations from tire and increased bearing losses due weight on tire/rim.
- **Torque transmission via rim (friction coupling):** Difficult to obtain a friction wheel that fits the rim. The required contact pressure would exceed the yield strength of most rubber compounds.
- **Torque transmission via rim (belt transmission):** Difficult to find compatible belt profile, but sufficient wrap and tension on the belt could compensate for this. The belt stretching on the rim would generate an unknown efficiency loss.

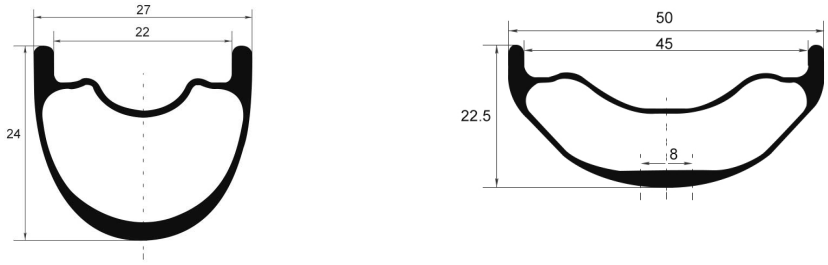


(a) 22mm wide rim

(b) 45mm wide rim

**Figure 5.4:** Various rim profiles.

The final choice was to use the belt transmission, despite its downsides.

A key requirement identified in Section 3.3 was the compatibility with different rim sizes and rim profiles. The former could be remedied by adjusting the belt tensioner, meaning the testing rig could support 26", 27.5" and 29" rim sizes.

The compatibility with different rim profiles, however, was not well supported with the current belt transmission. Figure 5.4 shows two different rim profiles. The first one represents a typical MTB or Touring bike rim with 22 mm internal width and a clearly defined rim well (center section). The second rim profile in Figure 5.4(b) is a wider variant, capable of supporting 3.0 inch wide tires. It has a much wider rim well that is poorly suited for a belt transmission. Wider rim sizes are becoming increasingly popular, and it is reasonable to believe that many future gearhubs will be built on such rims.

Supporting both rim profiles with a belt transmission would involve designing some instance of an adaptive rim strip, finding a V-belt profile that was compatible with all rims or simply having multiple V-belts for different rim profiles. The latter would of course be highly inconvenient as both of the belt pulleys would need to be replaced each time a new wheel was tested.

A considerable effort was made in researching this matter, including consulting well renowned suppliers in Norway and abroad. This resulted in testing several different belt configurations, some of which are depicted in Figure 5.5.

- Continental VFO Pioner 10 mm V-belt with flat, toothed and lower flat profile
- Continental VFO Pioner 13 mm V-belt with toothed and lower flat profile
- BEHA PU85 A green round belt with a 10 mm

The V-belts were tested both with toothed and flat profiles, both with mixed results. Even with a modified lower, flat profile, the belt had a frequent tendency to flip and pull to one side of the rim as shown in Figure 4.2.

A circular rim strip was therefore tested – the BEHA PU85 was not strong enough to sustain max braking torque, but provided a good example of the expected performance from a round belt. It still had a tendency to pull to one side, but did not flip like the V-belt options.

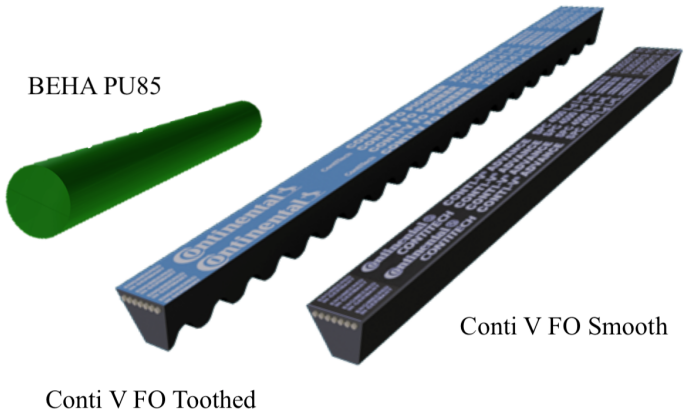


**Figure 5.5:** Several belt profiles were tested

The main difficulty with round belts was finding a strong belt with little elasticity – most round belts have some built-in elasticity and this is not suitable for the purpose in question. The problem with an elastic strip was that it would enter and exit the rim with different belt tension, meaning that the belt would effectively "creep" on the rim bed. This would generate a large efficiency loss that would depend on the braking torque.

Another problem, related to requirement no. 14 in Section 3.3, was the dependency on correct alignment and a true wheel. Even with the circular belt, the testing rig was very sensitive to wheel trueness.

To summarize, it would be highly desirable to skip the current V-belt transmission entirely in favour of a direct drive brake system.

## 5.4 Brake system

Discarding the outgoing V-belt transmission would of course depend entirely on constructing a suitable, direct drive brake system, and this is therefore discussed next.

A directly mounted brake system would essentially brake the hub and rim directly. The current brake system was tailor made for the V-belt transmission and therefore incompatible. As detailed in Section 5.3.2, Myklestad [9] explored several options for braking the rim directly but found multiple drawbacks. Different rim sizes and profiles would further complicate this matter, and the decision was therefore to study possible solutions for a direct mount brake system directly coupled to the gearhub.

## 5.5 Requirements overview

The previously defined requirements (Section 3.3) would impose some design constraints, but at the same time be a useful guide in the conceptualization phase. The following requirements were identified as relevant for the braking system:

- Requirement 1, sensitivity of $\pm 0.5\%$

| Gear ratios | | | | | 300W with 60RPM | | 100W with 120RPM | |
|---|---|---|---|---|---|---|---|---|
| Gear | $i_{gearhub}$ | $i_{motor-gearhub}$ | $i_{gearhub-brake}$ | $i_{total}$ | RPM | Torque [Nm] | RPM | Torque [Nm] |
| 1 | 0,27 | 2 | 1 | 0,54 | 16,2 | 235,7 | 64,8 | 14,7 |
| 2 | 0,36 | 2 | 1 | 0,72 | 21,6 | 176,8 | 86,4 | 11,0 |
| 3 | 0,46 | 2 | 1 | 0,92 | 27,6 | 138,4 | 110,4 | 8,6 |
| 4 | 0,55 | 2 | 1 | 1,1 | 33 | 115,7 | 132 | 7,2 |
| 5 | 0,64 | 2 | 1 | 1,28 | 38,4 | 99,5 | 153,6 | 6,2 |
| 6 | 0,73 | 2 | 1 | 1,46 | 43,8 | 87,2 | 175,2 | 5,4 |
| 7 | 0,83 | 2 | 1 | 1,66 | 49,8 | 76,7 | 199,2 | 4,8 |
| 8 | 0,92 | 2 | 1 | 1,84 | 55,2 | 69,2 | 220,8 | 4,3 |
| 9 | 1,01 | 2 | 1 | 2,02 | 60,6 | 63,0 | 242,4 | 3,9 |
| 10 | 1,11 | 2 | 1 | 2,22 | 66,6 | 57,3 | 266,4 | 3,6 |
| 11 | 1,2 | 2 | 1 | 2,4 | 72 | 53,0 | 288 | 3,3 |
| 12 | 1,29 | 2 | 1 | 2,58 | 77,4 | 49,3 | 309,6 | 3,1 |
| 13 | 1,39 | 2 | 1 | 2,78 | 83,4 | 45,8 | 333,6 | 2,9 |
| 14 | 1,48 | 2 | 1 | 2,96 | 88,8 | 43,0 | 355,2 | 2,7 |

**Table 5.1:** Direct braking torque for different gear speeds and power levels. Note that the gear ratios are inverse from the notation in eq. 2.1

- Requirement 9, quick wheel removal/installation
- Requirement 13, test hubs without rim
- Requirement 14, wheel true dependency
- Requirement 15, Kindernay XIV/VII compatibility

In addition, requirements for the actual braking torque also had to be considered. The most extreme load cases for the braking system (considering all 14 gearhub speeds) was the maximum (400 W at 30 rpm) and minimum (100 W at 120 rpm) braking scenarios. The motor torque is calculated with the relation

$$\tau_{motor} = \frac{P_{motor}}{\frac{\pi}{30} \cdot \text{ rpm}} \tag{5.5}$$

Considering the above load cases, this computes to the following numbers:

$$\tau_{\text{motor, max}} = 127.3 \text{ Nm (400 W, 30 rpm)} \tag{5.6}$$

$$\tau_{\text{motor, min}} = 7.95 \text{ Nm (100 W, 120 rpm)} \tag{5.7}$$

For the braking torque, we have the relation

$$\tau_{\text{brake}} = \frac{\tau_{\text{motor}}}{i_{\text{motor-gearhub}} \cdot i_{\text{gearhub}} \cdot i_{\text{wheel-brake}}} = \frac{\tau_{\text{motor}}}{i_{\text{total}}} \tag{5.8}$$

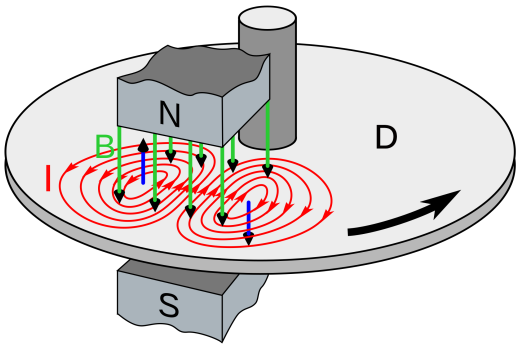


**Figure 5.6:** The principle of eddy-current braking systems. Adopted from Wikimedia Commons [19].

The previous braking system had a gear ratio $i_{\text{brake}} = 2.4$, while a directly mounted system would naturally have a gear ratio of $i_{\text{brake}} = 1$. As shown in Table 5.1, a direct drive system would need more than twice the braking torque, or $\tau_{\text{max}} = 235.8$ Nm. However, it would also need to support a minimum braking torque, $\tau_{\text{min}} = 2.7$ Nm.

### 5.5.1 Concepts

The dispersion between maximum and minimum torque requirements demanded an accurate, yet powerful braking system and therefore excluded many possible braking solutions – something that Myklestad discovered in his conceptualization phase [9]:

- **Hydraulic pump brake:** High cost, too low braking torque (at low rpm)
- **Water brake:** Few options for regulating torque at various rpm
- **Electrical generator brake:** Difficult to obtain a generator with satisfactory torque requirements (max/min)
- **Magnetic powder brake:** Not satisfying max and min torque requirement

The author did a brief study of the above braking systems and came to similar conclusions. In addition, the above systems were unsuited for directly mounted brake systems, especially considering the geometry of the relevant gearhubs and the testing rig. The two most promising solutions will be discussed next, namely eddy current brakes and friction brakes.

#### Eddy current brakes

Eddy current brakes (Norwegian: Virvelstrømsbrems) were not considered in Myklestads [9] conseptualization phase. They come in many different shapes and sizes, with a wide utility of applications. Common uses include train brakes, roller coasters and industrial machinery. They are based on the principle of utilizing the electromagnetic force between a magnet (electro or permanent) and a nearby conductive object [18]. In the current context, the conducting object could be a braking rotor that simply attached directly to the gearhub. The magnets can be either electro- or permanent magnets and the conductive object does not need to be magnetic. As shown in Figure 5.6, the effect is due to eddy currents that are induced in the conductor, and the energy is essentially dissipated as heat. The braking force increases linearly with speed up to a certain limit where it becomes non-linear.

Eddy current brakes fall within the field of electrical engineering and is somewhat outside the academic discipline of the author. Consulting relevant literature revealed that an accurate calculation involved numerous parameters.

Hukkelås [18] studied braking torque from Eddy-current braking systems and gave an orderly overview of the different theories on the subject. His calculations were based on Gosline and Hayward's [20] model, primarily because of its simplicity:

$$\tau_{\text{brake}} = n\frac{\text{P}_\text{b}}{\dot{\theta}} = n\frac{\pi\sigma}{4}D^2 dB^2 R^2 \dot{\theta} \tag{5.9}$$

where

- $\tau_{\text{brake}}$ is the braking torque
- $n$ is the number of magnets
- $\sigma$ [S/m] is the specific conductance
- $D$ [m] is the magnet diameter
- $d$ [m] is the disc thickness
- $B$ [T] is the magnetic field
- $R$ [m] is the effective disc radius
- $\dot{\theta}$ [rad/s] is the angular velocity

The braking torque was then calculated with the following assumptions

- There was enough room for a brake rotor with $d = 550$ mm in the testing rig
- The rotor could be machined or water-cut from aluminum with $d = 0.015$ m and $\sigma = 35.5 \cdot 10^6$ [S/m]
- Four N52 Neodym permanent magnets with $B = 0.6$ T and $D = 0.055$ m could be used in a brake caliper

Per table 5.1, the gearhub would spin with 16.2rpm = 1.7 $\frac{\text{rad}}{\text{s}}$ at 400 W and 30 rpm from the motor. Inserting into equation 5.9 yields

$$\tau_{\text{brake}} = 4 \cdot \frac{\pi \cdot 35.5 \cdot 10^6}{4} 0.055^2 \cdot 0.02 \cdot 0.6^2 \cdot 0.25^2 \cdot 1.7 = 258 \text{ Nm} \tag{5.10}$$

The validity of this result was highly questionable, for several reasons. Gosline and Hayward's [20] model does not include the effect of fringing [18], nor account for the non-linear "skin-effect" seen above certain rotational speeds. Furthermore, the effect of heat in the braking rotor and braking force was not considered. Hukkelås [18] identified very large errors between the aforementioned model and experimental data, the latter showing less than half the braking torque for lower rotational speeds.

To get a better overview of the spatial constraints, a quick sketch was modeled in Solidworks, shown in Figure 5.7. This indicated that the brake rotor and caliper would take up significant space in the axial direction, thus limiting the compatibility with wider bicycle rims. The size and weight of the braking rotor could also be a concern. Consulting the company engineers revealed that this was not a problem with the Kindernay gearhubs, but it would still impact usability of the rig to some degree.

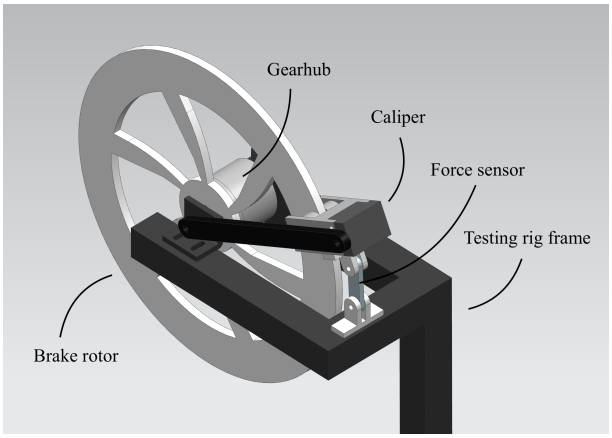


**Figure 5.7:** Sketch of Eddy current brake system in a cut-out of the current frame.

### Friction brake

A friction brake works by absorbing energy from a moving object, usually in the form of friction. Common applications are bicycle-, motorcycle and automotive vehicle brakes. The latter was what Myklestad [9] ended up using, because of its ease of use, predictability and robustness.

In the context of a directly mounted brake system, a friction brake would imply using a steel rotor that could be coupled directly to the gearhub. This would somewhat limit the rotor thickness because of the material density, and therefore high weight (especially compared to the aluminum disc discussed in the previous section). Brake systems from hydraulic bicycle or motorcycle brakes could be well suited as they utilize rotors with limited thicknesses, from 1.8 to 2.0 mm on bicycles and 3-4 mm on motorcycles.

The torque calculation on friction brakes involves far less variables compared to the Eddy-current brakes. Assuming a regular four-piston bicycle disc brake caliper with $D_{\text{piston}} = 17$ mm we have a total piston area $D_{\text{pi, total}} = 907$ mm$^2$.

The maximum required braking torque was previously calculated to be $\tau_{max} = 235.7$ Nm. If the rotor has a 550 mm effective diameter, the braking force at the caliper is

$$F_{\text{brake}} = \frac{\tau_{\text{max}}}{r_{\text{mid}}} = \frac{235.7 \text{ Nm}}{275 \text{ mm}} = 857 \text{ N} \tag{5.11}$$

This corresponds to a fluid pressure of

$$P_{\text{brake}} = \frac{F_{\text{brake}}}{\mu \cdot \pi \frac{d_{\text{piston}}}{4}} \cdot n = \frac{857}{0.4 \cdot \pi \frac{17^2}{4}} \cdot 4 = 2.36 \text{ MPa} \tag{5.12}$$

or 342 psi, assuming $\mu = 0.4$. This was well within the maximum pressure of modern brake hoses that have limits above 6000 psi [21].

To get an idea of how much pressure one would have to apply to the brake lever, the following calculation was performed:

The diameter of a typical bicycle brake lever master cylinder is $d_{\text{master}} = 10$ mm, giving $A_{\text{master}} = \pi \cdot \frac{10^2}{4}$ mm$^2$ = 78.5 mm$^2$. Hence, the force on the master piston would be

$$F_{\text{master}} = P_{\text{brake}} \cdot A_{\text{master}} = 2.36 \text{ MPa} \cdot 78.5 \text{ mm}^2 = 185.3 \text{ N} \tag{5.13}$$

Considering a reduction ratio of 1/6 in the brake lever, this would require about 30 N or 3 kg of pressure on the lever – well within operating limits.

The primary challenge with friction brakes in the present application would be heat accumulation because of continuous braking. Heat will dissipate from the braking rotor in the form of radiation and the cooling is highly dependant on the airflow through the brake rotor. This can be improved by designing radial fins into the braking rotor. Calculating the actual cooling effect is therefore highly dependant on the rotor geometry, but a "worst case" scenario for heat accumulation can be always be estimated under the assumption of no cooling. Heat accumulation, or thermal energy in its simplest form is simply added heat divided by mass and specific heat capacity, or

$$\Delta T = \frac{Q}{m \cdot c} \tag{5.14}$$

For the highest load scenario, $P = 400$ W $= 400 \frac{\text{J}}{\text{s}}$ we can calculate the heat accumulation per second, or

$$\frac{\Delta T}{s} = \frac{Q}{m \cdot c \cdot s} \tag{5.15}$$

The testing rig could accommodate a rotor size of at least 550 mm. With 2 mm thickness that equals a volume of roughly $V = 4.75 \cdot 10^{-4}$ m$^3$ and an approximate weight of $m = 3700$ g. Assuming 5 minutes = 400 s of sustained loading and the specific heat capacity for steel, $c \approx 490 \frac{\text{J}}{\text{kg} \cdot \text{K}}$ [22], we get

$$\Delta T_{400s} = \frac{400 \frac{\text{J}}{\text{s}}}{490 \frac{\text{J}}{\text{kg} \cdot \text{K}} \cdot 3.7 \text{kg}} \cdot 400 \text{s} = 88.25 \text{K} \tag{5.16}$$

Given a 25° ambient temperature, this will give a total temperature of 125°, well within the operating temperature of standard disc brake systems. Since the heat accumulation is directly proportional to the time, the temperature would in theory increase indefinitely for continuous loading, meaning a 20 minute test would increase the temperature to $25° + 353° = 378°$.

In reality however, the temperature would stabilize at some point due to cooling effects. It would therefore be important to maximize the disc size, surface area and ventilation slots, but without removing to much material on the brake. Lastly, any tests longer than 5 minutes would seldom be necessary. It was therefore reasonable to assume that temperature would not be an issue.

## 5.6 Force sensors

Regardless of any changes to the testing rig, it would still be necessary with in-going and outgoing force measurements to obtain efficiency data. The previous force sensors were so-called beam load cells, as shown in Figure 5.8(a). These are primarily used for high-accuracy weighing applications and were therefore well suited on paper.

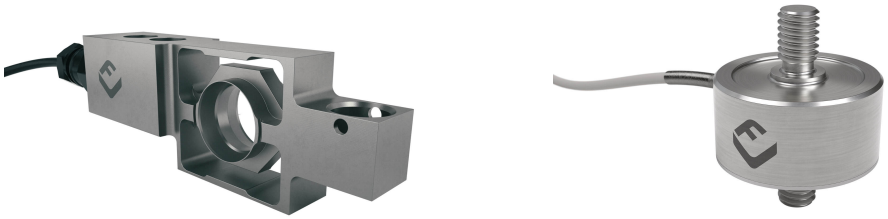

(a) Beam load cell

(b) Axial force sensor

**Figure 5.8:** Examples of different types of force sensors. The renders are adopted from Flintec [23].

The problem with the previous implementation however, was the uncertainty of the point of attack, especially in the out-going force sensor. The point load was transferred from the torque arms with a large bolt size and it was therefore difficult to determine the exact length of the torque arm. The supporting bracket for the in-going sensor was also too flexible, as noted previously.

A better solution would be to employ an axial force sensor combined with female rod end bearings, as depicted in Figure 5.8(b). This would have several advantages:

- The axial force sensors would be more space efficient
- The rod end bearings would provide axial adjustment, making assembly straightforward
- The rod end bearings would ensure that only axial forces were transmitted to the load cell
- The exact position of the point of attack would be straightforward to determine

The exact placement and specification of the force sensors would be highly dependant on any changes to the motor and braking system. This is detailed in the next chapter.

### 5.6.1 Summary

Based on the preceding discoveries it was decided to dismiss the V-belt transmission in favour of a new brake system, coupled directly to the gear hub. After studying several options, the most compelling concept was the use of a friction brake system combined with a large rotor. The Eddy current braking system seemed somewhat promising, but the uncertainty surrounding the calculations and general performance was problematic. This, combined with a high material cost for the braking rotor made the friction brake an obvious choice. The motor issues were to a large degree improved by using correct inverter configurations, but a new assessment would have to be made after implementing a new braking system.

# Chapter 6

# Brake system solution implementation

This chapter describes the design and conceptualization of the directly mounted braking system and the force transducers on the testing rig. It is based on the discoveries made in previous sections.

## 6.1 Brake system – analytical model

The decision from the solution selection process (Chapter 5) was to implement a direct mount brake, either as a friction brake or an eddy-current brake. While the requirements imposed some clear construction guidelines, the design space was still wide. The first step in this process was to consider the analytical aspect of a direct mount brake.

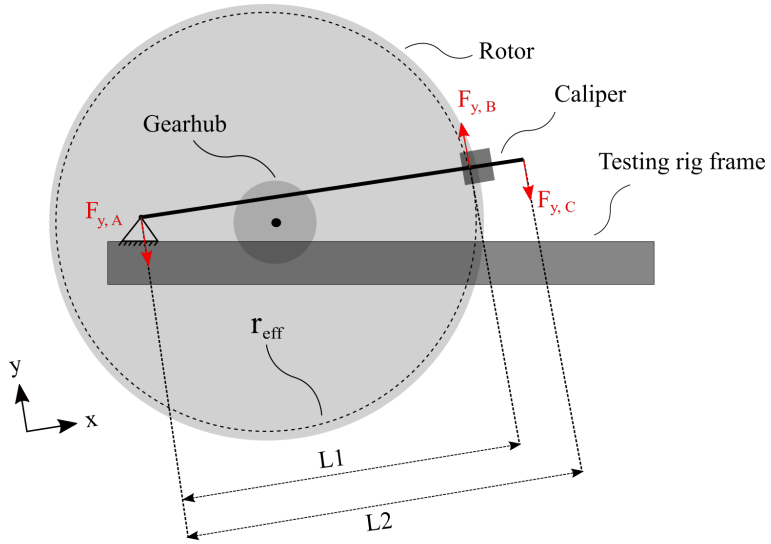


**Figure 6.1:** Analytical model 1.

A direct mount brake will imply the use of a caliper and a brake rotor. The braking forces applied to the rotor will determine the power output from the motor, which will simply draw more current as more braking is applied. Hence, if increasing the braking force, the motor has to run at a higher power level to maintain the rotational speed of the wheel and brake.

The braking power is simply

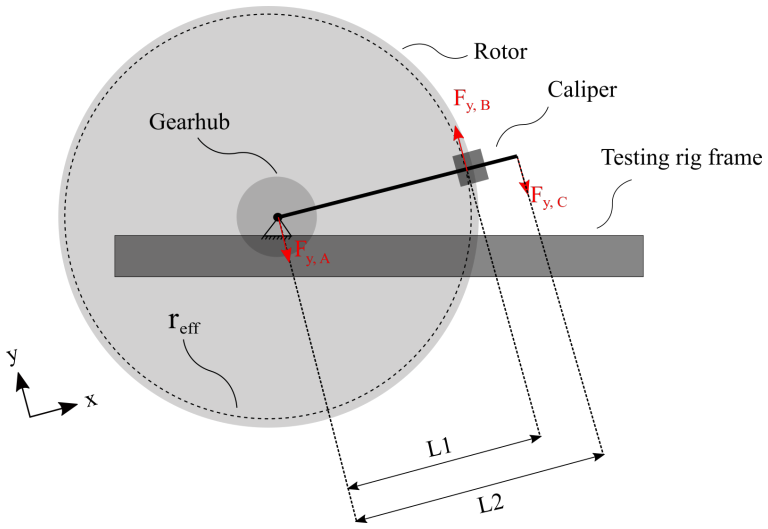


**Figure 6.2:** Analytical model 2

$$P_{\text{brake}} = \tau_{\text{brake}} \cdot \omega = \tau_{\text{brake}} \cdot (\frac{2\pi}{60} \cdot \text{ rpm}) \tag{6.1}$$

There are several ways to measure the braking torque, the most obvious being

- Measure strain in braking rotor with strain gauge
- Measure the reaction force from the caliper with force transducer

The strain gauge measurement was considered problematic for several reasons – it would be highly dependant on having optimized rotor geometry, compensation for thermal effects and also live signal transmission from a rotating object.

Measuring reaction forces in the caliper had none of these disadvantages, but did present some challenges in itself. To compute the torque, the effective radius of the braking disc must be known:

$$\tau_{\text{brake}} = F_{\text{brake}} \cdot r_{\text{rotor, eff}} \tag{6.2}$$

Consider the concept shown in Figure 6.1, where the caliper is mounted on a solid arm that pivots freely around point A. The arm is constrained in point C by a force transducer, hence the value of $F_{y,c}$ is known. By summing the moments around point A, we get that

$$F_{\text{brake}} = F_{\text{y,B}} = \frac{L_1}{L_2} \cdot F_{\text{y,C}} \tag{6.3}$$

Here, $L_1$ is the distance from the center of the pivoting arm to the effective radius $r_{\text{rotor, eff}}$ of the braking rotor. The effective radius is simply the radius at which the combined braking force from the caliper acts on the rotor. This is highly dependant on the geometry, position and movement of the brake pads in the caliper. Hence, the values of $L_1$ and $r_{\text{rotor, eff}}$ are subject to uncertainty.

Consider instead the concept shown in Figure 6.2. Here, the pivoting point of the solid arm is centered on the axle to the gearhub, and therefore also in center of the braking rotor. This implies that $r_{\text{rotor, eff}} = L_1$. Summing the moments around point A gives

$$L_1 \cdot F_{\text{y,B}} = L_2 \cdot F_{\text{y,C}} \tag{6.4}$$

Hence, we get

$$\tau_{\text{brake}} = F_{\text{brake}} \cdot r_{\text{rotor, eff}} = F_{\text{y,B}} \cdot L_1 = F_{\text{y,C}} \cdot L_2 \tag{6.5}$$

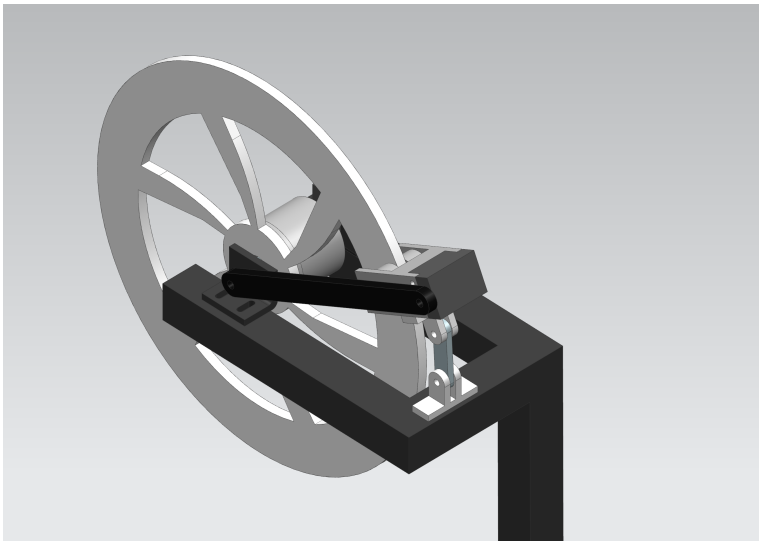

**Figure 6.3:** Direct mount brake with arm centered on hub axle.

In other words, the braking torque can be computed from the value of the force transducer and the length from the hub center to the force transducer ($L_2$). A simple 3D drawing of this concept is shown in Figure 6.3. Centering the pivoting point around the gearhub axle implies that the solid arm must be positioned to the left of the gearhub. The resulting reaction moment $M_{\text{x,A}}$ in point A will depend on the positioning of the force transducer, as shown in Figure 6.4.

The magnitude of $F_{\text{y,C}}$, and therefore $F_{\text{y,A}}$, is determined by the placement of the force transducer in the $x - y$ plane, that is, the dimensions of $L_1$ and $L_2$ in Figure 6.2. From Figure 6.4(b) we can see that

$$\frac{L_1}{L_2} = \frac{L_3}{L_4} \tag{6.6}$$

Hence, by placing the force transducer on the symmetry line in Figure 6.4(b), the reaction moment $M_{\text{x,a}}$ in point A will be eliminated. The exact position of $F_{\text{y,B}}$ would be somewhat uncertain, especially during construction. Thus, having the option to adjust the position of the force transducer in the z-direction would be a useful feature. In addition, the pivot in point A should be constructed with double ball bearings, giving structural rigidity to counteract any reaction moments $M_{\text{x,A}}$ resulting from imperfect alignment of the force transducer.

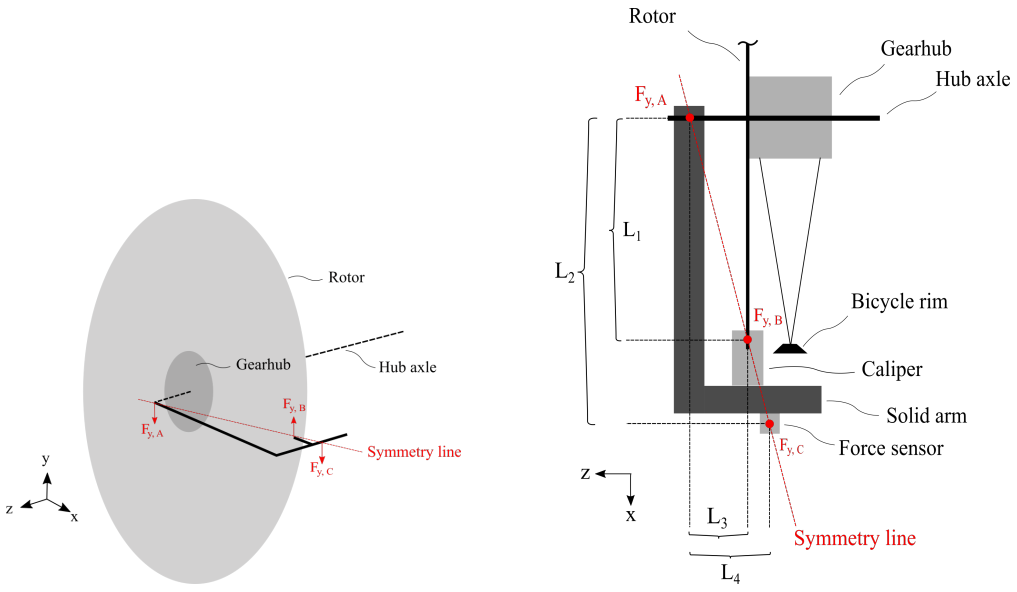


(a) 3D view (b) x-z plane

**Figure 6.4:** Alternate views of the second analytical model.

## 6.2 Considerations around the conceptualization process

As discussed in chapter 5, the two most promising direct-mount brake concepts were

- A direct mount friction brake based on a large rotor diameter and a powerful, yet small, brake caliper
- A direct mount eddy-current brake (onward termed the "ECB") based on a large rotor diameter and a permanent magnet caliper

These systems were constructed in parallel, as they built on many of the same concepts and principles. The systems were designed with the same connecting interface on the hub axle, and could therefore be tested and compared easily. The initial testing showed that the ECB system had superior stability and modulation. The friction brake solution was therefore discarded early in the conceptualization process. The following chapters focus on the conceptualization of the ECB system, but the development of the friction brake is also described briefly.

## 6.3 Eddy-current brake conceptualization

The ECB was conceptualized based on the analytical considerations in section 6.1. It would consist of four main components:

- The brake rotor, directly attached to the gearhub
- The brake caliper with magnets and adjustable engagement
- The caliper arm, enabling the caliper to pivot around the gearhub axle while providing adjustable engagement
- The actuating mechanism for the adjustable caliper engagement

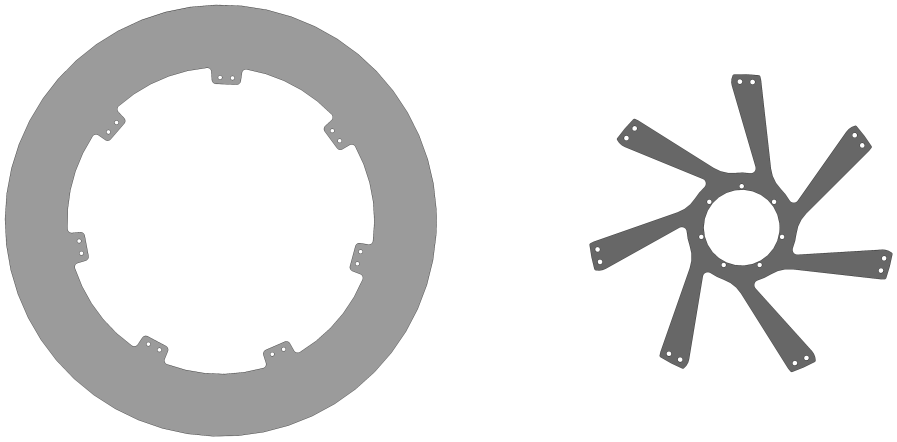

(a) Braking rotor (b) Spider connecting rotor and hub

**Figure 6.5:** The indivodual components making up the eddy current braking rotor.

The conceptualization of each component is described next.

### 6.3.1 Brake rotor

Because the braking torque is directly dependant on the rotor thickness, the ECB rotor would need a considerably thicker rotor compared to the friction brake, to deliver similar braking performance. Making the rotor out of a singe component turned out to be difficult because of the limited clearance to the hub dropout, especially with conventional IS 6-bolt rotor interfaces.

The braking rotor was therefore constructed with two main components:

1. The outer braking rotor with 15-20 mm thickness, made out of a conductive (but non-magnetic) material
2. The braking rotor spider with 2-3 mm thickness, attaching the main braking rotor to the hub interface

The outer braking rotor, shown in Figure 6.5(a), would therefore define the diameter of the complete braking rotor. The outer and inner diameters were defined to accommodate complete coverage of the caliper magnets, with some additional clearance.

The rotor spider, shown in Figure 6.5(b), was made in two different versions to fit both the XIV 7-bolt interface and the IS 6-bolt interface for regular hubs. Both version were designed with 7 spokes. The spokes were angled forwards to increase the stiffness during braking, effectively allowing the spider to tighten outwards.

The outer braking rotor and spider were designed with a common 14-bolt interface. This way, the outer braking rotor could be adapted for 7-bolt and 6-bolt hub-interfaces by swapping the spider. Adapting the outer rotor to additional rotor interface would also be possible by creating an additional spider.

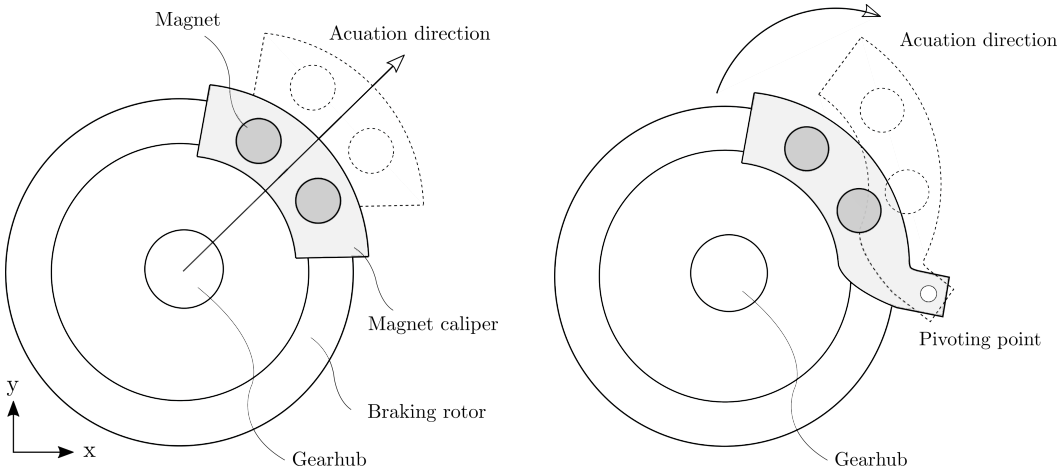


(a) Radial actuation (b) Pivoting actuation

**Figure 6.6:** Different actuation paths for the magnet caliper.

### 6.3.2 Magnet caliper

The magnet caliper would be the most complex component of the eddy-current braking system. Ideally it would support multiple requirements:

1. Easy installation and removal of magnets
2. Non-magnetic, but conductive caliper material with maximum surface area to increase braking power
3. Adjustable air gap (axial distance between magnets and rotor)
4. Sufficient clearance for wheels with wide rims (in all rim sizes)
5. Adjustable engagement versus the braking rotor, to adjust the braking torque

The solution to requirement 5 would define the overall geometry of the magnet caliper. The optimal solution to this requirement would be a caliper moving in the radial direction of the braking rotor, as shown in Figure 6.6(a). This type of design would be desirable in that the actuating mechanism would not be affected by the braking force, but would also be complicated to integrate with the analytical model illustrated in Section 6.1. To simplify the actuating mechanism and reduce the number of parts, it was decided to instead create a pivoting mechanism, as shown in Figure 6.6(b). This would increase the load on the actuating servo but could be compensated for by using a servo with more gearing, as actuating speed was of little importance.

Further conceptualization of the caliper body would depend on the type of magnet used. Figure 6.7 shows various shapes of available neodymium magnets, in regular round shapes, with bolt holes and with tapped steel holders. Using the latter two magnet shapes with bolt connections would conflict with requirement 4, because the caliper body would extend behind the rear face of the magnet and therefore limit the space for the rim. Furthermore, these magnets would need to be bigger compared to the round shaped magnet because of their reduced field strength. A regular round neodymium magnet was therefore chosen. This inferred that the magnets should be installed by securing the side face of each magnet. Requirement 1 excluded any glued connections, and a clamping mechanism was therefore necessary. Because neodymium magnets are brittle of nature, a

(a) Disc magnet

(b) Disc magnet with hole

(c) Disc magnet in threaded holder

**Figure 6.7:** Various types of neodymium magnets.

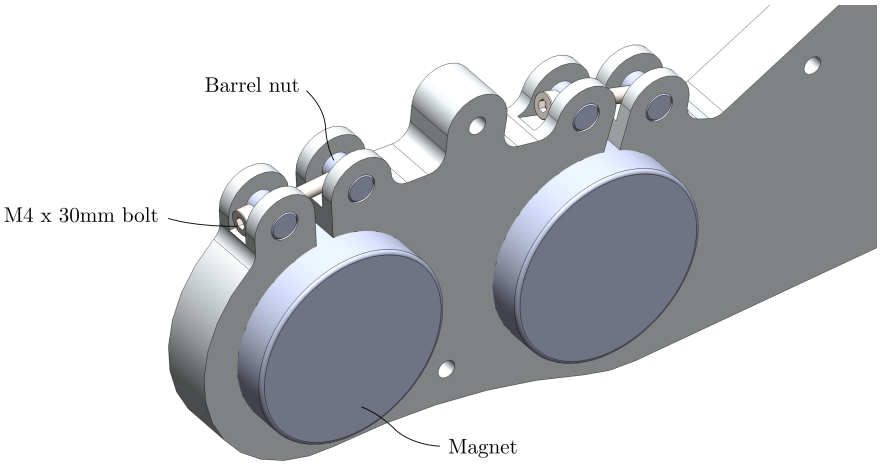


**Figure 6.8:** The magnet clamping mechanism in the ECB caliper.

set screw design could potentially damage the magnet. The clamping mechanism therefore needed to exert even pressure on the face of the magnet – this could be done in multiple ways, the simplest one being to integrate the clamping mechanism in the geometry of the caliper, as shown in Figure 6.8. The magnets could then be secured by tightening one bolt.

The preceding discussion suggested that it could be possible to design the magnet caliper as a two-part component, where each body could be defined as a two-dimensional geometry. The two bodies would then be connected via multiple bolted connections, with spacers in between to account for the width of the brake rotor. Adjusting the length of the spacers would adjust the distance between the caliper bodies, and therefore the air gap between the magnets and the rotor – hence fulfilling requirement number 3.

For maximum performance, the two magnets in each magnet pair would be positioned in an attracting formation. Moreover, the magnet pairs would be rotated 180 degrees to each other, as shown in Figure 6.9.

### Geometry optimization

To maximize braking performance, the magnets would be placed so that they covered the braking rotor completely during maximum caliper engagement. This meant placing the magnets in a circular

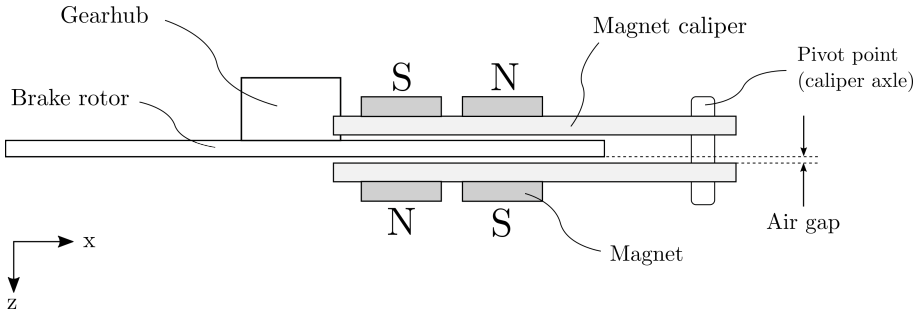


**Figure 6.9:** The magnet formation and air gap in the ECB caliper.

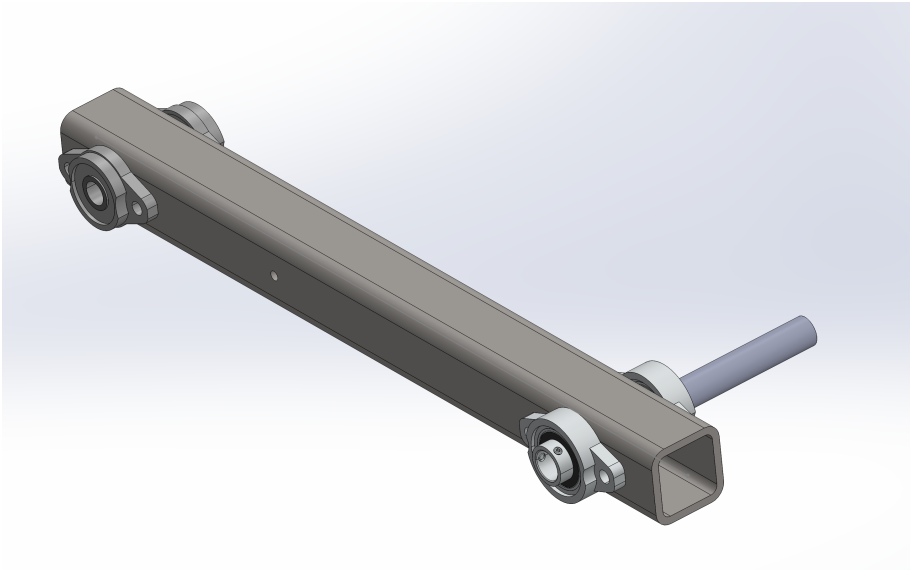

**Figure 6.10:** The caliper arm for the ECB system.

pattern, along the radius $r_{\text{eff}}$ as shown in Figure 6.11. The braking forces for each magnet pair, $F_{\text{mag},1}$ and $F_{\text{mag},2}$, would follow the tangent of the circumference to the imaginary circle with $r = r_{\text{eff}}$ during maximum caliper engagement. To minimize the load the actuating mechanism, it would be optimal to place the location of the pivoting axle such that the moment $M_{\text{C}} = 0$. This could be accomplished by placing the pivoting axle on the line of the resultant braking force, $F_{\text{mag, R}}$.

### 6.3.3 Caliper arm

The caliper arm would function as a rigid, pivoting arm that directed the braking forces into the force transducer, as previously illustrated in Figure 6.4(b).

As previously discussed, it also had to provide adjustment of the caliper in the x- and z-direction, and the force transducer location in the z-direction. It was therefore desirable to manufacture the arm with a geometry that had a decent amount of surface area, high strength and decent weight.

The caliper arm was to rotate freely around the axle of the freehub. This was accomplished by using UFL 001 flange bearings on each side of the square profile, as shown in Figure 6.10. The inner bearings of the flange bearings were rotated to minimize the overall width of the caliper arm, hence it could be positioned closer to the gearhub.

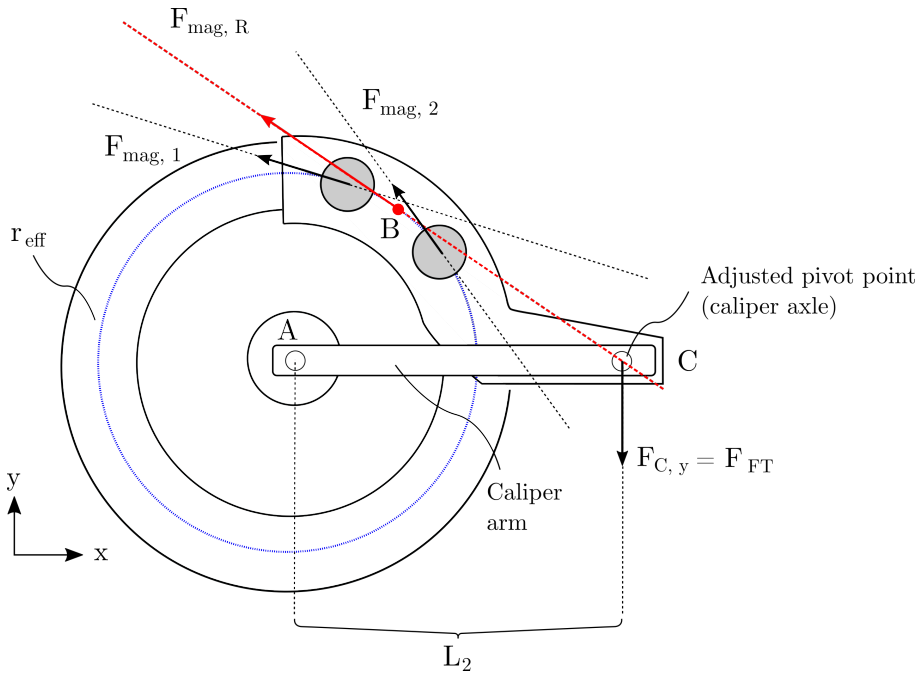


**Figure 6.11:** The forces acting on the ECB caliper during maximum brake engagement.

The arm was designed as a straight section of 40×40×4 mm S355 structural square tubing, as it had sufficient thickness for tapping and was readily available. An aluminum spacer was designed to fit inside the tubing, between the inner bearing races. This would ensure that the inner bearing races were compressed from both sides when tightening the hub axle, so that the bearings didn't bind.

The eddy current caliper arm would also need to support the rotating motion of the magnet caliper, while maintaining the necessary stiffness in all other degrees of freedom. Furthermore, it needed to provide adequate adjustability for the magnet caliper to be properly aligned to the braking rotor. Both of these requirements were met by using UFL 002 flange bearings in the opposite end of the gearhub axle.

UFL 001 and 002 flange bearings are designed for M6 bolts, but with 7 mm bolt holes. In addition, the outer bearing race can freely rotate inside the flange body. This would provide the necessary adjustability for the magnet caliper versus the braking rotor, and put less demand on the tolerance precision for the bolt holes in the caliper arm.

The magnet caliper was connected to the caliper arm by a 15 mm steel axle (onward termed the "caliper axle"), as shown in Figure 6.11. The axial position of the magnet caliper would be set by tightening the set screws on the inner bearings races of the flange bearings and thereby locking the caliper axle.

For 10×135 mm gearhubs, the brake arm would use a custom adapter, detailed in section 6.5.3.

### 6.3.4 Actuating mechanism

The actuating mechanism would be responsible for regulating the caliper engagement on the braking rotor, thereby modulating the braking power. The position of the axle location, determined in

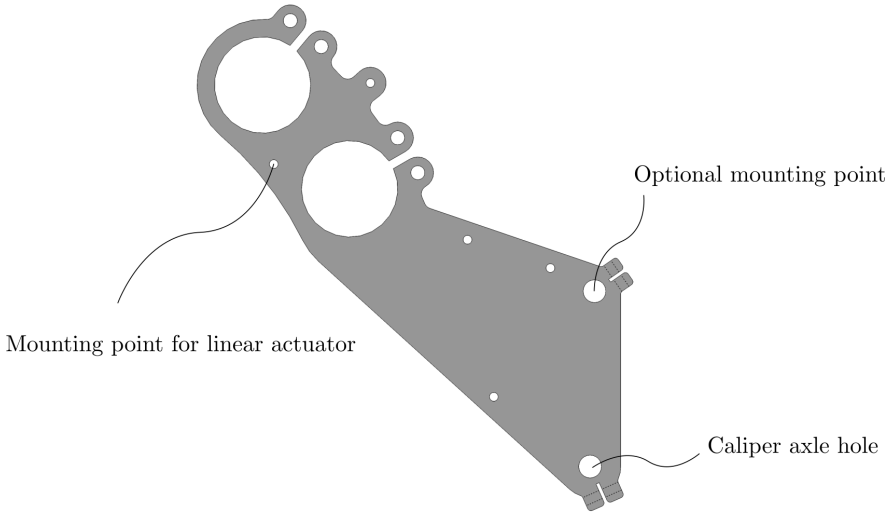


**Figure 6.12:** The finished ECB caliper geometry with actuator mounting points.

section 6.3.2, would determine the reaction force on the actuator for different caliper positions. By looking at the geometric considerations in Figure 6.11, the following conclusions were drawn:

- During maximum brake engagement, the resultant force $F_{\text{mag, R}}$ passes through the caliper axle. The resulting force on the actuator is therefore zero.
- During partial brake engagement of both magnet pairs, the resultant force $F_{\text{mag, R}}$ moves closer to the outer diameter of the braking rotor, and therefore passes through a point slightly above the caliper axle. This results in a compressive force on the actuator
- During partial engagement of *only* the magnets closest to the axle, the resultant force $F_{\text{mag, R}}$ only consists of $F_{\text{mag,2}}$. It is again therefore brought closer to the axle, reducing the compressive force on the actuator

Hence, the force on the actuator would depend on the exact location of $F_{\text{mag, R}}$, which would not move linearly with the caliper position. To completely disengage the brake during operation, the actuator needed to counteract this force. This would depend on the exact location of the resulting force, which was somewhat difficult to calculate exactly given the variable location of the braking forces $F_{\text{mag,1}}$ and $F_{\text{mag,2}}$.

Given this uncertainty, the brake caliper was designed with two mounting points as shown in Figure 6.12:

1. Mounting point 1 would support a simple linear actuator that was fastened directly on the caliper arm
2. Mounting point 2 would accept a 15 mm axle that could be extended to create a more robust actuating mechanism, in the event that the linear actuator for mounting point 1 was insufficient

Both options were incorporated in the final design. Mounting point 1 was placed to accommodate an Actuonix P16 100 mm linear actuator with 1:256 gearing. Its low gearing ratio results in a high peak force of 300 N and a back drive force of 500 N, with the drawback of reduced actuating speed. Because the testing rig would be run at constant braking power for each test, this was of little importance.

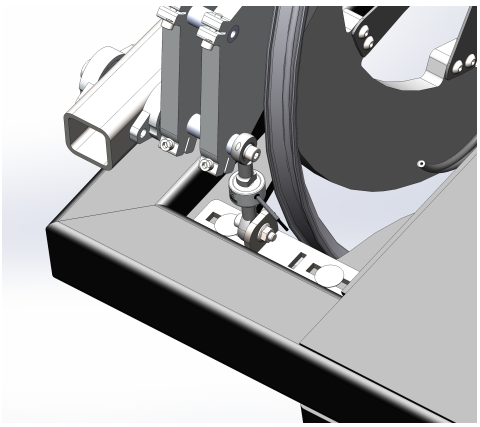

(a) Force transducer mounted with female rod ends

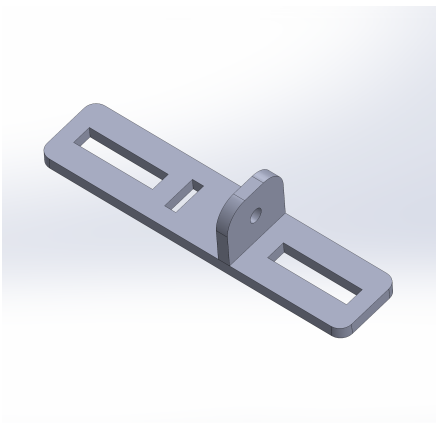

(b) The ECB force transducer bracket

**Figure 6.13:** The force transducer measuring the ECB brake power.

### 6.3.5 Force transducer

The position of the outgoing force transducer would be determined from the symmetry line according to Section 6.1. This implied the use an axial force transducer for the outgoing measurement. The outgoing force transducer would attach to the braking arm on one side and to the testing rig on the other.

The force transducer was mounted with female rod ends and mounted directly on the 15 mm steel axle that the caliper was attached to, as shown in Figure 6.13(a). A bracket was designed for connecting the force transducer to the testing rig, as shown in Figure 6.13(b). The bracket consisted of two parts that would be welded together.

Because the brake caliper would move to adjust the braking force, the static load on the force transducer would vary, depending on the brake assembly's center of gravity. This would be compensated for in the control system by taring the force transducer before each measurement at a given braking power.

Considering the maximum braking torque, the maximum force on the force transducer would be

$$F_{\text{ft, out}} = \frac{\tau_{\text{brake, max}}}{L_2} = \frac{235.7 \text{ Nm}}{0.33 \text{ m}} \approx 714 \text{ N} \tag{6.7}$$

, defining $L_2$ as in Figure 6.4(b). Similarly, the minimum braking torque $\tau_{\text{brake, min}} = 2.7$ Nm would produce a force of $F_{\text{ft , out}} = 8.2$ N

Hence, a force transducer like the Flintec Y1 [23] or HBM U9C [24] with a 1000 N capacity and 0.25% accuracy would be well suited for the maximum torque scenario. The value of $L_2$ was subject to change during the final dimensioning, but only by a few millimeters and this would not affect the choice of range for the force transducer. A high capacity force transducer would naturally have lower accuracy for low power and/or high speed measurements, and multiple sets of force transducers would be necessary if high accuracy was desired for all testing scenarios outlined in Table 5.1.

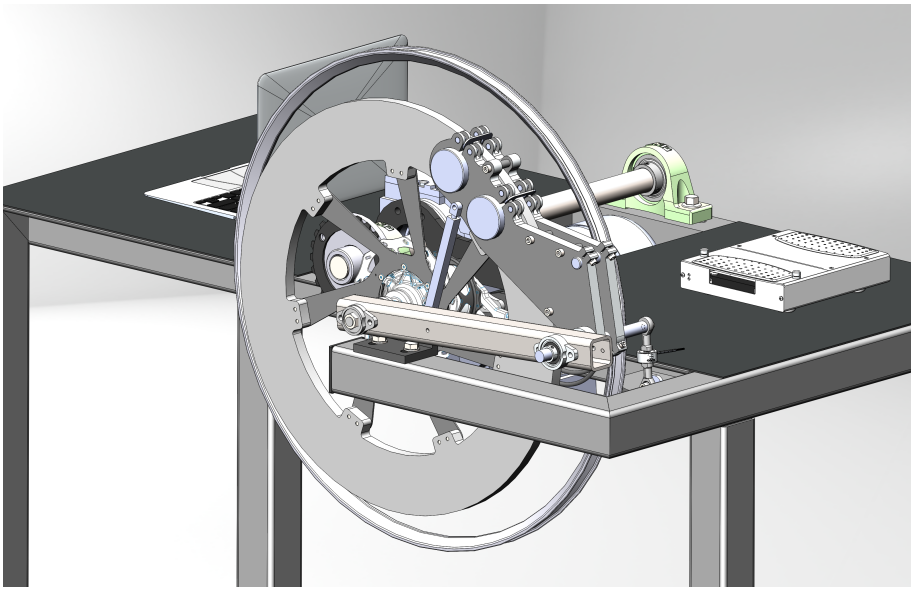

**Figure 6.14:** The finished ECB assembly after final dimensioning.

#### Force transducer position

The geometry of the ECB caliper determined the magnitude, direction and point of action for the resultant force, $F_{\text{mag, R}}$, in Figure 6.11. During maximum braking, $F_{\text{mag, R}}$ would create a moment around point A with an arm corresponding to $r_{\text{eff}}$.

In accordance with the discussion in Section 6.1 and Figure 6.4(b), the ideal position of the force transducer would therefore be:

$$L_4 = L_3 \cdot \frac{L_2}{r_{\text{eff}}} \tag{6.8}$$

### 6.3.6 Final dimensioning

The testing rigs compatibility with relevant rim sizes and widths was highly dependant on the dimensions of the braking rotor, position of the brake caliper and length of the caliper arm. After modelling all components, these parameters were fine-tuned in Solidworks by modelling various rims. This resulted in the following changes:

- The braking rotor diameter was adjusted to $d = 520$ mm and the rotor thickness was set to 15 mm
- The dimension of the neodymium magnets was set to $d = 55$ mm and $t = 25$ mm
- The inner diameter of the outer braking rotor was set to $d = 340$ mm to give sufficient coverage of the 55 mm magnets
- The overall geometry of the magnet caliper was defined with basis in the above parameters. This involved placing the magnets along $r = r_{\text{eff}}$ of the outer rotor and positioning the caliper axle location relative to the resultant force

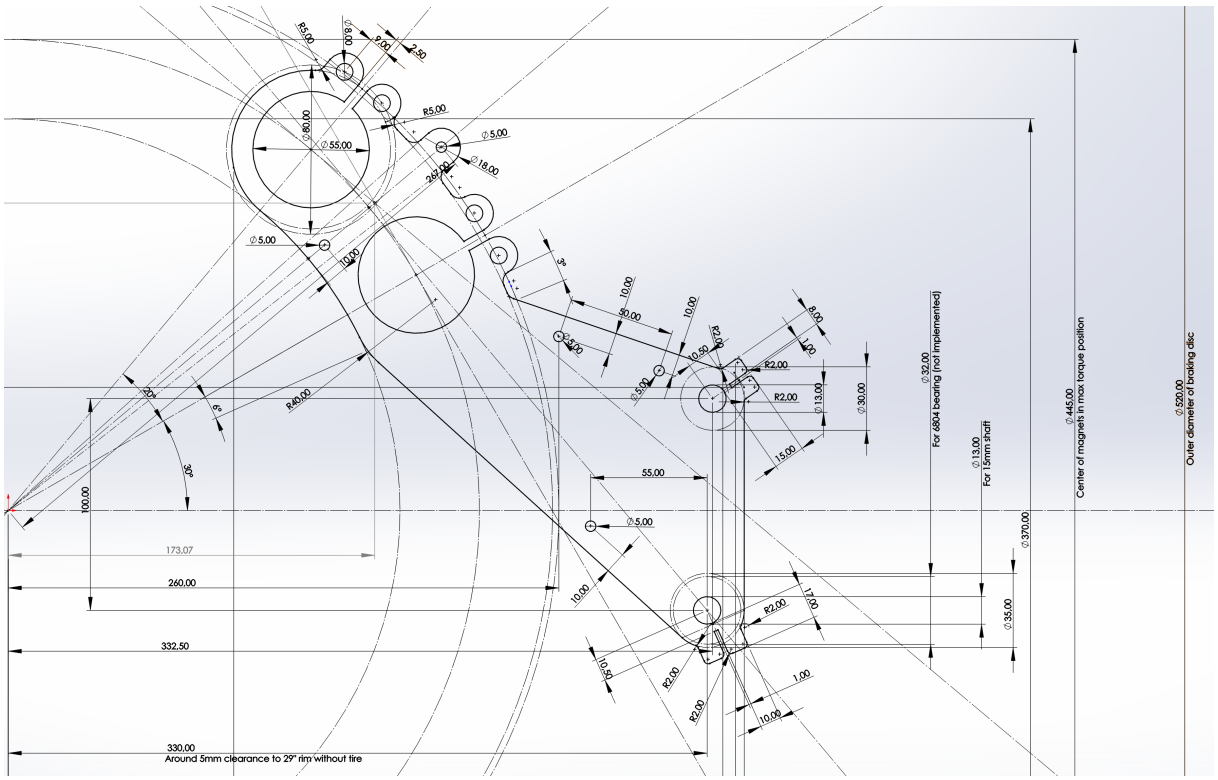


**Figure 6.15:** Final dimensionsing of the ECB system.

- The surface are of the magnet caliper bodies was maximized within the design space to maximize the braking performance
- The clamping mechanism on the magnet caliper was redesigned to use barrel nuts, simplifying the manufacturing process
- A split was added to the magnet caliper bodies, such that the caliper could be clamped securely to the axle without additional components
- The length of the caliper arm was determined from the geometry of the ECB-caliper plate and the gearhub axle location, as shown in Figure 6.15. Using equation 6.8, the force transducer was mounted 7 mm from the ECB caliper and 95 mm from the center of the caliper arm.

The finished assembly is shown in Figure 6.14.

### 6.3.7 Structural considerations and FEM-analysis

Several structural considerations were performed on the ECB-system prior to manufacturing.

#### Caliper arm and axle

It was especially important to consider the deformations that would pull the caliper out of true, relative to the rotor - that is, bending around the x-axis in Figure 6.4:

- Bending of the caliper axle: Because the force transducer was positioned next to the ECB-caliper, the active axle length was short compared to the axle diameter. It was therefore

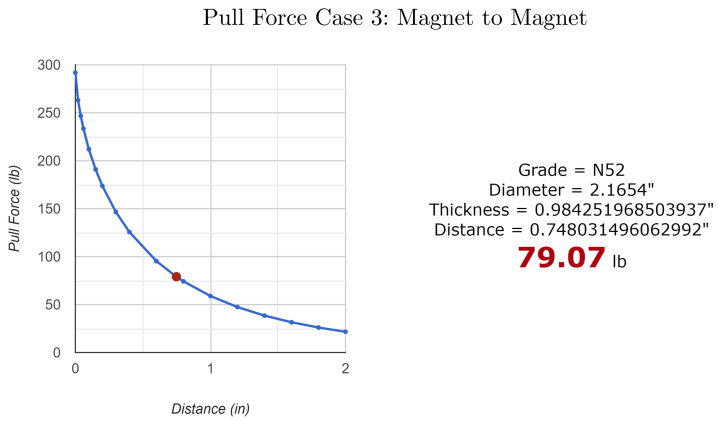


**Figure 6.16:** The attracting force from each magnet pair, calculated using the K&J magnet calculator [25]

.

considered insignificant.

- Bending of 12 mm gearhub axle and/or the caliper arm: The symmetry line described in the analytical model (Section 6.1) implied that the reaction moment in point $M_{x,\,A}$ in Figure 6.4 would be very small. Because of this, the deformations from the torque and bending moment acting on the caliper arm and 12 mm hub axle, respectively, would be insignificant.

### ECB caliper

In addition, any deformations that reduced the air gap between the ECB-caliper and braking rotor needed to be considered. The deformation of the magnet caliper bodies from the attracting magnet forces was therefore considered.

Naturally, the force between two attracting magnets decreases as the magnets are pulled apart. The attracting force between the magnet pairs was calculated from the K&J Magnetics calculator [25]. Using $55 \times 25$ mm N52 Neodym magnets and the previously defined air gap of 19 mm, this would create an attracting force of 79.07 lb = 35.9 kg $\approx$ 352 N as shown in Figure 6.16. This was likely an overestimate of the actual attracting force, as the chinese magnets probably were of lower grade neodymium than specified.

Using the above loading scenario, a FEM-analysis was carried out in Siemens NX12 on a single ECB caliper plate, with the following procedure:

1. The part file was first idealized in Solidworks by removing unneccesary holes, fillets and slots.
2. The part was then exported from Solidworks as a STEP AP203-file and imported into Siemens NX12 where a .fem file was created in the Pre/Post application
3. The polygon geometry was swept meshed with 3 mm CHEXA(8) elements, as shown in Figure 6.17(a)
4. The material properties of the .fem were assigned to 6082-T6 aluminum
5. RBE2 elements were created for the bolt holes and magnet slots, shown in orange in Figure 6.17(a)

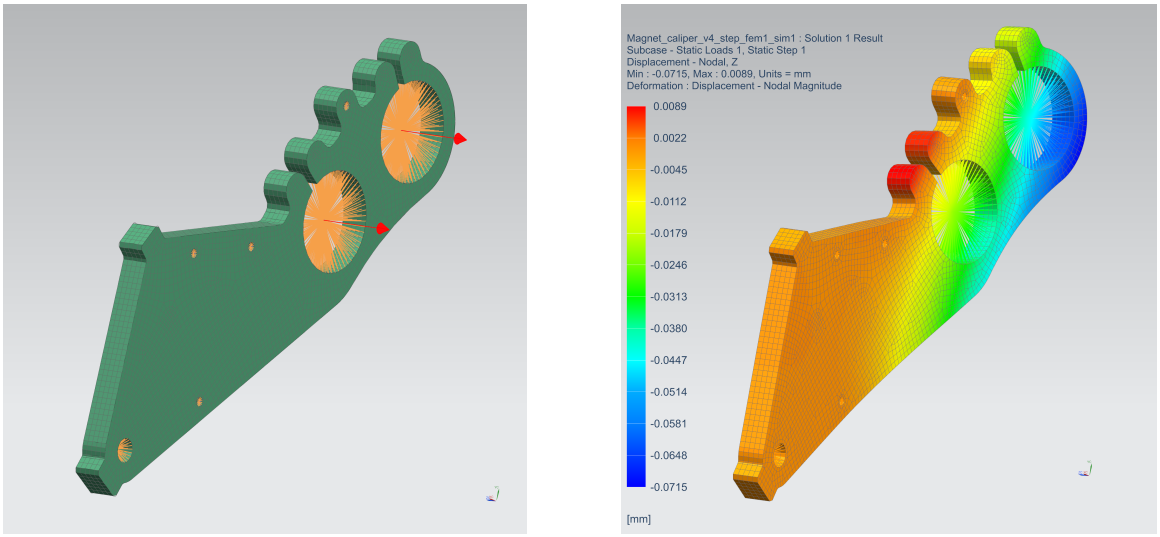


(a) The .sim file of the ECB-caliper plate

(b) Deformation in Z-direction

**Figure 6.17:** The FEM-analysis of the ECB-caliper plate. The simulation result has an absolute scale by 300.

6. A .sim file was created with an SOL101 Statics solver, and displacement and stress output requests
7. The RBE2 elements for the bolt holes and the caliper axle slot were constrained in all six degrees of freedom
8. An axial force of 353 N was applied in each of the RBE2-elements in the magnet slot for a total of 706 N, as shown in red in Figure 6.17(a)

The solution indicated a total displacement in the z-direction of 0.072 mm, as shown in Figure 6.17(b). The air gap would thus be reduced from 2.0 mm to 1.92 mm at the tip of the caliper, in other words an insignificant deformation. The calculated principal stresses were low around 10 MPa.

The presence of the magnets inside the ECB-caliper would likely add some stiffness to the system, but due to the slight conical shape of the slot (further detailed in Section 6.6) this was difficult to estimate. For this reason, the magnets were not included in the analysis, to depict a "worst-case" scenario.

#### Eigenfrequency analysis

The ECB showed stable performance during testing (Further detailed in Chapter 8) and an eigen-frequency analysis was not considered neccesary.

## 6.4 Friction brake conceptualization

A friction brake was also conceptualized, similarly based on the analytical considerations in Section 6.1. The friction brake would use the same connecting interface on the hub axle as the eddy-current brake, and consist of four main components:

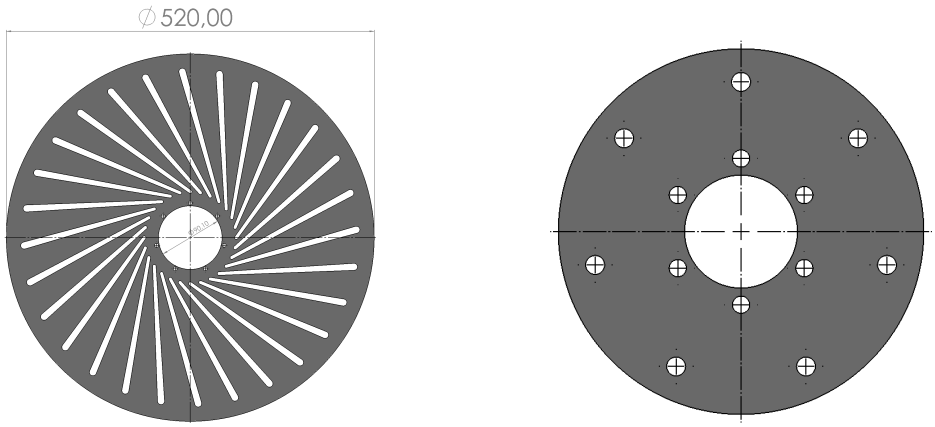


(a) 520 mm rotor.

(b) 7-bolt to IS-6-bolt adapter

**Figure 6.18:** Braking rotor and adapter for the friction brake

- The brake rotor, directly attached to the gearhub
- The brake caliper
- The caliper arm, enabling the caliper to pivot around the gearhub axle
- The caliper adapter bracket assembly, connecting the caliper to the caliper arm

The conceptualization of each component is briefly described next.

### 6.4.1 Brake caliper

The calculations in Section 5.5.1 indicated that a powerful bicycle disc brake with a four piston caliper would be adequate. Results from a dynomometer braking test done by Enduro Magazine [26] indicated that the Magura MT7 brake system had enough power for the intended application. The brake was tested with a 180 mm rotor and achieved an average braking torque of $\tau_{\text{brake}} = 99.3$ Nm with 40 N of lever pressure. This would equal a braking force on the rotor of around 1100 N, or a braking torque of $\tau_{\text{brake}} = 300$ Nm with a 550 mm braking disc. While this test was not very scientific, it indicated that the braking system's torque capabilities were satisfactory.

The geometry of the MT7 caliper created from approximate measurement of its physical dimensions to identify any spatial constraints or issues in the assembly.

The Magura MT7 uses mineral oil as braking fluid. The brake could be tested with its original lever to begin with, and afterwards coupled to a compatible master cylinder with a linear actuator. This would require a master cylinder with mineral oil compatible seals, like nitrile butadiene rubber (NBR).

### 6.4.2 Brake rotor

Using the aforementioned brake caliper, the rotor would need a thickness of $t = 2$ mm. The braking rotor was then designed with 28 evenly placed ventilation slots as shown in Figure 6.18(a), to maximize cooling but without removing much material. The braking surface was kept smooth, i.e. without holes or slots, as this could potentially lead to unwanted vibrations at low rpm.

Disc brake rotors for bicycles are normally laser cut from hardened AISI 410 Stainless steel with a hardness from 30-40 HRC [27]. The raw material is often blanchard grinded to achieve optimum flatness.

After consulting two independent braking component manufacturers, it was discovered that the blanchard grinding process might not be possible with rotor diameters above 300 mm. Consequently, a large diameter braking rotor might not feature optimum flatness. This could lead to instability during operation, but might be compensated for if the caliper was allowed to float sideways to some degree.

As Figure 6.18(a) illustrates, the braking rotor was designed to fit the Kindernay XIV 7-bolt interface. It could then be adapted to IS 6-bolt using an adaptor as shown in Figure 6.18(b). This would move the braking rotor inwards or outwards by a distance equal to the rotor thickness. It would therefore be important to have adjustability of the caliper in the z-direction.

### 6.4.3 Caliper adapters and brackets

The brake caliper was mounted in the reverse direction to position it as close to the force transducer as possible, and thereby minimizing the forces acting on the caliper arm and brackets.

The following requirements were also considered:

- To simplify wheel removal for the operator, the mounting system should allow quick adjustment of the caliper in the x-direction (Figure 6.2). The caliper could then be moved backwards before wheel removal, and forwards after installation. The operation should not require re-adjusting the caliper in any other directions
- When mounted, the caliper should be rigid in the $x - y$ plane, but allowed some movement in the z-direction (Figure 6.4(b)) to account for lateral movement of the braking disc.

By designing a flexible bracket from a steel plate, one could satisfy both of these requirements. The "flex plate" would attach to the caliper adapter and be positioned directly behind the braking disc – therefore not taking up any significant bending moments. To allow movement in the x-direction, slots were added were the flex plate attached to the caliper arm brackets. Lastly, the flex plate was designed to attach to the over- and underside of the caliper arm.

This required two equal brackets mounted on the over- and underside of the caliper arm, as shown in Figure 6.19. Using a common location of the upper and lower bolt holes, the brackets were attached with two M8 bolts. The brackets were designed with a 25 mm wide slot to allow movement of the whole caliper assembly in the z-direction. With a common thickness of 5 mm, the brackets could be made from 5 mm steel plate or rectangular bar.

### 6.4.4 Caliper arm

The caliper arm for the friction brake would function similarly to the eddy-current brake, by pivoting around the gearhub and directing the forces into the force transducer.

The arm required an L-shaped form because of the caliper brackets. As previously discussed, it also had to provide adjustment of the caliper in the x- and z-direction, and the force transducer location in the z-direction. It was therefore desirable to manufacture the arm with a geometry that had a decent amount of surface area, high strength and decent weight.

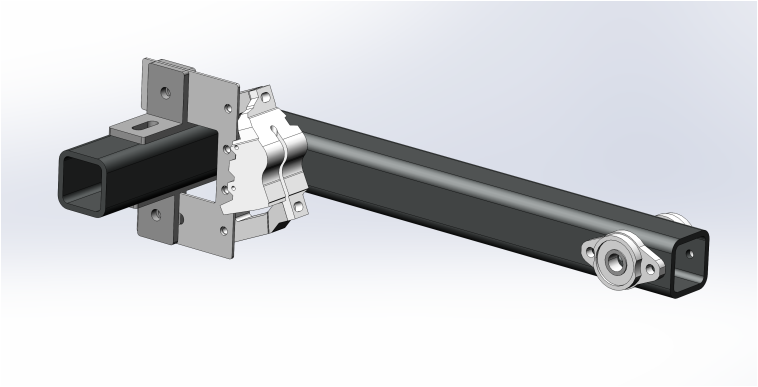

**Figure 6.19:** Brackets attaching the brake caliper to the braking arm.

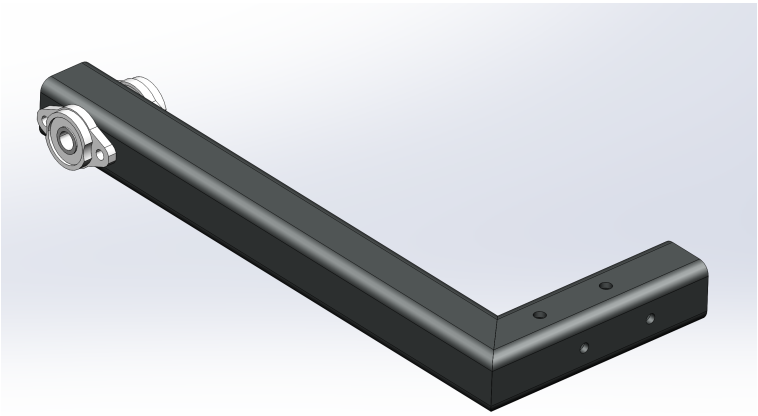

**Figure 6.20:** The caliper arm made from square steel tubing.

A 40×40×4 mm S355 structural square tubing section was chosen, as it had sufficient thickness for tapping, was readily available and easily weldable.

The caliper arm was designed with UFL 001 flange bearings to pivot around the gearhub axle, similar to the eddy-current brake.

### 6.4.5 Force transducers

The friction brake was designed with a tension/compression force transducer, similar to the eddy-current brake. Because the sensor placement was similar to the friction brake, a sensor with similar geometry and resolution could be used for both braking systems. The outgoing force transducer would attach to the braking arm on one side and to the testing rig on the other, using the brackets designed previously.

### 6.4.6 Final dimensioning

Similar to the ECB conceptualization, the process of defining the final dimensions was completed in SolidWorks after drafting all components and combining them in the testing rig assembly. This

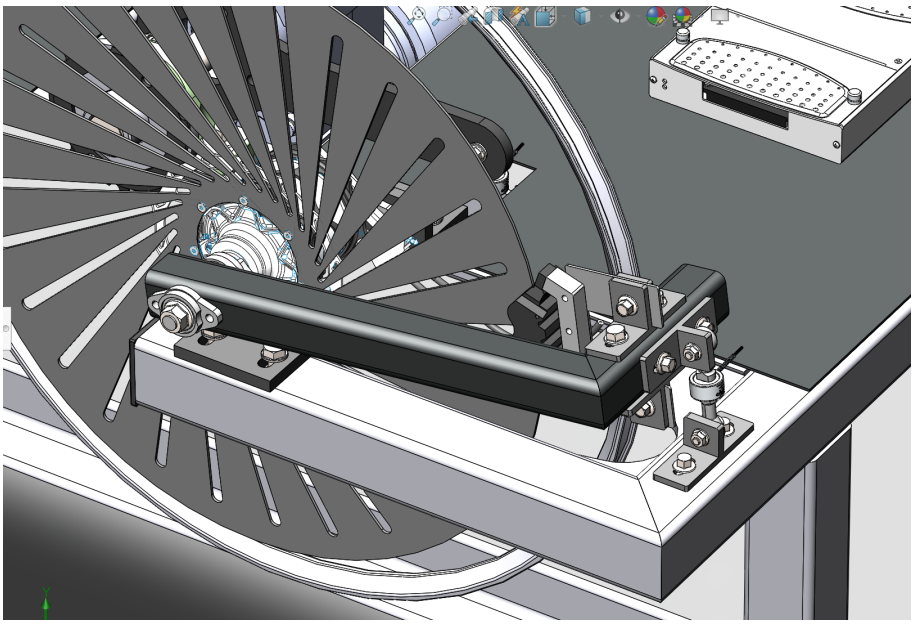

**Figure 6.21:** The complete friction brake assembly with force transducer and bracket.

resulted in the following measurements:

- The braking disc diameter was adjusted to $d = 520$ mm. This meant a slight decrease in braking power compared to the above calculations, but still well within the torque requirements.
- The length of the caliper arm was adjusted to $L_2 = 381$ mm . This gave enough clearance for removing a 29" inch wheel, while keeping the force transducer as close to the caliper as possible.

The finished assembly is shown in Figure 6.21.

### 6.4.7 FEM-analysis

An FEM-analysis was performed on the braking arm to check the deformations and stress under maximum braking torque. The individual part files for the braking arm assembly, including brackets and adapters, were exported as STEP AP203 from Solidworks and imported into Siemens NX12. A .fem file for each part was created with an accompanying idealized part file, to remove unnecessary features that were considered irrelevant for the analysis. The parts were then meshed individually and the correct material was applied. The parts were idealized and meshed in the following way

- **Caliper arm:** The bolt holes for the flange bearings and brackets were removed in the idealized part. It was then converted to a midsurface geometry and the part was meshed in the accompanying .fem file with 2.5 mm CQUAD4 elements, as shown in Figure 6.22. RBE2 elements were added to the holes centered around the axle.
- **Loadcell bracket:** The bolt holes and edge blends were removed in the idealized part and the geometry was swept meshed with 2.5 mm CHEXA(8) in the .fem file. An RBE2 element was added to simulate the constraint from the force transducer.
- **Flexplate brackets:** The bolt holes and edge blends were removed in the idealized part and the geometry was swept meshed with 2.5 mm CHEXA(8) in the .fem file

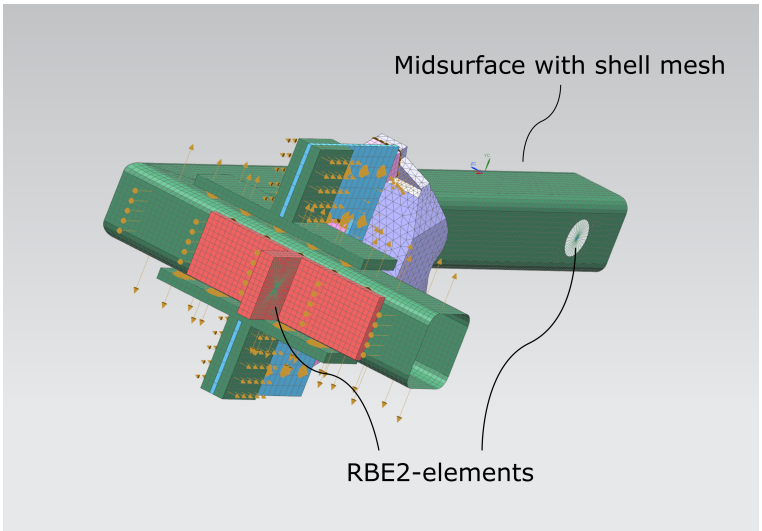


**Figure 6.22:** The finished simulation file with meshes and contacts.

- **Caliper flex plate:** The bolt holes and edge blends were removed in the idealized part and the geometry was swept meshed with 5 mm CHEXA(8) in the .fem file
- **Caliper reverse adapter:** The bolt holes and edge blends were removed in the idealized part and the geometry was swept meshed with 2.5 mm CHEXA(8) in the .fem file
- **Caliper:** The part was idealized by removing bolt holes, edge blends and complicated edges. The part was 3D meshed with 4 mm CTETRA(10) elements and assigned an aluminum 6061 material. A common RBE2 element was positioned inside the caliper, connecting both of the faces shown in Figure 6.22. The element was added in the approximate location of the effective radius $r_{\text{eff}}$ on the the brake rotor.

The individual .fem files were then combined into an assembly .fem (assyfem) file.

### Statics analysis

A simulation file based on the assyfem file was then created with an SOL101 Linear Statics solver. This is primarily a linear NX-nastran solver, but it can include non-linear effects due to contacts and was therefore well suited for the analysis. The brackets were glued to the caliper arm. Similarly, the flex plate and caliper adapter were glued to represent the bolted connections in the final assembly. The assembly could have been modelled with bolted connections, but the acting forces were low compared to the bolt sizes this was considered unnecessary (low grade M8 bolts normally have a proof load of over 2000 kg).

The RBE2 elements in the rotating end of the caliper arm were constrained in the first 5 dimensions, hence allowed to rotate around the z-axis. The RBE2 element on the force transducer bracket was constrained in a similar manner. A force was then applied to the RBE2 element inside the caliper, acting along a vector tangential to the braking rotor.

The finished simulation file with meshes and contacts is shown in Figure 6.22.

#### Real eigenvalue analysis

Due to oscillations observed during the initial testing (shown in Figure 8.1), a real eigenvalue analysis was also performed with the SOL103 Real Eigenvalues solver. A real eigenvalues calculates the eigenfrequencies (or resonance frequencies ) for a given structure without constraints. The analysis was set up with 12 modes, the six first being (trivial) free body modes. The result would therefore indicate the first six eigenfrequencies of the structure.

#### Results

The results from the static analysis are shown in Appendix C.1 and show maximum deflection values around 0.2 mm for the caliper in the loading direction. Furthermore, the caliper shows very little deformation in the z-direction and little twisting. This is likely a result of the flex plate placement being in line with the disc. The maximum principal stresses indicate maximum stresses around 120 MPa in the flex plate bracket, although this is likely somewhat artificial because of stress concentrations in sharp corners.

The results from the eigenvalue analysis are shown in Appendix C.2. The modes were identified as:

- **Mode 1:** 95 Hz
- **Mode 2:** 636 Hz
- **Mode 3:** 707 Hz
- **Mode 4:** 751 Hz
- **Mode 5:** 1046 Hz
- **Mode 6:** 1440 Hz

The modes were primarily related to the flex plate bracket, which is not surprising considering its low relative stiffness.

## 6.5 Additional components and modifications

### 6.5.1 In-going force transducer

As determined in Section 5.6, it would also be highly beneficial to use an axial force transducer on the in-going measurement. The problem with the current rig however, was the lack of a supporting element around the torque arm from the motor. The plate on top of the testing rig was only 2 mm and would be too flexible for this purpose. It was therefore decided to install a supporting S355 60×60×5 mm L-profile in the testing rig frame with a bolted connection, as shown in Figure 6.23(a). By cutting a slot in the top plate, the force transducer could be installed as shown in Figure 6.23(b). The profile was designed to be adjustable so that various force transducer geometries could be adopted.

Considering the maximum motor output at 400 W and 30 rpm, the in-going force transducer would see a maximum force off

$$F_{\text{fs, in}} = \frac{\tau_{\text{motor, max}}}{L_{\text{arm, in}}} = \frac{127 \text{ Nm}}{0.25 \text{ m}} \approx 509 \text{ N} \tag{6.9}$$

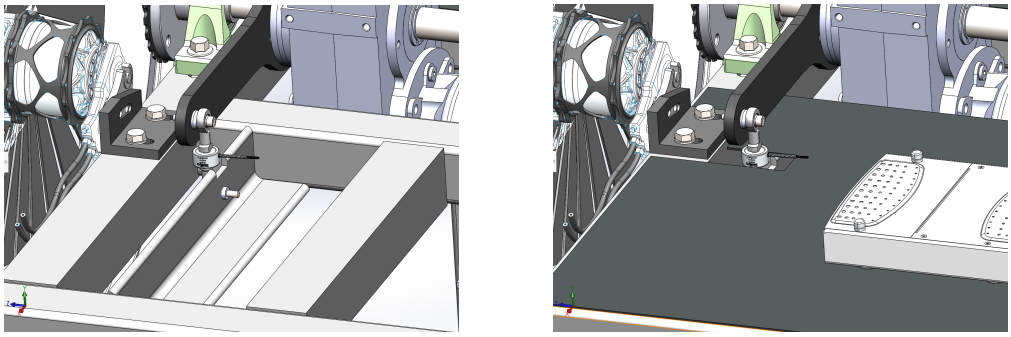

(a) Without top plate

(b) With top plate

**Figure 6.23:** Addition of L-profile to support in-going force transducer, shown with and without top plate.

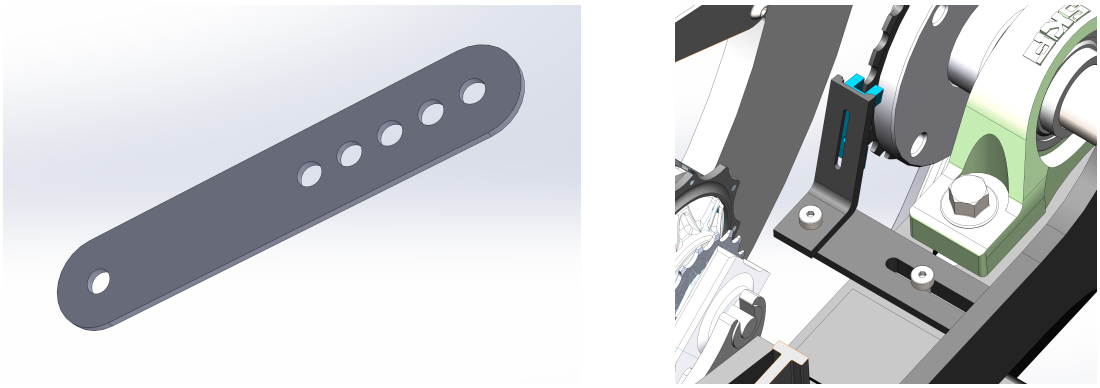

(a) The "dummy" force transducer bracket.

(b) The speed sensor bracket

**Figure 6.24:** Brackets for the testing rig.

where $L_{\text{arm, in}}$ denotes the effective length of the torque arm mounted to the motor. The minimum braking torque $\tau_{\text{motor, min}} = 8$ Nm would produce a force of $F_{\text{fs, in}} = 31.8$ N. Thus, a similar force transducer could be used for the in-going measurement.

A set of "dummy" force transducers were also designed, shown in Figure 6.24(a). These brackets could be temporary placeholders to verify basic functionality of the testing rig, before purchasing costly force transducers.

### 6.5.2 Mounting bracket for speed sensor

The IR-speed sensor for the control system (detailed in Section 7.1.2) was to be mounted around the teeth of the 32T chainring from the motor gearbox. The bracket needed to support the following requirements:

- Clearance for the chain surrounding the 32T sprocket
- Adjustability in the x-direction to account for various motor positions when adjusting chain tension
- Adjustability in the z-direction to account for different chainlines when testing various gear-

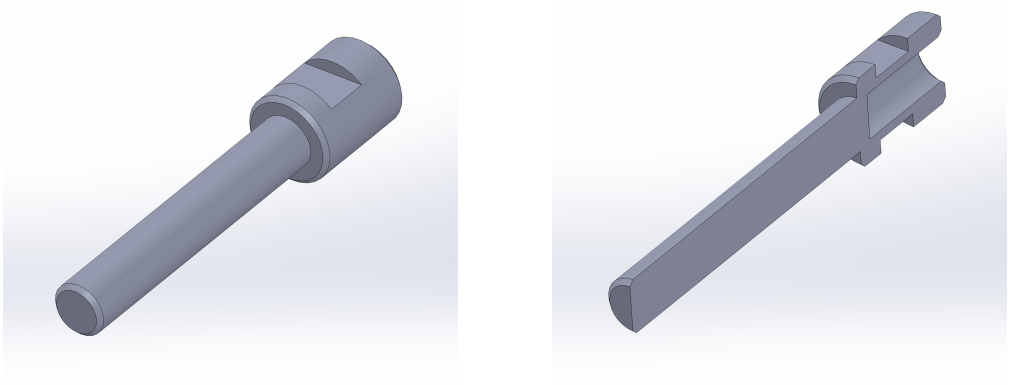

(a) Shown as solid

(b) Shown with cutaway

**Figure 6.25:** The 10×135 mm adapter.

hubs

The resulting bracket geometry was designed and mounted to the testing rig frame as shown in Figure 6.24(b). The bracket was 3D-printed with PLA-filament.

### 6.5.3 Adapter for 10×135 mm gearhubs

To use the caliper arm with 10×135 mm gearhubs an adapter was needed. The adapter would simply act as a "locknut" for the non-drive side that extended into a 12 mm axle. Such an adapter is shown in Figure 6.25, with a simple slot for a 14 mm spanner wrench. The inner hole would have a 10×1 mm thread. The 12 mm axle could have threads on the end or simply a slot for an external snap ring.

A similar variant could also be made for 5×135 mm gearhubs. The hole for the hub axle would then be 5 mm instead of 10 mm, and the adapter could be combined with a quick release.

## 6.6 Manufacturing and assembly

The conceptualization phase also involved having a clear-cut plan for manufacturing the components for both brake systems. The company had some basic metalworking capabilities, including a metal lathe, an hydraulic feed metal band saw, welding machines (TIG and MIG) and a drill press. The company also had access to an external workshop with a water-jet cutter and a CNC-mill. The following paragraphs give a brief overview of the manufacturing processes.

### 6.6.1 Eddy-current brake

The manufacturing and assembly of the friction brake is described next.

#### Brake rotor components

The outer brake rotor was cut on the WJS water cutter from 15 mm 6082-T6 sheet, with 5 mm holes. The holes were then tapped to fit M6 bolts. The brake rotor spiders were water-cut from 2 mm AISI 302 stainless sheet from company material supply.

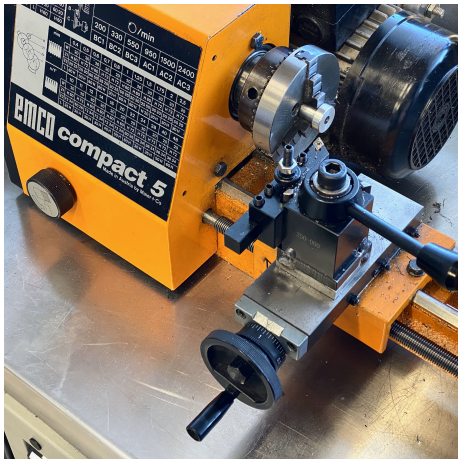


(a) Turning aluminum spacer for force transducer

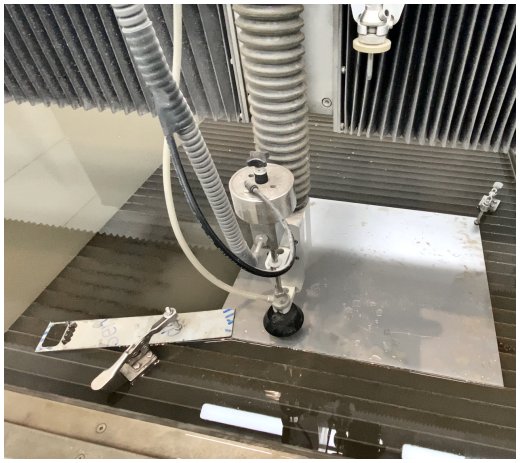

(b) Water-cutting rotor-spider

**Figure 6.26:** Manufacturing parts for the ECB using various machinery

### Magnet caliper

The magnet caliper bodies were water cut from the same 15 mm 6082-T6 sheet as the outer braking rotor. As mentioned in Section 6.3.2, the magnets were to be positioned in attracting formation for maximum braking performance. This would result in severe magnetic forces between the magnets, potentially making installation of the secondary magnet difficult and dangerous. The caliper bodies were therefore cut with a slight cone for the 55 mm holes. This was achieved by optimizing the cutting speed parameters in the water cutting software (IGEMS 2020).

The mounting holes for the barrel-nuts were post-drilled on the drill press, and the split for the M4-bolt was added manually with custom angle-grinder fixture and a Dremel. The barrel nuts were custom made by the author on the lathe with a 8×15 mm dimension.

To ensure optimum alignment with the caliper axle, the axle mounting holes were dimensioned and cut with a 13 mm closed hole, as shown in Figure 6.12. Both caliper bodies were then clamped together, and the Ø15 holes were machined in the same operation on a DMG Mori CNC mill with an H7 tolerance. The clamping split was then opened on a band saw. Lastly, a 5 mm hole with threads in one end was drilled and tapped in the ears of the split.

### Caliper arm

The caliper arm was cut to length from the S355 square tubing on the band saw. The mounting holes for the flange bearings were added with a drill press. The 12 mm and 15 mm axles for the gearhub and caliper mounting points were turned from tool steel bar on the Emco Compact 5 lathe, by the author. The aluminum bearing spacer for the 12 mm axle was turned from 6082 aluminum on the same lathe.

## 6.6.2 Friction brake

The manufacturing and assembly of the friction brake is described next.

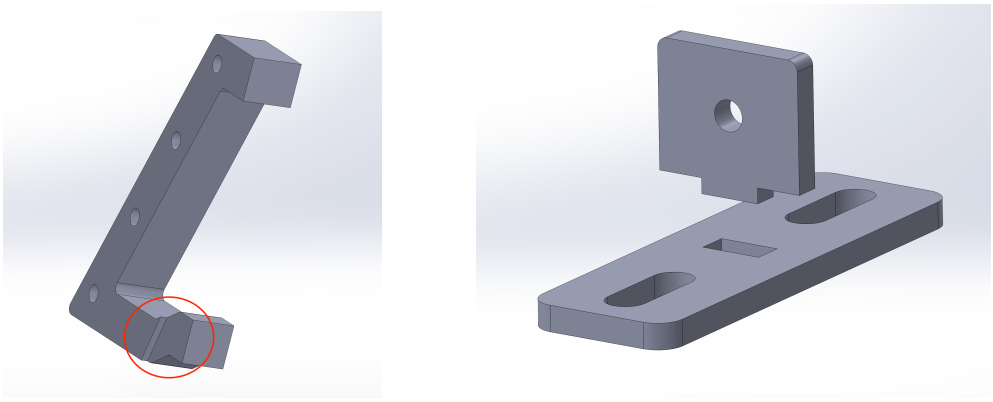

(a) Slot in reverse adapter

(b) Slot for easier welding

**Figure 6.27:** Manufacturing features.

### Braking disc

The braking disc model was exported to a flat pattern (.dxf) file and laser-cut by an external supplier (DELTA Braking) from 2 mm 4028 Stainless (hot rolled, annealed) with a hardness of 20HRC. Due to equipment limitations caused by the large rotor diameter, the rotor was not hardened or blacnhard grinded.

### Caliper reverse adapter

The caliper reverse adapter was also exported to a flat pattern file and cut from 15 mm 6082 aluminum on the WJS water-jet cutter. The holes for the caliper were tapped afterwards and the slot for braking rotor clearance shown in Figure 6.27(a) (not dimension critical) was added manually with a die grinder.

### Caliper flex plate

The caliper flex plate was similarly exported and cut on the WJS water cutter from 2 mm AISI 302 Stainless sheet from the company material supply. The plate would ideally be made from a spring steel with higher yield strength, but this was not available at the time.

### Flexplate and force transducer brackets

The flexplate and force transducer brackets were similar in dimensions, but originally modelled as one solid. They were instead divided into two solids that were cut on the WJS water jet from 5 mm S355 plate and TIG-welded by the author afterwards. A 3 mm deep slot was designed into each part to ease the welding process, as shown in Figure 6.27(b).

### Caliper arm

The S355 40×40×4 mm square profile was cut on the band saw in two pieces, each with one 45 degree end for the miter joint. The length measurement was not a critical dimension. The required holes were then drilled in the drill press. The miter joint was TIG-welded by the author in two stages; first tack welded with a slight positive angle, and then fillet welded inwards to obtain a perfect 90 degree angle.

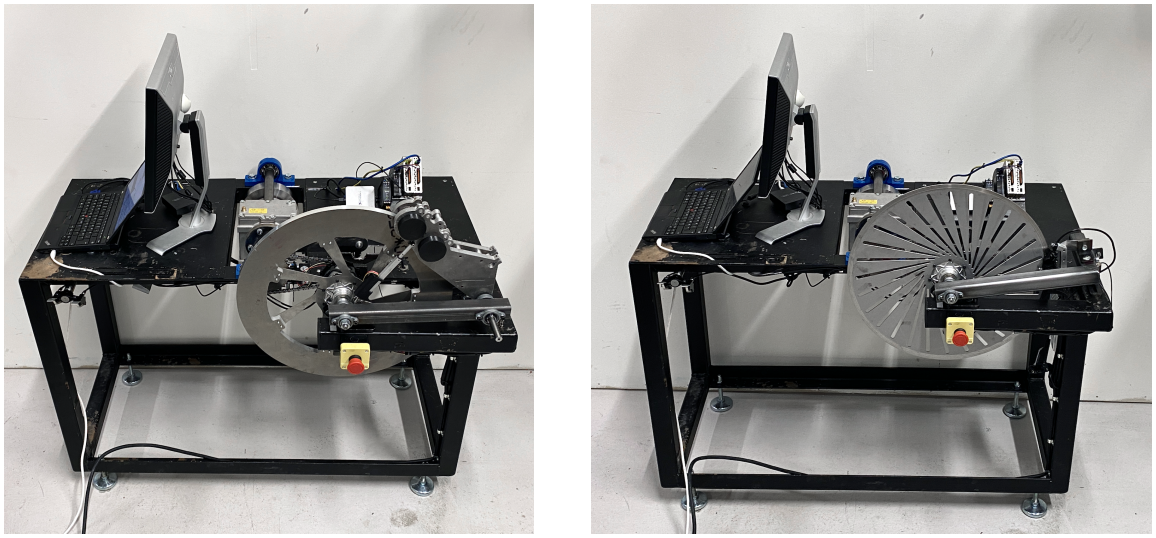

(a) ECB

(b) Friction brake

**Figure 6.28:** The finished braking systems after manufacturing.

#### Drawings

Drawings were made for the parts:

- 10×135 mm adapter: Drawing with dimensions
- Motor flywheel: Drawing with tight geometric tolerances was made to ensure concentricity
- ECB caliper arm: Drawing with hole locations and a cut list with lengths
- 520 mm brake rotor for friction brake: A drawing was made to complement the .dxf (flat pattern) file, adding flatness, surface and geometric tolerances. This was necessary when contacting external suppliers for quotes
- Friction brake welded caliper arm: Drawing with hole locations, welds and a cut list with lengths and angles

The drawings are shown in Appendix F. As the remaining parts were water-cut and had no critical dimensions, they could simply be exported as .dxf (flat pattern) files from SolidWorks and imported into IGEMS on the water-jet computer.

### 6.6.3 Finished assemblies

The finished brake systems are shown in Figure 6.28. Additional pictures of both systems are shown in Appendix B.

## 6.7 Setup and calibration

### 6.7.1 Calibration rig for force transducers

A simple calibration rig was designed to facilitate quick and accurate calibration of the tension/compression force transducers. The two force transducers used to measure input and output

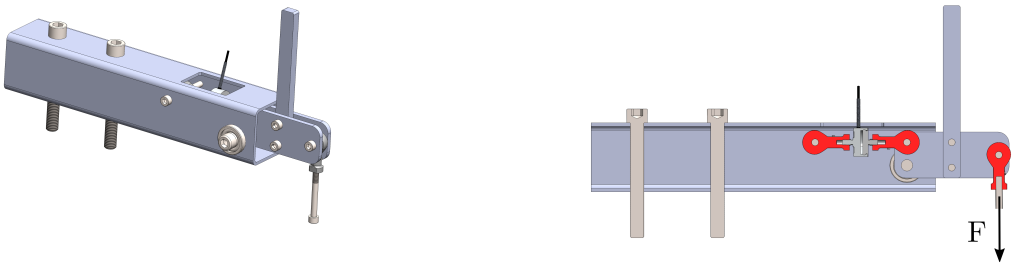


(a) (b)

**Figure 6.29:** The force transducer calibration rig, with the force applied in (b).

power would see opposite loading conditions, meaning that the motor force transducer would measure compressive force while the brake force transducer would measure tensile force. The calibration rig was therefore designed to function in two orientations, to be able to calibrate force transducers in tension and compression. The rig was designed as a compact device that could be clamped to the corner of a workbench.

The main body was constructed from 60×60×3 mm square tubing with two 6800 ball bearings in one end. A pivoting swing link was coupled to the ball bearings, and extending outwards from the main body. The force transducer was connected via female rod ends to the square profile in one end, and the swing link in the other end. A known weight was then hung from the opposite end of swing link, also connected to a rod end bearing. The swing link was designed with a rectangular shape as shown in Figure 6.29(b), such that the moment arm for the weight was four times the arm for the force transducer, that is, $L_{\text{weight}} = 4L_{\text{ft}}$ . The swing link would therefore multiply the added weight four times, meaning that 1000 N capacity force transducers could be calibrated with an approximately 25 kg hanging weight.

The complete calibration rig assembly is shown in Figure 6.29(a).

### 6.7.2 Alignment tool for force transducer installation

An alignment was also created for accurate installation of the force transducers. The tool was designed to work with both the motor and brake force transducer, and for alignemen in the x-y and y-z plane. The model was 3D-printed on an Ultimaker 3 printer with PLA-filament and 100% infill.

The tool essentially provided two supportive edges for accurately aligning the measuring direction of force transducer, by using an anglemeter or a level as shown in Figure 6.30.

### 6.7.3 Setup and calibration procedure for testing rig

The setup and calibration procedure for the testing rig involved multiple steps to ensure optimal performance and accurate measurements:

1. Install gearhub with brake rotor
2. Align and tighten the chain by adjusting the x-position of the motor assembly
3. Install the 12 mm gearhub axle

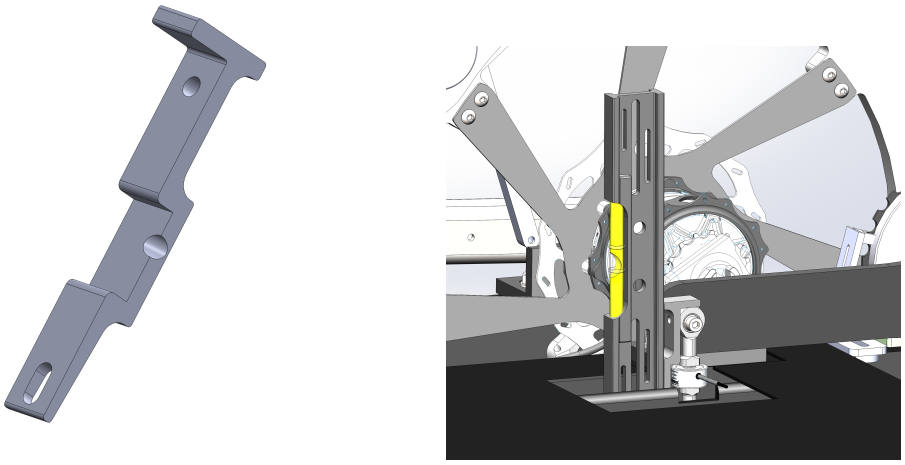

(a) The force transducer alignment tool

(b) Using the alignment tool during installation

**Figure 6.30:** A force transducer alignment tool was constructed to accurate installation.

4. Install the ECB-assembly and connect actuator to control board. Use spacers on the 12 mm axle to space the caliper correctly vs. the braking rotor.
5. Tighten the locknut on the hub axle to 12 Nm using a torque wrench (to ensure realistic and even preload on the hubs)
6. Align the brake caliper position relative to the braking rotor position such that the faces are parallel, by using the built in adjustment in the UFL001 bearings.
7. Align the brake loadcell in the x-y and y-z plane by using the alignment tool shown in Figure 6.30.
8. Align the motor loadcell in a similar manner

Point 2 and 6-8 would only have to be performed once. If changing the sprocket size of the gearhub (and thereby altering the necessary chain length) the chain tension would need readjustment. In that case, point 2 and 8 would need to be repeated.

### 6.7.4 Gearhub replacement procedure

When in use for development, the testing rig would test different gearhubs on a regular basis. For this reason, the ECB system was designed to allow quick gearhub replacement without altering any of the above settings. The removal and installation procedure of a gearhub in the ECB system consisted of the following steps:

1. Extend the actuator to 100%, switch off the power for the LAC-board and disconnect the P16 Actuator
2. Disconnect the force transducer from the caliper axle by removing the locknut with an 8 mm spanner wrench
3. Remove the locknut on the gearhub axle with a 19 mm socket

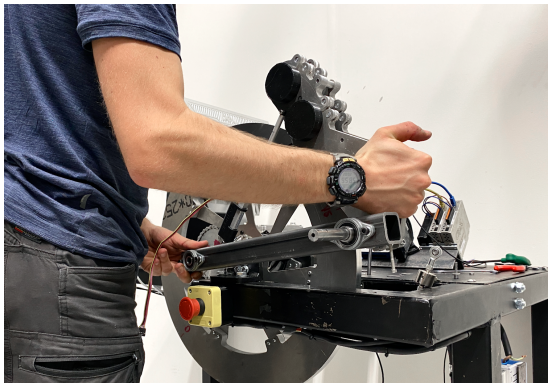

**Figure 6.31:** Removing and installing the ECB assembly.

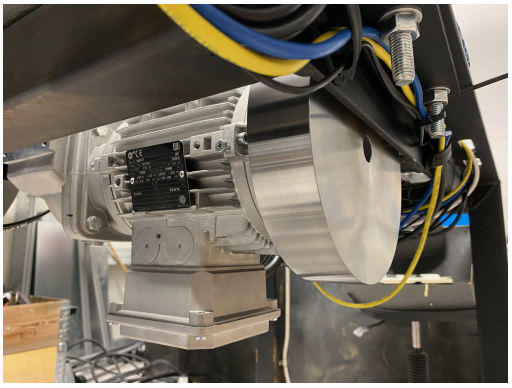

**Figure 6.32:** The 9 kg steel flywheel installed on the motor.

4. Remove the ECB assembly, axle spacers, gearhub axle and gearhub
5. Install the gearhub, gearhub axle, axle spacers and the ECB system
6. Install and torque the hub axle locknut to 12 Nm
7. Connect the force transducer to the caliper axle and torque the locknut to 10 Nm
8. Connect the P16 actuator and power the LAC-board.

Removal of the ECB system is shown in Figure 6.31.

## 6.8 ECB stability improvements after initial testing

The ECB was tested in several stages with a fixed rear hub (1:1 gearing) to examine and improve the stability of the system under load. The results from the the initial testing at 215 W and 60 rpm rotor speed, shown in Figure 8.2, indicated that the ECB oscillated around two frequencies:

1. $\sim$ 1 Hz: This frequency matched the rotational speed of the ECB rotor, but also the 16T input sprocket.
2. $\sim$ 16 Hz: This frequency matched the number of teeth per second on 16T input sprocket and the 32T gearbox sprocket

As the 16 Hz frequency matched the sprocket tooth frequency, it was likely caused by the chain polygon effect [17], as discussed in Section 5.3.1. This effect would be impossible to eliminate without discarding the chain transmission, but it could to be compensated for by running efficiency measurements over time with running mean calculations. The oscillations shown in Figure 8.2 were roughly 15% and seemed high to be caused by the polygon effect alone. Additional measures were therefore taken to reduce the oscillations:

1. The alternating current from the inverter to the motor was measured using the ACS 712 passive current sensor to check for correlation vs. the observed oscillations
2. The frequency inverter was adjusted to operate from a V/f characteristic curve instead of Voltage Flux Control (VFC) mode. This would prevent the inverter to adjust for the changing speed from the polygon effect

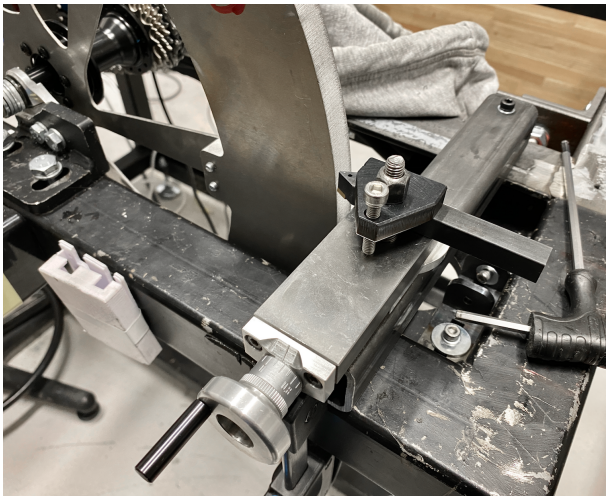

(a) The lathe tool holder mounted to the testing rig

(b) The end result after turning

**Figure 6.33:** Turning the ECB rotor to minimize the 1 Hz oscillation.

3. The 3-phase motor fan was removed and replaced with a 9 kg steel flywheel that was precision machined by an external machine shop (Aasen Dreieverksted) and installed on rotor axle as shown in Figure 6.32. It was installed with a glued connection, by first removing the motor completely and then leveling it with the axle in a vertical position. The flywheel would introduce a significant inertia in the system that could help smooth out the oscillations

The current measurement, shown in Figure 8.3, did not indicate any correlation between the motor current and observed oscillations. Likewise, adjusting the inverter settings to V/f characteristic curve did not produce a visible difference in the results. The result from the flywheel installation, shown in Figure 8.4 slightly reduced the 1 Hz frequency, but in return amplified the 16 Hz frequency considerably. It was therefore not included in the continued testing.

The first frequency of 1 Hz was believed to be caused by the ECB rotor. Measuring the rotor with a dial indicator showed a radial run-out of about 0.2 mm. A custom fixture was created to mount lathe tooling directly in the testing rig, as shown in Figure 6.33(a). The rotor was then turned directly in the testing rig, while mounted to the hub. Figure 6.33(b) shows a clear improvement from this modification, to the point where the 1 Hz frequency was close to eliminated.

# Chapter 7

# Data aquisition and control system implementation

The control system and data acquisition hardware was implemented in several stages to verify the performance of each subsystem. The first step was to define the basic requirements for the data aquisition and control system. Based on this, a general hardware layout for the control system and data flow would be defined. The appropriate hardware was then selected, purchased and installed. Finally, the software complementing the chosen hardware was programmed to meet the requirement needs.

## 7.1 Hardware setup

Because of the general uncertainty around the testing rig sub-systems, the initial performance and stability analyses of the braking system were done with low-cost measuring equipment:

- DYMH-003 1kN tension compression force transducers
- SMOWO RW-ST01A force transducer amplifier
- Arduino Uno microcontroller

The above force transducer and amplifier combination was calibrated with the calibration rig described in Section 6.7.1.

After verifying the brake performance and stability with the aforementioned equipment, the testing rig was fitted with high-accuracy measuring equipment. The finished control system consisted of the following hardware:

- PC with Windows 10 x64 and LabView 2019 64-bit
- TP-Link TL-SG105E Network Switch
- National Instruments USB-6002 Multifunction Data Aquisition Device (DAQ) (shown in Figure 7.2(c)
- Actuonix LAC Control Board
- Actuonix P16 Linear Actuator

- Two HBM ClipX 1-BM40 Loadcell Amplifiers (shown in Figure 7.2(b))
- Two HBM U9C 1 kN 4-wire, full-bridge loadcells (0.2% accuracy)
- LM393 Comparator IR Speed Sensor Module (FC-03)
- NORD SK500e frequency inverter
- PULS MiniLine 12 V and 24 V power supplies

The control system hardware configuration is shown in Figure 7.1. Data-sheets for the above devices are given in Appendix E. A short description of the functionality for each subsystem is given next.

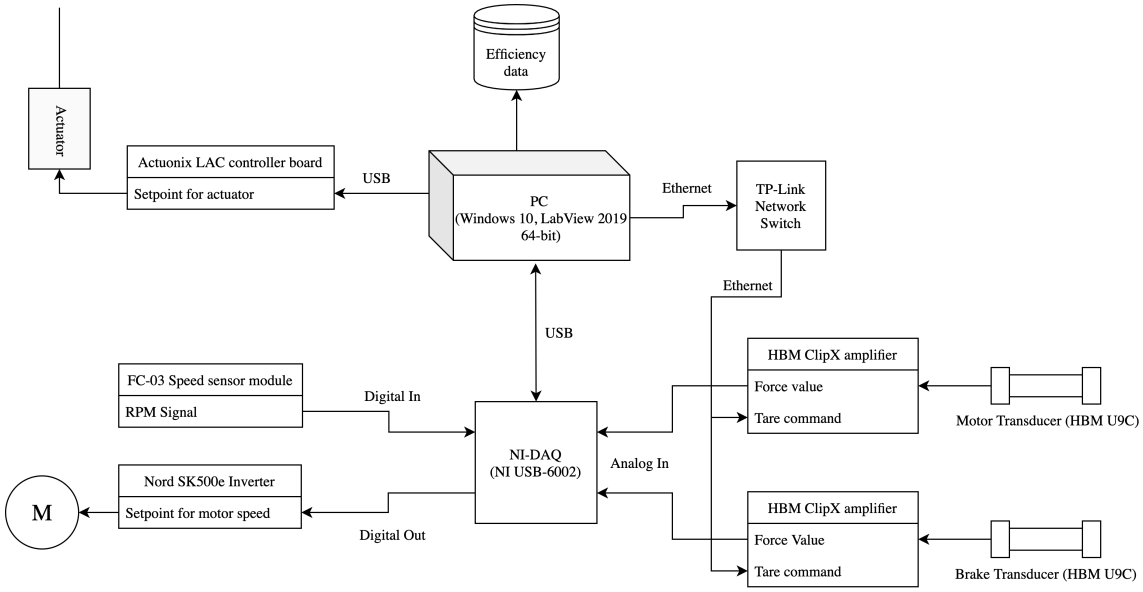


**Figure 7.1:** Hardware diagram illustrating the control system hardware setup

### 7.1.1 Force measurement

The HBM U9C force transducers have a measurement sensitivity of 1 mV / 1000 N. A transducer amplifier was therefore necessary to scale the voltage delta and thereby increasing the measurement sensitivity and stability for the NI-DAQ. The force transducers were each connected to a separate HBM ClipX amplifier and parametarized with the the data from their respective calibration certificates. The measurement values were then verified in the calibration rig from Section 6.7.1.

The ClipX amplifier analog output was set to $\pm 10V$ (the maximum measuring range for the NI-DAQ) for a measurement span from 0 to 1000 N and a sample rate of 19.2 kHz. The amplifiers were connected to the NI-DAQ using short-length double shielded cables to minimize noise interference.

The ClipX amplifiers were also connected directly to the PC via Ethernet. This enabled direct parametarization of the devices from LabView, further detailed in Section 7.2. Due to long delivery estimates for the measuring equipment, the order was placed early in the project phase. The transducers were ordered with the necessary maximum capacity to enable testing of both braking systems at the maximum torque requirements.


(a) The FC03 Speed sensor

(b) HBM U9C force transducer and ClipX amplifier

(c) The NI-DAQ USB 6002

**Figure 7.2:** The measurement hardware for the control system.

### 7.1.2 Speed measurement

The FC-03 speed sensor, shown in Figure 7.2(a), works by outputting a *HIGH* digital signal if the IR-beam is blocked. The sensor was installed parallel to the 32-tooth sprocket from the motor gearbox, thus giving a resolution of 32 points per revolution. The digital signal was outputted directly to the NI-DAQ.

### 7.1.3 Motor control

The NORD SK500e inveter has numerous options for control via analog and digital signal. For maximum stability, the motor speed was pre-set on the inverter control panel. The inverter was then activated via a digital signal from the NI-DAQ, controlled from LabView.

### 7.1.4 Brake actuation

The Actuonix P16 linear actuator has position feedback, and can be accurately controlled via the Actuonix LAC control board. The control board was connected to the PC via USB for direct control.

### 7.1.5 Power supply

The hardware components were powered in the following way:

- NI-DAQ: USB 5V DC power
- TP-Link switch: Separate 5 V DC PSU
- ClipX Amplifiers: 24 V DC from Puls MiniLine PSU. The amplifiers were grounded according to manufacturer instructions.
- Actuonix LAC: 12 V DC from Puls MiniLine PSU.

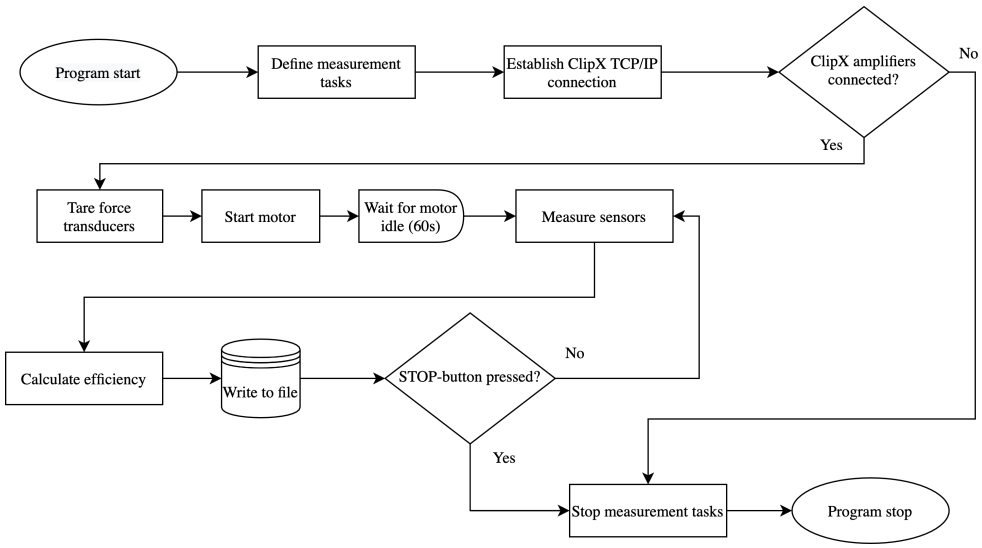


**Figure 7.3:** A flowchart for the control system LabView program

## 7.2 Software design

As the control system was centered around the NI-DAQ, the software was written in LabView 2019. The NI-DAQ is a versitaile device with analog and digital I/O, as well as built in timing.

The software was written step-by-step, and each of the program sub-tasks were implemented and tested as single virtual instruments (VI's). The single VI's were then combined in a common LabView Project.

The software design for each sub-task is described next. The complete LabView-code is shown in Figure D.1 in Appendix D.

### 7.2.1 Program flow

The basic program structure consists of a timed sequence, followed by while-loop inside a case structure. The case-structure is true only if the ClipX amplifiers are connected, hence, the program will abort if no connection is detected.

Once the program detects a successful connection to the ClipX-amplifiers, the timed sequence initiates and tare the force transducers in order, before starting the motor. A wait command is then run to delay the measurement tasks until the motor reaches the desired rotational speed.

The while-loop performs the measurement and calculation tasks and iterates until the program is stopped. The program flow is illustrated in Figure 7.3.

### 7.2.2 Defining measurement channels

As shown in Figure 7.4, the program starts by defining the following measurement channels:

- Force transducers: $\pm 10$ V differential input, one channel for each transducer
- Speed sensor: $0 - 5$ V differential inputs

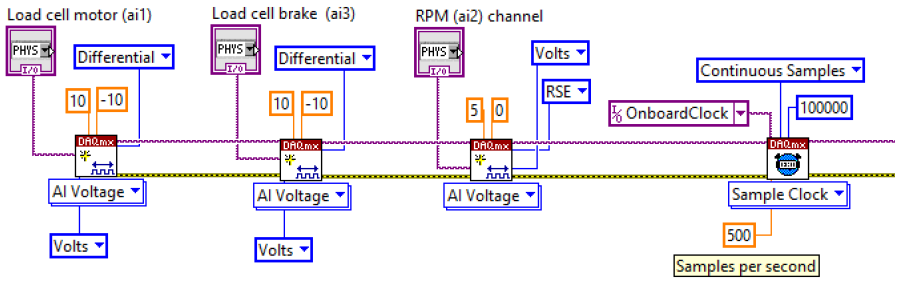


**Figure 7.4:** Defining the NI-DAQ inputs in LabView

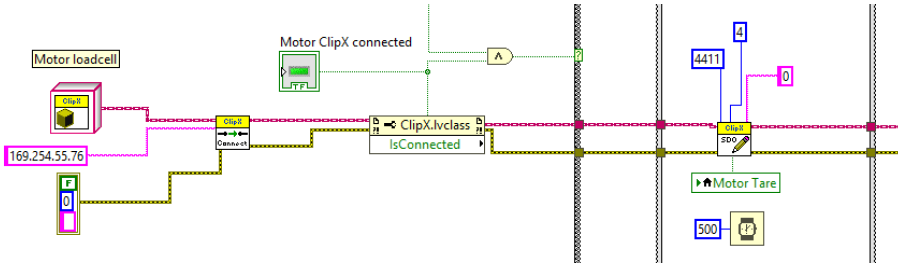


**Figure 7.5:** Connecting to ClipX and taring the force transducers

A sample clock with 500 samples/second and continuous operation is then defined for the measurement tasks.

### 7.2.3 Force measurement

As mentioned in section 6.3.5, the measured weight of the braking system on the brake force transducer will depend on the position of the brake caliper. The amplifiers therefore needed to be tared before each measurement.

The HBM ClipX LabView library makes it possible to read and write SDO parameter settings directly to the amplifiers from LabView via a TCP/IP network connection. Each amplifier was therefore tared upon program startup, before starting the motor, as shown in Figure 7.5.

The force measurements were converted from analog voltage to force as shown in Figure 7.6. The power was obtained by combining force with the speed sensor measurement.

### 7.2.4 Speed measurement

The raw signal from the FC-03 speed sensor was converted to frequency by using the built-in "Extract Single Tone Information" VI in LabView. The actual rotational speed was then obtained as shown in Figure 7.7.

### 7.2.5 Motor control

The motor was activated by using the digital input function of the SK500e frequency inverter. Because the digital *HIGH*-value for the inverter corresponded to 8 V (higher than the digital *HIGH* from the NI-DAQ), the inverter was activated by sending a constant amplitude analog voltage of

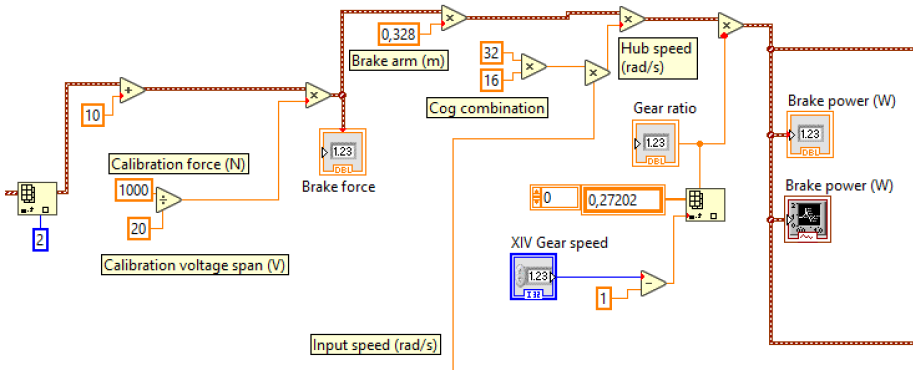


**Figure 7.6:** Calculating force and power from the voltage input

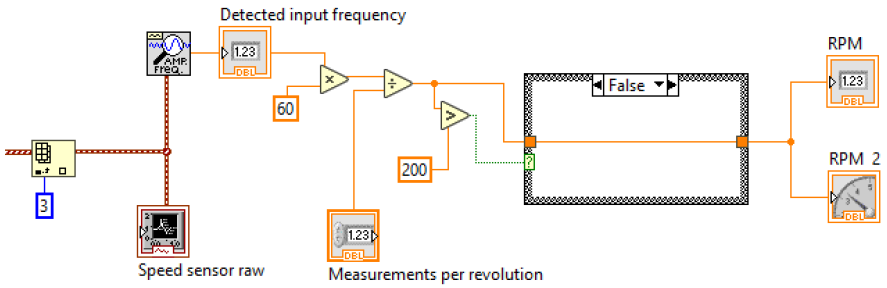


**Figure 7.7:** Calculating input speed from the voltage input

$8V$ from the NI-DAQ to the inverter. The same signal was set to 0 V upon stopping or aborting the program, thus stopping the motor.

The frequency inverter settings were optimized to give the motor a gradual speed ramp during start-up and shutdown. This was especially important when testing the flywheel, to avoid unnecessary stress on the glued connection between the motor axle and the flywheel.

### 7.2.6 Brake actuation

The brake actuation was adjusted by using Actuonix' own software utility, shown in Figure 7.8. The plan was originally to incorporate this functionality into the LabView program, but as the dynamic link library (DLL) for the Actuonix controller board was developed for 32-bit, it was not possible to integrate into a 64-bit LabView application.

The actuator position was adjusted prior to starting the LabView program, to ensure correct tare-values on the force transducers.

### 7.2.7 Efficiency calculation

The efficiency calculation was performed as shown in Figure 7.9. The running mean efficiency was continuously calculated by using shift registers in the while loop.

The sensor data was also written to an .xlsx spreadsheet with the "Write to file measurement" VI.

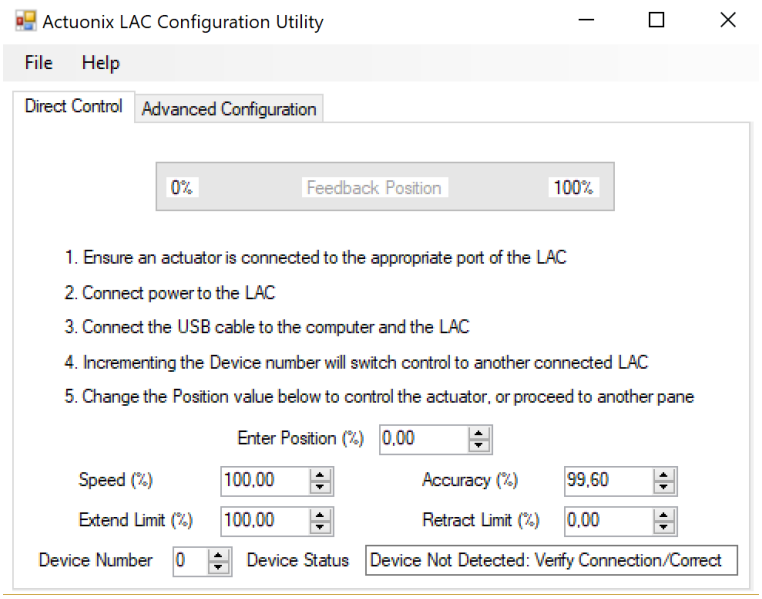


**Figure 7.8:** The Actuonix LAC software utility for controlling the brake power.

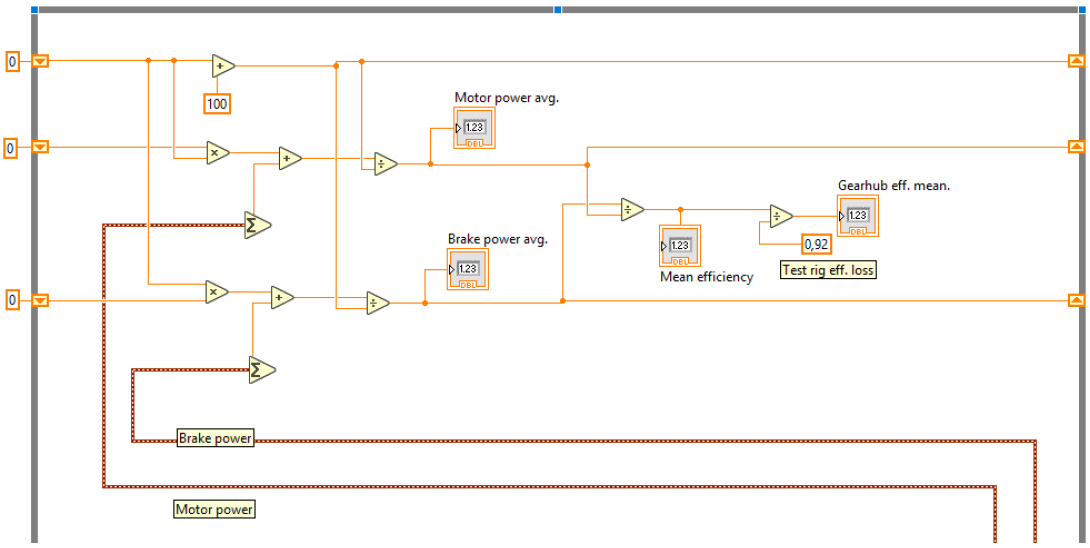


**Figure 7.9:** Calculating the running mean efficiency using shift registers in LabView.

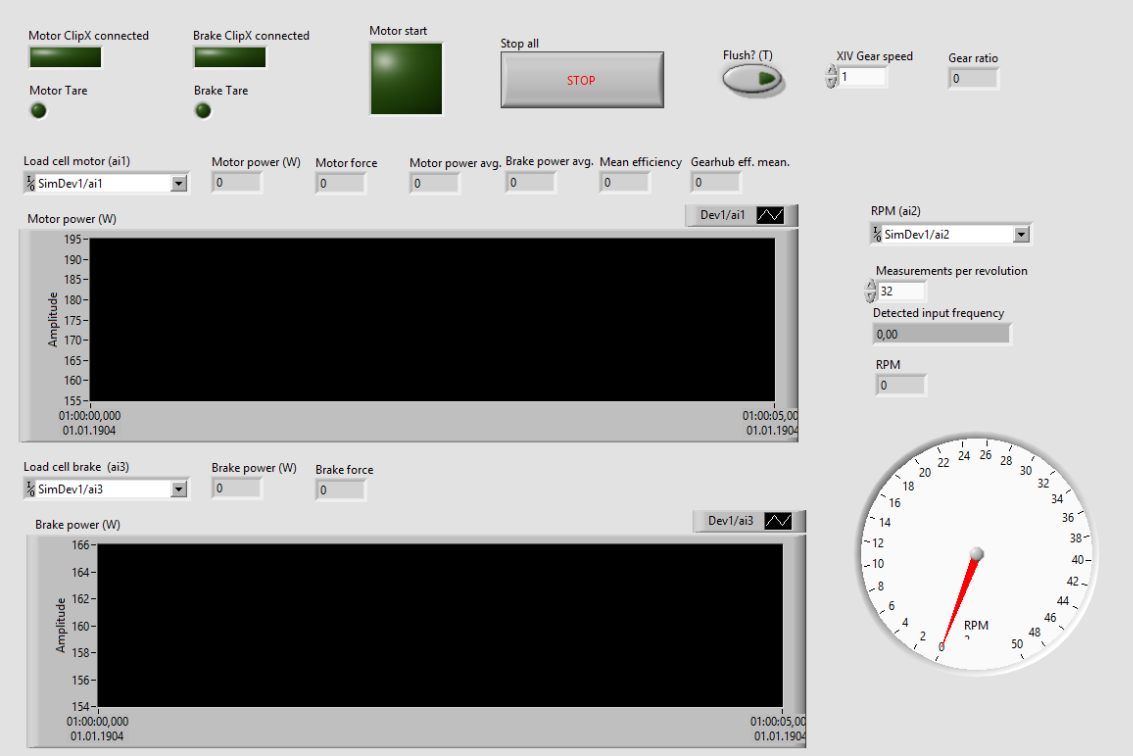


**Figure 7.10:** The front panel of the LabView application.

### 7.2.8 Front Panel

The complete front panel for the LabView program is shown in Figure 7.10. The front panel includes boolean indicators for connection status, tare functions and motor status. The numeric indicators show live measurement data, including mean efficiency. Live charts show the motor and brake power as a function of time.

Drop-down selectors are available for all signal inputs, as well as numeric controls for setting the selected gearhub speed and tooth count on the input shaft sprocket.

# Chapter 8

# Results

This chapter presents results obtained during the project period. First, a comparison between the ECB and the friction brake is shown to demonstrate the large difference in stability between the two systems. This result was the primary reason why the friction brake was discarded, as discussed in Section 6.2. The following results are therefore centered around the development and performance of the ECB system. The results from the incremental stability improvements of the ECB system are then presented. Subsequently, several results for the ECB are shown to more accurately demonstrate the performance of the finished system. Lastly, the results from a preliminary efficiency analysis of the Kindernay XIV gearhub is presented.

## 8.1 ECB and friction brake comparison

Figure 8.1 shows a comparison between the friction brake and the first iteration of the ECB. Both systems were set with constant brake actuation at an average braking power of 215 W. The results were measured using the motor force transducer.

Both systems showed fluctuations around two frequencies:

1. $\sim$ 1 Hz: Matching the rotational speed of the braking rotor
2. $\sim$ 16 Hz: Matching the frequency of the chain on the input cog, as discussed in Section 6.8

Obviously, the friction brake showed considerably worse stability, making the system unsuited for accurate efficiency measurements. The fluctuations created visible movement of the rig during operation and seemed to amplify with increasing load. Measurements of the rotor indicated that it had a slight radial run-out of around 1 mm. Interestingly, the friction brake also seems to excite the 16 Hz fluctuations, as the amplitude is many times larger the fluctuations in the ECB system. The friction brake seemed to be meeting the power requirements as it was able to stop the motor, even at low gear ratios.

The 1 Hz fluctuations were barely visible for the ECB system in Figure 8.1, but were more evident when reducing the y-axis scale. This will be studied in detail in the next sections.

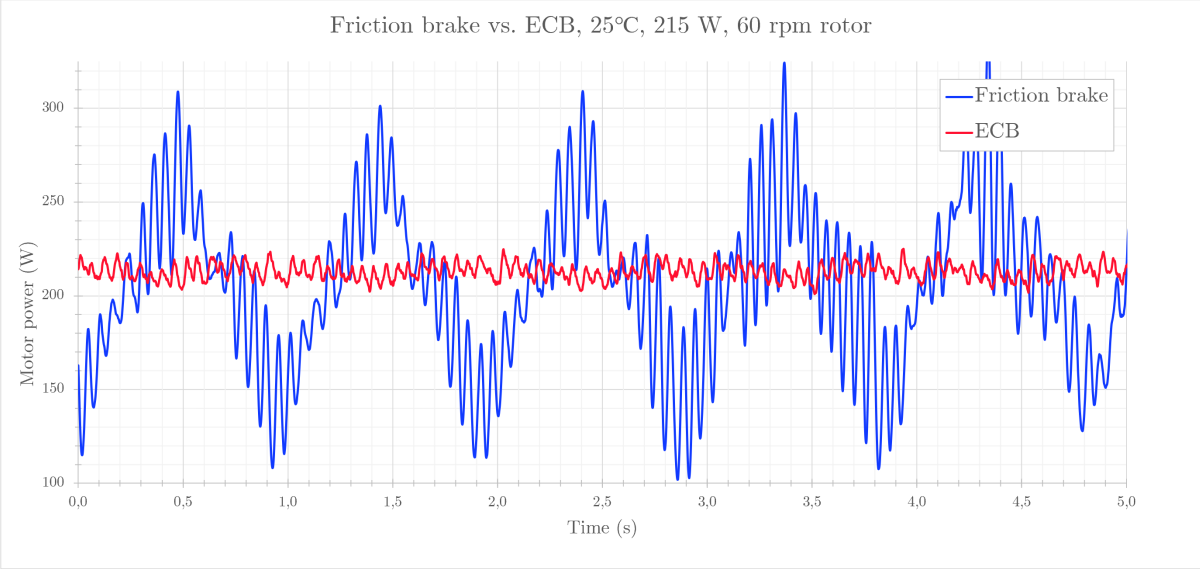


**Figure 8.1:** Comparison between the stability of the ECB and friction brake system

## 8.2 Testing of the ECB

The section presents the results from the continued testing of the ECB.

### 8.2.1 Baseline

Figure 8.2 shows a magnified plot of the force signal when testing the first iteration of the ECB system. The green line represents a 255-period moving average of the same signal, with exponential smoothing to refine the first frequency at 1 Hz. Note that the y-axis is representing force (N) (the speed sensor was not stable at this time, and therefore excluded from the measurement). The ECB was studied and improved on the basis of this result, as will be shown in the following.

### 8.2.2 Results from stability improvements

The results from the stability study and subsequent improvements are presented in the same order as in Section 6.8:

- Figure 8.3 shows the 16 Hz fluctuations vs. the alternating current to the 3-phase motor. Note that the current signal is represented in volts, as this is the output from the ACS712 current sensor (the values are therefore irrelevant)
- Figure 8.4 shows the unmodified ECB and motor compared to the same system with a flywheel connected to the motor
- Figure 8.5 shows the unmodified ECB and motor compared to the same system with a turned (and concentric) ECB rotor

### 8.2.3 Performance

In addition to the stability discussed previously, the performance of the ECB-system was benchmarked on two more parameters, namely maximum power and heat performance. This is represented

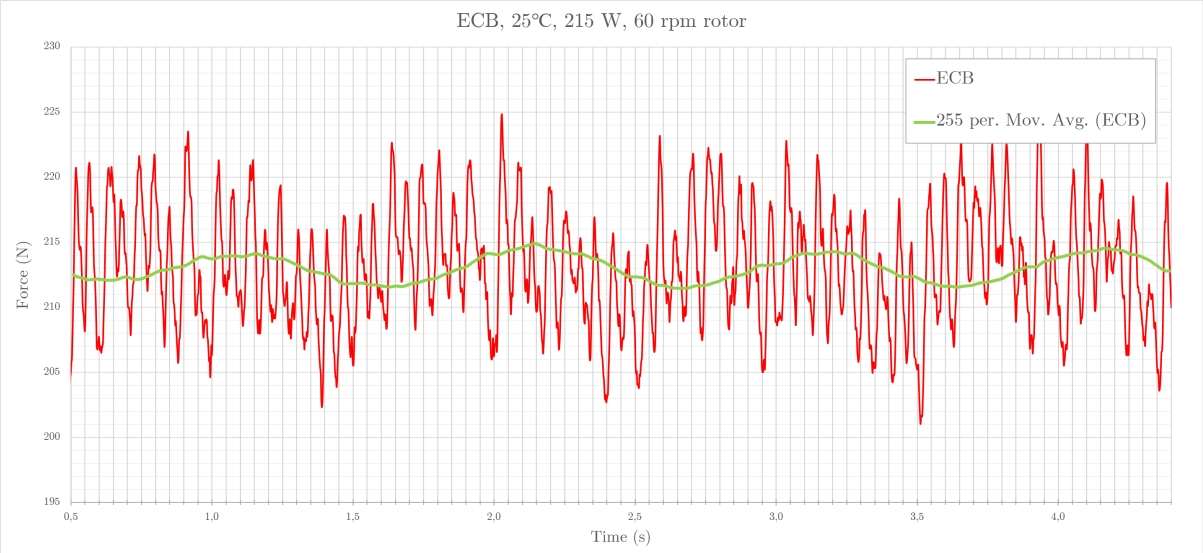


**Figure 8.2:** A magnified view of the oscillations seen in initial testing of the ECB system.

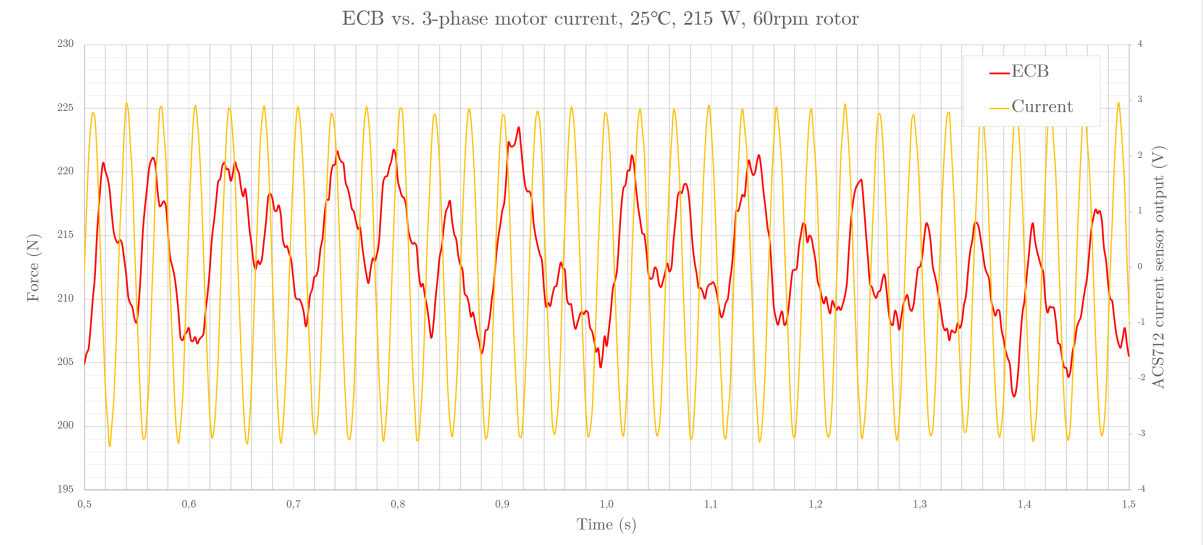


**Figure 8.3:** Comparing the oscillations in the ECB-system to the 3-phase motor alternating current.

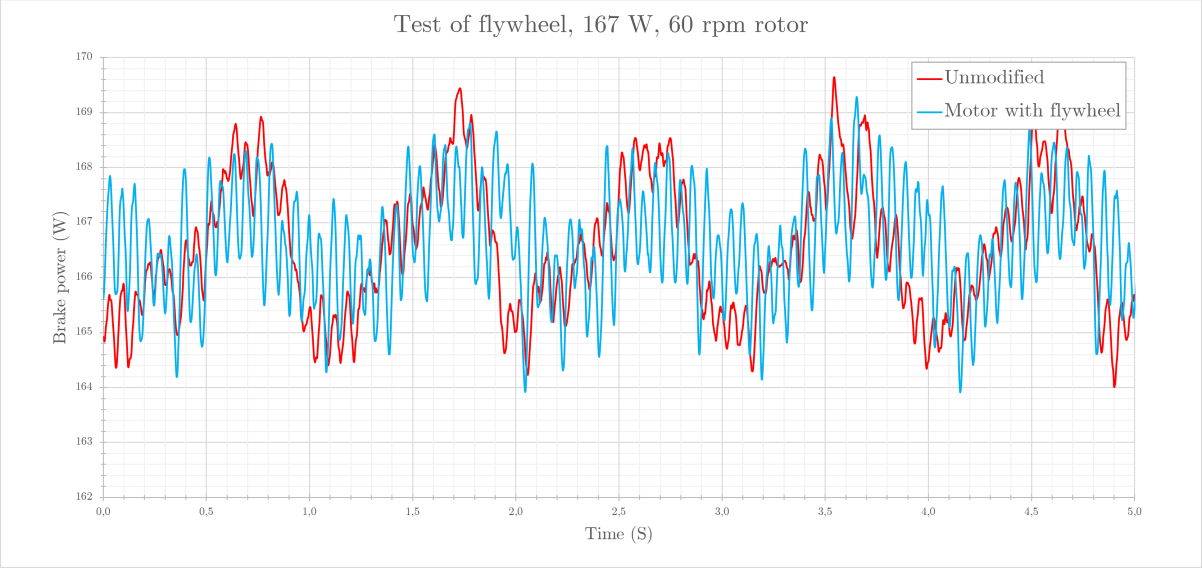


**Figure 8.4:** Comparison between the motor with and without the 9kg flywheel.

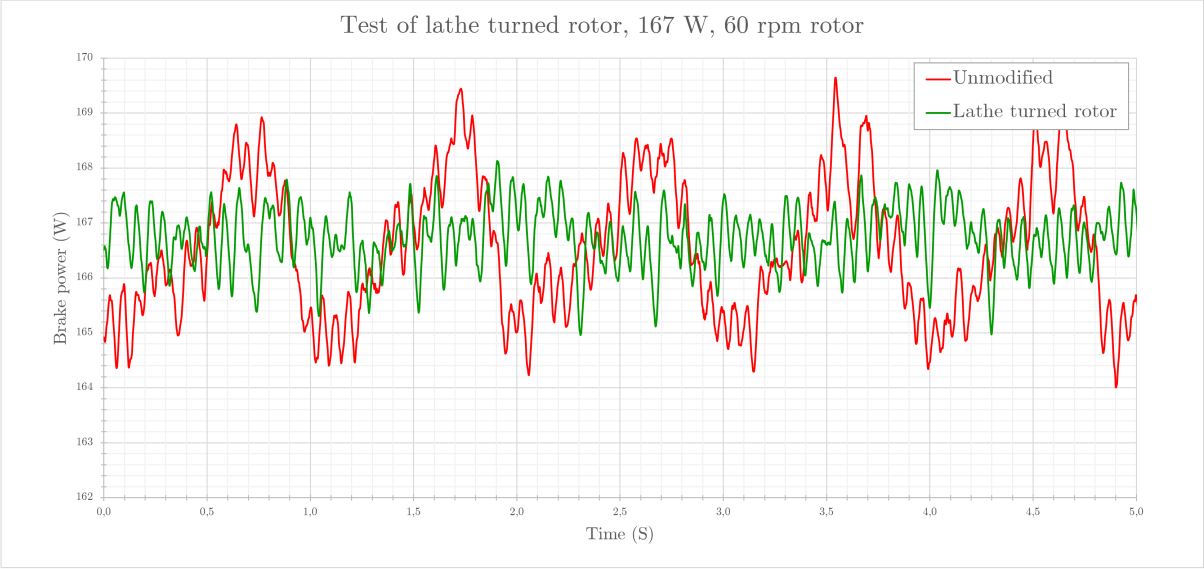


**Figure 8.5:** Comparison between the unmodified and lathe turned ECB rotor.

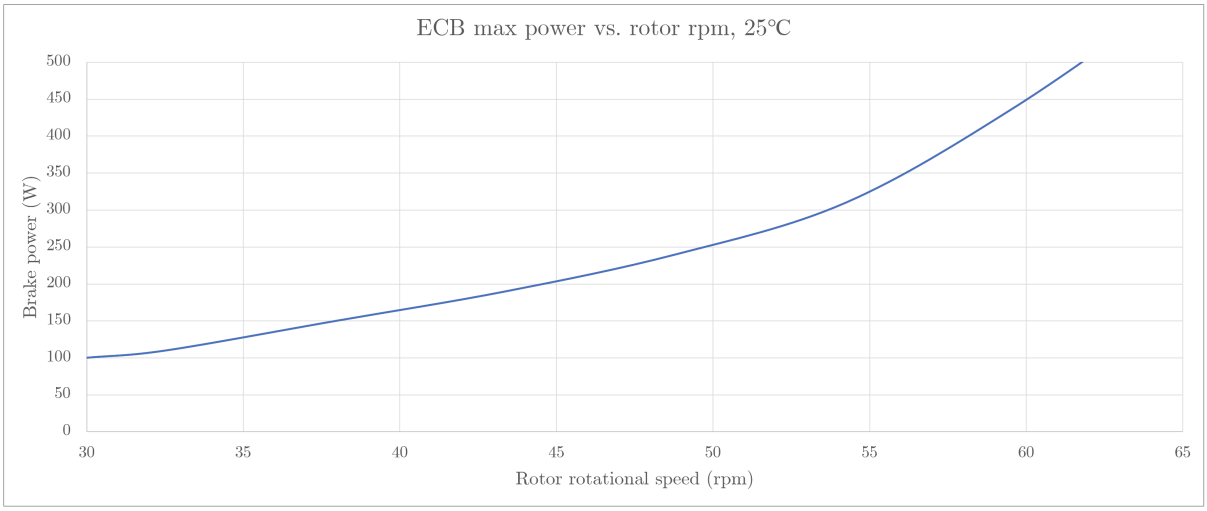


**Figure 8.6:** The maximum power of the ECB showed a non-linear relationship to the rotational speed, as expected.

| Cog ratio | 32/14 = 2,29 | | | | | | | | | | | | | |
|---|---|---|---|---|---|---|---|---|---|---|---|---|---|---|
| Gear | 1 | 2 | 3 | 4 | 5 | 6 | 7 | 8 | 9 | 10 | 11 | 12 | 13 | 14 |
| Gear ratio (inverse) | 0,27 | 0,31 | 0,35 | 0,40 | 0,46 | 0,52 | 0,59 | 0,68 | 0,77 | 0,88 | 1,00 | 1,14 | 1,30 | 1,48 |
| Rotor speed (30 rpm cadence) | 18,7 | 21,2 | 24,2 | 27,6 | 31,4 | 35,7 | 40,7 | 46,4 | 52,9 | 60,2 | 68,6 | 78,1 | 89,0 | 101,3 |
| Rotor speed (60 rpm cadence) | 37,3 | 42,5 | 48,4 | 55,1 | 62,7 | 71,5 | 81,4 | 92,8 | 105,7 | 120,5 | 137,1 | 156,1 | 177,9 | 202,6 |

**Figure 8.7:** The maximum power of the ECB versus the requirements in Table 5.1. The green fields indicate that the system meets the power requirement

by the following Figures:

- Figure 8.6 shows the maximum power of the ECB versus rotor rotational speed
- Figure 8.7 shows the maximum power of the ECB vs. the requirements in Table 5.1
- Figure 8.8 shows power loss from rotor heating

### Maximum performance

As expected, the ECB shows a progressive increase in braking torque for increasing speed. Comparing against the requirement of 400 W at a cadence of 30 rpm, the ECB only meets the maximum power requirement for gear 10-14, as shown in Figure 8.7. For a 60rpm cadence, the requirements are met for all gears but the 1-4. The requirements are met for all gears with a cadence above 90 rpm.

### Power loss from rotor heating

The power loss would be most severe during maximum braking at low rotor speeds, due to the reduced cooling effect from the airflow around the rotor. The test was therefore run at constant

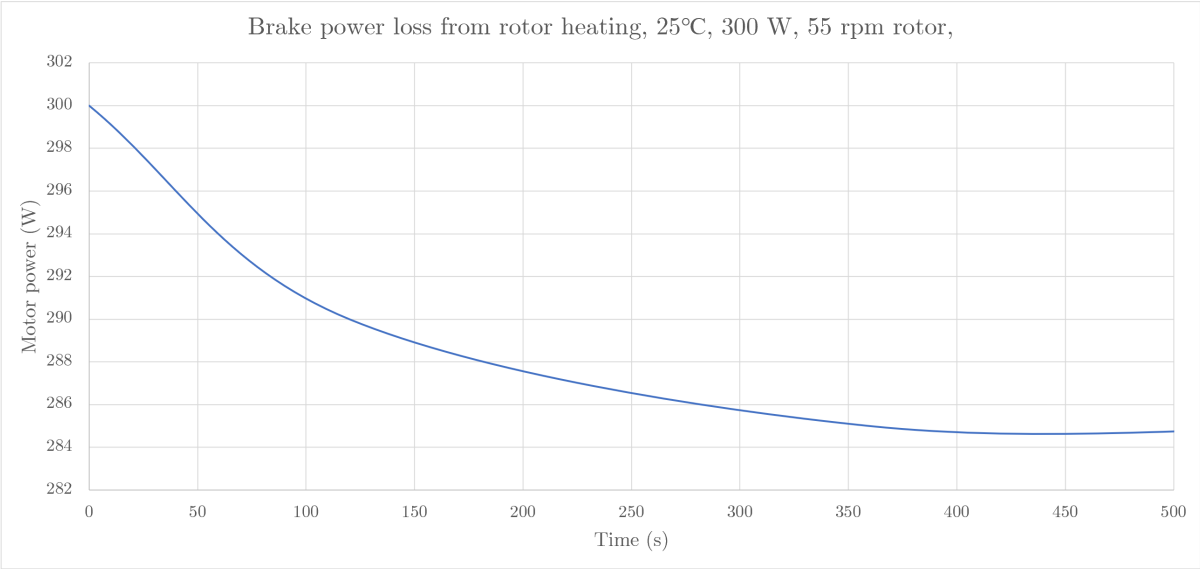


**Figure 8.8:** The ECB showed a slight power loss over time due to rotor heating and reduced conductivity.

speed and maximum ECB engagement with a rotor speed of 55 rpm. The ambient temperature was 25°C and there was no additional cooling.

The rotational speed corresponded to a crank input (motor gearbox speed) of 100 rpm in 1st gear of the Kindernay XIV. The plot shows that the power drops by around 6 W the first minute, and stabilizes at around 285 W after 7 minutes. Running the ECB at the same power level but double rotor speed (partially engaged caliper) resulted in almost no power loss.

### 8.2.4 Constant losses from testing rig

The constant losses from the testing rig were measured using a standard DT Swiss 350 142mm IS 6-bolt rearhub without a rim. To reduce the effect of bearing losses the following measures were taken prior to testing:

- The hub was disassembled to remove the bearing seals and grease from the roller bearings, including the bearings in the freehub body
- The bearings were lubricated sparingly with thin machine oil

The flange bearings supporting the motor gearbox axle were given a similar treatment prior to testing. The tests were performed in 25°C at 100 W with 60 rpm cadence (120 rpm hub input speed). Initial testing showed that the system efficiency increased and stabilized 0.5-1 percentage points higher than the first efficiency result after 2-3 consecutive tests. The system was therefore "warmed up" prior to testing by running at the aforementioned power/cadence combination for 10 minutes. The testing protocol can be described as follows:

- Set the actuator position
- Tare both force transducers
- Ramp up the motor gradually to 60 rpm over 60 seconds, as described in Section 7.2.5

- Perform a 1-minute continuous measurement and calculate the mean efficiency
- Ramp down the motor to 0 rpm over 60 seconds

Each test therefore lasted a total of 3 minutes. After doing 10 independent tests, a mean loss of 93.186% was obtained with a 95% confidence level of 0.768.

## 8.3 Kindernay XIV efficiency testing

Multiple efficiency tests were performed on one sample of the Kindernay XIV gearhub for all gear speeds (1 to 14). The tests were performed at the same power level and cadence as the constant loss test, such that the constant losses could be subtracted from the gearhub test. Due to limited time caused by component delays for the control system, the tests were performed late in the project period, with little time to test additional hub, power and cadence combinations.

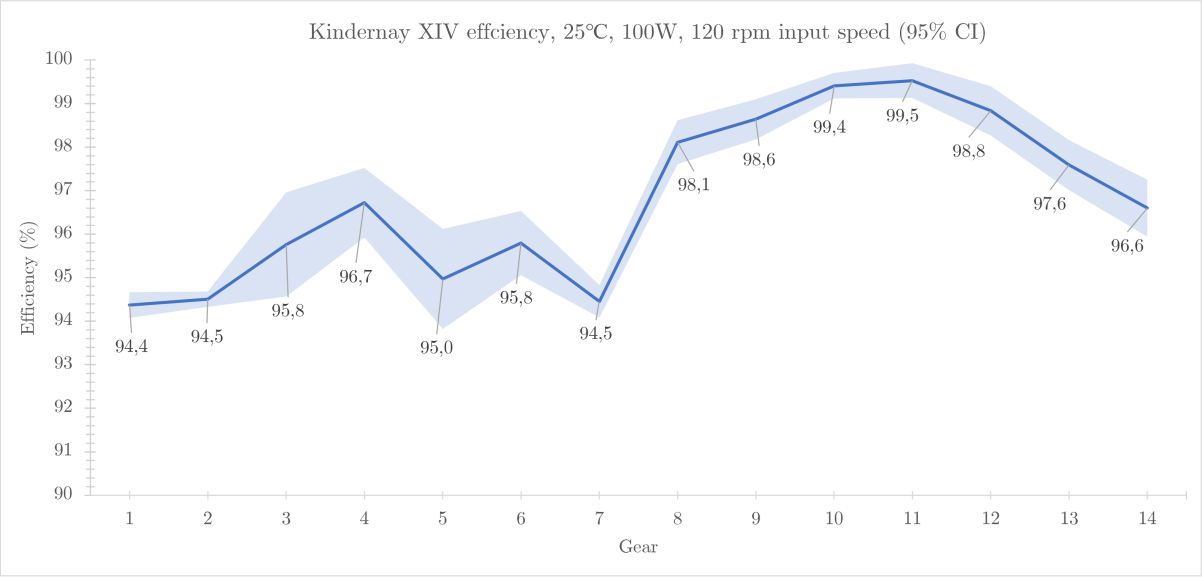


**Figure 8.9:** The efficiency data for the Kindernay XIV gearhub. The data was produced using one individual gearhub.

The efficiency tests were performed using the same test protocol as the constant loss test. 10 independent tests were done for each gear speed. The combined results are shown in Figure 8.9. The mean efficiency value for each gear speed is represented by the blue line, and the 95 % confidence interval is represented by the light blue shading.

# Chapter 9

# Discussion

This chapter intends to present a systematic discussion of the results from Chapter 8, in the same order as the results were outlined. As many of the results are related to previous sections, the discussion will also refer to theory, methods and results in other sections.

## 9.1 ECB and friction brake comparison

The comparison plot in Figure 8.1 is a good illustration of the challenges related to directly mounted brake systems in a measurement rig. Because the relative rotation speed for the rotor is low, the system is more sensitive to oscillating behaviour from component imperfections and eigenfrequencies. This was especially apparent with the friction brake, where a small imperfection caused very large oscillations. The eigenfrequency analysis of the friction brake assembly in Section 6.4.7 did not indicate any eigenfrequencies close to the observed oscillations, and this correlates well with the visual observation of the system during runtime.

The oscillations were believed to be entierly caused by the imperfect lateral trueness of the braking rotor, and not from component resonance. Because of the low rotational speed and consequently high braking forces, the oscillations were very large compared to the mean braking power.

Because of the rotor design discussed in Section 6.4.2 with many spokes large material area, the brake track was quite stiff and had little room for sideways adjustment. This also made it difficult to true the braking rotor. Visual observation also showed that the caliper flex plate exerted little axial movement. The combination of these parameters likely created a system that was too stiff to tolerate the rotor runout. The instability might therefore have been reduced by installing a caliper flex plate from spring steel with minimal thickness and a braking rotor with less material. However, it was still unlikely that the stability would match the ECB system. Moreover, the friction brake would still be highly vulnerable to rotor contamination and handling during installation. Since the system would be removed and installed on a regular basis, this was a considerable downside.

It was therefore clear that the ECB system was favourable for continued development, both in terms of stability and usability.

## 9.2 Testing of the ECB

The results from the various ECB tests in Section 8.2 are discussed next.

### 9.2.1 Baseline result

The baseline result of the ECB showed promising performance, but detailed examination revealed small oscillations in the measuring data. Studying the observed oscillations lead to better understanding of the underlying behaviour caused by the different subsystems.

### 9.2.2 Results from stability improvements

While the stability improvements performed in Section 6.8 had mixed results, the results still produced valuable knowledge. The main takeaways from the stability improvements can be summarized in the following points:

1. Neither current measurements or the change of operation mode to V/f characteristic curve on the inverter showed any correlation or improvement versus the observed oscillations in Figure 8.3. This would indicate that the motor operated in a stable manner, not contributing to the oscillations
2. The flywheel installation supported this conclusion in that no stability improvements were observed
3. The rotor turning modification showed significant improvement in stability and was likely the single cause of the 1 Hz fluctuations. This gave a clear indication of just how sensitive the ECB was to radial runout on the rotor, especially when actuating the caliper radially

The rotor runout turned out to be problematic when adapting the outer braking rotor to a different hub/spider combination, as a tiny misalignment would cause measurement oscillations. It would therefore be ideal to manufacture one rotor for each brake disc interface, for instance 6-bolt IS, 7-bolt Kindernay and 4-bolt Rohloff.

The actual effect of the oscillations on the mean efficiency measurements could also be discussed. As Figure 8.7 shows, the 1 Hz oscillations were not that significant compared to the mean power level. However, it would always be best to compare different hub systems on a similar basis, and therefore reduce the oscillations as much as possible before each test.

### 9.2.3 Performance

As Figure 8.7 shows, the ECB did not meet the performance requirements defined in Table 5.1 for all gear combinations of the Kindernay XIV. The plot in Figure 7.6 illustrates well how the progressive behaviour is unsubstantial below a rotor speed of 50 rpm, where the braking power is limited. The real world braking torque was therefore differing considerably from the theoretical calculations in Section 5.5.1. This can likely be explained by the fact that Gosline and Haywards model [20] does not account for the fringing effect. As the rotor thickness was set to 15 mm, a large total air gap was required between the magnet caliper plates, likely causing a considerable fringing effect. The large contrast between Gosline and Haywards model is something that Hukkelås [18] also observed in his results.

While it is interesting to test the gearhubs at as many power and speed combinations as possible, this would not be a necessity for comparing the gearhub between different competitors. In retrospect, especially the 400 W requirement at 30 rpm is not very realistic for the lower gears, as traction would be limited because of the high torque. If instead increasing the rotor speed to 60 rpm, the power is raised significantly and the ECB meets the power requirement for gear 5-14. Still, it would

be desirable to increase the performance of the ECB systems at lower rotor speeds. This could be done in multiple ways without deviating from the original concept:

- Decrease the air gap between the ECB caliper plates from 2 mm to 1 mm: Runout measurements during loading indicated that radial true of the ECB rotor was good enough to accept the reduced clearance
- Increase the number of magnets on the magnet caliper: The brake performance could be increased considerably by installing three instead of two magnet pairs.

Obviously, the ECB has a lot of variables that determine its ultimate performance characteristics. The continued development and usage of the testing rig could benefit from studying the characteristics of the ECB further, and experiment with various parameters like rotor thickness, air gap and materials.

### 9.2.4 Constant losses from testing rig

The result of 93.2 % from the constant loss test in Section 8.2.4 performed with the DT 350 rearhub showed worse performance than expected for a regular chain transmission [4]. The losses were likely not caused by the hub only, as the DT 350 hub showed very low rolling resistance after optimizing the roller bearings. Moreover, the 0.5 percentage point difference between the DT 350 hub and Kindernay XIV 11th gear (with multiple grease-lubricated roller bearings) indicated that the bearing losses were small compared to the total testing rig efficiency loss.

The flange bearings supporting the gearhub axle would also contribute to the constant rig losses. The roller bearings were degreased similarly to the DT 350, but are still large compared to bicycle hub bearings and likely have higher constant losses. It is still unlikely that they gave a significant contribution to the efficiency loss.

By studying the chain transmission it was observed that the chain did not ride smoothly on either of the sprockets. The 32T input sprocket was an industrial component with wider teeth and rough machining surfaces compared to average bicycle sprockets. This required the use of a wider chain that was a poor fit on both sprockets. It is highly possible that this transmission caused higher losses compared to a conventional bicycle chain transmission with optimized sprockets and chain. Future improvements of the testing rig should therefore include replacement of the 32T sprocket with a specific bicycle sprocket and chain to investigate the constant losses further.

## 9.3 Kindernay XIV efficiency testing

The efficiency plot for the Kindernay XIV gearhub in Figure 8.9 shows results that largely correlate to the expected relative efficiencies discussed in Section 2.3.

First of all, there is a clear jump from 7th to 8th gear by almost 4% when the reduction gear is disabled. This is also noticeable when riding the gearhub on a bicycle uphill, and supports the theory of worse efficiency in the reduction gear compared to the two other planetary series.

Also noticeable is the peak efficiency in 4th and 11th gear for the low and high range, respectively. This is to be expected from the data in Table 2.1, as neither of the first two planetary series are enabled. Hence, the comparison between 4th and 11th gear essentially shows the effect of the reduction gear alone, even if considering increased splash losses and speed dependant losses.

Looking at trend from gear 1-7 and 8-14, one would expect to see a similar curve shape, with gear 8-14 noticeably higher in the efficiency range. This is due to the fact that many of the same mechanisms are working in gear 1 and 8, 2 and 9 and so on, apart from the reduction gear and G-clutch. This is largely the case, although not for all gear combinations. Gear 1-4 and 8-11 show a similar trend, but 5th gear shows a larger efficiency drop than 12th gear, compared to the previous gear. This behaviour is difficult to explain with the data from Table 2.1. It could potentially be caused by the reduction gear hitting a resonance frequency, and for this reason it would be valuable to test several gearhubs to see if the efficiency relation differs.

Another interesting result is that the efficiency in 14th gear is considerably worse than 8th gear. This relation is not true for the low series, where 7th gear has slighty better efficiency than 1st gear. This effect might be explained by the increasing splash losses that become significant with the increasing speed in the higher gears.

A short note is also made regarding the actual efficiency values. Compared to the Rohloff efficiency values discussed in Section 3.1 the XIV gearhub seems to produce competitive efficiency values, especially considering the test is performed at a low power level of only 100 W.

While the results for the XIV hub are promising, they are not comprehensive enough to confidently represent expected efficiency data for production units. Future testing of the gearhub should include more tests on multiple gearhub samples, and on different power and speed combinations. In addition, an uncertainty analysis should be performed with basis in the accuracy of the testing equipment. This is especially important if deciding to compare the data to competing products and publish the data. As seen in Section 2.4, the scientific quality and methods of previous efficiency-studies is highly variable, as illustrated by diverging results. The company would therefore benefit from publishing an open and thorough study that tests gearhubs on equal and realistic terms. The test should be described in sufficient detail so that the results can be reproduced.

The variability observed in the measurements can largely be explained by the accuracy class and maximum load rating of the force transducers. Since the measurements were performed at only 100W, the forces on the brake force transducer varied from 89 N down to 16.5 N. An accuracy class of 0.2 % for 1000N measuring range could therefore lead to quite significant errors of up to 12 % for the lower force values. The force transducers ordered early in the project phase were therefore not optimal for the performed efficiency tests. Considering that most quality tension/compression force transducers have accuracies between 0.1-0.2 %, it would not be possible to meet the requirement of 0.5 % accuracy across all power/cadence combinations with a single load cell capacity. For the best possible results in future testing it would therefore be ideal to use multiple sets of force transducers with different load ratings, depending on the power level to be tested.

## 9.4 Comparison to requirement specification

An evaluation of finished testing rig and the requirements from Section 3.3 is shown in Table 9.1, showing that the testing rig satisfy all requirements related to usability and compatibility. The requirement related to accuracy is dependant on the measuring equipment used. It is not satisfied with the current force transducers for all loading scenarios, but could be satisfied with force transducers with higher accuracy and lower absolute capacity, as previously discussed. For instance, the HBM U9C [24] with 100 N capacity would give 10 times better accuracy compared to the current transducers.

Producing valid and reliable measurements would to a large extent depend on the stability of the

| No. | Requirement | Satisfied (old) | Satisfied (new) |
|---|---|---|---|
| 1 | Total measurement sensitivity of ±0.5% | No | No[1] |
| 2 | Compatibility with 10×135 mm and 12×142 mm axles | No | Yes |
| 3 | Adjustable power with $P_{max} = 400$ W | Yes | Yes |
| 4 | Max torque of $T_{max} = 130$ Nm | Yes | No |
| 5 | Motor output speed $\omega_{motoroutput} = 30 - 120$ rpm | Yes | Yes |
| 6 | Stationary construction requiring little setup time | Yes | Yes |
| 7 | Easily movable by pallet jack | Yes | Yes |
| 8 | Space efficient | Yes | Yes |
| 9 | Quick wheel removal/insertion | Yes | Yes |
| 10 | Rim size/profile compatibility | No | Yes |
| 11 | Clearance for shifting mechanisms | Yes[2] | Yes |
| 12 | Shifting gears during run-time | Yes | Yes |
| 13 | Test hubs without rim | No | Yes |
| 14 | Wheel true dependency | No | Yes |
| 15 | Kindernay XIV/VII compatibility | Yes | Yes |

[1] Satisfied if aquiring force transducers with correct resolution and accuracy
[2] Requires new sliding dropouts and adapter for caliper arm

**Table 9.1:** Requirements comparison with new and old configuration.

system during loading. As observed in the functional analysis, the stability of the testing rig during run-time can be affected by several subsystems. The motor, transmission systems and brake system all have to function in an optimum manner.

### 9.4.1 Discussion around the direct mounted brake concept

The current ECB brake was conceptualized with a limited design space, both because of the existing frame geometry and the usability requirement related to fitting bicycle wheels with various rim widths. From the preceding discussion around stability and performance it is apparent that coupling the ECB braking system with a chain transmission (or similar) could have several advantages:

- The ECB system could be placed further away from the wheel/hub, allowing for a wider design space
- The ECB rotor could be geared to increase the rotor speed, thereby reducing the size and increasing the performance
- The ECB caliper could be actuated axially instead of radially, and therefore be less susceptible to oscillations from rotor runout

This would of course require a completely different rig design, and many of the structural considerations made in the previous chapters would have to be rethought. The knowledge and insight gained through this project would still be valuable in the development.

## 9.5 Summary of research questions and results

| **Research question** | **Relevant sections** |
|---|---|
| 1.1: Which subsystems cause the observed instability and compatibility issues? | 4.2 |
| 1.2: How can these subsystems be improved? | 5.2, 5.3, 5.4 |
| 2.1: How can the in-going and out-going power be measured in an accurate and repeatable manner? | 6.1 |
| 2.2: Which requirements are necessary to ensure compatibility with the most common gearhub systems on the market? | 3.1, 3.2 |
| 2.3: How can the suggested solutions be implemented in accordance with these requirements? | 6.1, 6.3, 6.5 |
| 3.1: How is the control system hardware coupled together? | 7.1 |
| 3.2: How should the testing rig be calibrated to deliver accurate results? | 6.7, 7.2.3 |
| 3.3: How is the testing rig accuracy affected by the measuring equipment? | 6.7, 7.1.1, 9.3 |
| 4.1: How can mechanical losses in the testing rig be accounted for? | 8.2.4, 9.2.4 |
| 4.2: How does the gearhub efficiency vary in different gears of the gearhub? | 8.3, 9.3 |
| 4.3: Why does the gearhub efficiency vary in different gears of the gearhub? | 2.2, 2.3, 9.3 |

**Table 9.2:** An overview of the relevant sections for the research questions.

The objectives and research questions outlined in Section 1.3 were answered in multiple sections of this thesis. A summary of relevant sections for each research question is given in Table 9.2 for the readers convenience.

# Chapter 10

# Conclusion

This project set out to examine and improve the functionality of a gearhub efficiency testing rig in a Norwegian company. Initially, the goal was to perform a complete efficiency comparison between all the gearhubs mentioned in Section 3.1, but in retrospect this was somewhat optimistic considering the developmental challenges and component delivery issues during development of the ECB- and control system.

The symptoms described by the company were mainly related to uneven operation and poor compatibility. While the functional analysis confirmed this information, there was no obvious cause – rather, it seemed to be a combination of poorly performing sub-systems. Investigating each subsystem separately gave a clearer picture of the underlying problems, indicating that the motor, V-belt transmission system and brake all contributed to the observed instability. Configuring the motor parameters made a significant improvement, although the braking system still showed significant oscillations.

On the basis of these results, it was decided to redesign the braking system. This was a challenging task that needed to satisfy many adverse requirements. It consumed more time and effort than anticipated, but as the testing rig would be used in future development, calculated changes were prioritized above project pace.

Two brake systems were conceptualized, a friction brake and an ECB system. The latter had clear advantages – the improved testing rig meets all requirements related to usability and compatibility. The combination of the ECB brake and new motor settings improved the stability of the rig to a level where accurate efficiency measurements are possible. However, the accuracy still depends on the precision and capacity of the measuring equipment. It is not possible to meet the required accuracy and performance requirements with only one set of force transducers, and the company should consider investing in multiple force transducers if testing all the power and cadence combinations is a continued priority.

In its current state, the ECB system does not meet the all the performance requirements originally set by Myklestad [9] and the company. Still, the relevance of the maximum power tests at low rpm is questionable, and not critical to satisfy many of the intended use cases. In addition, the performance can likely be improved with little effort, by optimizing the air gap or adding additional magnets.

The efficiency testing rig has many use cases for the company, including testing and comparison of new components and products, as well as competitive gearhub systems. Many of these use cases can

be fulfilled with the current testing rig, but the range of use cases can also be expanded to commercial applications if investing time in improving accuracy and performing a thorough uncertainty analysis of the complete system.

The efficiency analysis of the Kindernay XIV gearhub gave results that correlated well with the planetary transmission theory. With the current accuracy of the testing rig, the results are subject to significant uncertainty however, especially since they are calculated with basis in constant losses in the testing rig. Thus, the data is primarily of a qualitative degree at the current stage, and the absolute efficiency values should not be given too much emphasis. Still, there is reason to believe that the XIV is highly competitive to other efficient gearhubs on the market like the Rohloff Speedhub [8].

The observed offset between the curve shape of the low (1-7) series and high (8-14) series, especially in gear 5 and 12, could not be directly explained from the gearhub theory. The hypothesis is that it might be caused by resonance in the reduction gear, but there was little time to study this further. The gearhub contains a multitude of mechanisms at play, whose effects on the efficiency are largely unknown and can cause unexpected results like this. This is a good argument for performing more testing at several power and speed combinations, and on more than one gearhub sample.

From an educational perspective, the project involved many different scientific subjects, some of which were outside the academic discipline of the author. In addition, the project process was also of great variability, comprising theoretical studies, practical tasks and construction of new solutions. The project has therefore been a learning process, and the opportunity of being part of a company project has been highly rewarding and a great motivation for continued work in the field of mechanical engineering and ICT.

## 10.1 Recommendations for further work

The development and use of the testing rig will continue as an internal company project after submission of this thesis. The author will likely participate in the continuing work on the testing rig, with the objective of improving measurement precision and performance. The steps towards this objective can be summarized as follows:

1. **Study and improve ECB performance:** Continued work on the testing rig will greatly benefit from further studies of the ECB-system. While the stability of the current system is good, the performance should be increased to be able to test gearhubs with low gear ratios at higher power levels.
2. **Improve the ingoing chain transmission:** The 32T sprocket on the gearbox axle should be replaced with a bicycle-specific sprocket so that a regular bicycle chain can be installed.
3. **Implement force transducers with correct load rating:** As discussed in Chapter 9, the continued testing should be performed with force transducers with load ratings optimized for the testing load.
4. **Uncertainty analysis:** An uncertainty analysis should be performed based on the accuracy of the testing equipment.
5. **Control system HW-improvements:** A speed sensor for the gearhub rotational speed should be implemented for testing gearhubs with unknown (or inaccurate) gear ratios. The shifting could be software controlled if implementing hardware actuators for the shifting levers.

6. **Control system automation:** The current LabView implementation is dependent on the operator stopping and starting each test. If performing multiple tests, the program can be expanded to run a pre-set number of tests, and store all the mean efficiency values. The program could be further automated by implementing shifting actuation as mentioned above. The program could then run a complete test set for all gear combinations.
7. **Continued efficiency testing:** As discussed in Chapter 9, the continued testing should include more samples of the XIV gearhub, as well as competitor gearhubs. The latter can be compared with results from the studies outlined in Section 3.1 to further verify the data.
8. **HSE implementation:** Once the testing rig is fully operational, it is important to implement HSE-measures that ensure optimum safety for the operator and surroundings. The greatest dangers with the current setup is the rotating ECB rotor and wheel. Implementing plexiglass shielding around the ECB and bicycle wheel would greatly reduce the risk of injury during operation.
9. **Documentation:** The functionality, operation and maintenance of the testing rig must be documented for future use.

# Bibliography


[1] Herbert W. Müller. *Epicyclic Drive Trains: Analysis, Synthesis, and Applications*. Wayne State University Press, 1982. ISBN: 978-0814316634.

[2] *Conservation of energy*. [Accessed 24.02.20]. URL: https://en.wikipedia.org/wiki/Conservation_of_energy.

[3] road.cc. *Shimano Dura Ace 9100*. [Accessed 01.02.20]. 2016. URL: https://road.cc/content/tech-news/207047-shimano-dura-ace-9100-first-ride-review.

[4] Michael J. Ehrlich James B. Spicer Christopher J.K. Richardson and Johanna R. Bernstein. *On the efficiency of bicycle chain drives*. [Accessed 24.02.20]. 2000. URL: http://www.ihpva.org/HParchive/PDF/hp50-2000.pdf.

[5] Elizabeth A. Casteel and Mark Archibald. *A Study on the Efficiency of Bicycle Hub Gears*. [Accessed 09.02.20]. 2013. eprint: https://asmedigitalcollection.asme.org/IMECE/proceedings-pdf/IMECE2013/56420/V013T14A044/2487515/v013t14a044-imece2013-64507.pdf. URL: https://doi.org/10.1115/IMECE2013-64507.

[6] Steven Weinberg. *Planetary Gears – a masterclass for mechanical engineers*. [Accessed 02.04.20]. 2018. URL: https://www.engineeringclicks.com/planetary-gears/.

[7] Ph.D. Frank Berto Chester R. Kyle. *The mechanical efficiency of bicycle derailleur and hub-gear transmissions*. [Accessed 15.01.20]. 2001. URL: http://www.ihpva.org/HParchive/PDF/hp52-2001.pdf.

[8] Rohloff AG. *EFFICIENCY MEASUREMENT OF BICYCLE TRANSMISSION*. [Unknown publication date, accessed 22.06.20]. URL: https://www.rohloff.de/en/experience/technology-in-detail/mechanical-efficiency/efficiency-measurement.

[9] Testrigg for Kindernay XIV. *Hallvard Askeland Myklestad*. [The thesis is confidential but has been included in the upload on Inspera]. 2018.

[10] *MILESTONES Highlights from over 30 years of company history*. [Accessed 06.02.20]. URL: https://www.rohloff.de/en/company/rohloff-ag/milestones.

[11] *A12-mounting check and retrofitting a Rohloff SPEEDHUB A12 hub into 12mm Thru-axle frames*. [Accessed 06.04.20]. URL: https://www.rohloff.de/fileadmin/user_upload/Rohloff-A12-beide_Messmethoden-EN-18092017.pdf.

[12] *NuVinci® Technology*. [Accessed 10.02.20]. URL: https://www.fallbrooktech.com/nuvinci-technology/.

[13] *NUVINCI® N360® HUB INSTALLATION AND ADJUSTMENT*. [Accessed 07.03.20]. URL: https://www.parktool.com/blog/repair-help/nuvinci-n360-hub-installation-and-adjustment.

[14] *Internal Gearhubs*. [Accessed 02.02.20]. URL: https://www.sheldonbrown.com/internal-gears.html.

[15] *Sturmey-Archer Heritage*. [Accessed 03.02.20]. URL: http://www.sturmey-archerheritage.com.

[16] *NORD Drivesystems SK5XX frequency inverter manual*. [Accessed 03.02.20]. URL: https://www.nord.com/cms/no/documentation/manuals/details_1139/detail_7443.jsp.

[17] *Chordal Action of Chains*. [Accessed 10.06.20]. URL: http://chain-guide.com/basics/2-2-1-chordal-action.html.

[18] Control of Eddy-Current Brakes. *Snorre Hukkelås*. [Accessed 01.04.20]. 2018. URL: http://hdl.handle.net/11250/2563281.

[19] Chetvorno. *Eddy current brake diagram – From Wikimedia Commons, the free media repository*. [Accessed 16.05.20]. 2017. URL: https://commons.wikimedia.org/wiki/File:Eddy_current_brake_diagram.svg.

[20] A. H. Gosline and V. Hayward. 'Eddy current brakes for haptic interfaces: Design, identification and control'. In: *IEEE/ASME Transactions On Mechatronics* 13 (2008).

[21] *Alligator Hydrahose ULTIMATE$^{TM}$ ø5 MM*. [Accessed 21.03.20]. URL: https://www.alligatorcables.com/ultimate-5-mm.html.

[22] *Specific Heat of common Substances*. [Accessed 17.02.20]. URL: https://www.engineeringtoolbox.com/specific-heat-capacity-d_391.html.

[23] *Flintec Y1 In-line Threaded Force Sensor*. [Accessed 23.03.20]. URL: https://www.flintec.com/weight-sensors/force-sensors/miniature/y1.

[24] *U9C Miniature Load Cell: for Measurement of Tensile and Compressive Force*. [Accessed 23.04.20]. URL: https://www.hbm.com/en/3926/u9c-miniature-force-sensor-for-tensile-and-compressive-forces/.

[25] *The Original K&J Magnet Calculator*. [Accessed 10.06.20]. URL: https://www.kjmagnetics.com/calculator.asp.

[26] *The best MTB disc brake you can buy*. [Accessed 05.03.20]. URL: https://enduro-mtb.com/en/best-mtb-disc-brake-can-buy/.

[27] Takaaki Matsuda. *A novel stainless steel for a disc brake rotor*. European Patent EP1199374A1. 54 2002. URL: https://patents.google.com/patent/EP1199374A1.

# List of Appendices

# Appendix A

# Tables

## A.1 Results from gearhub study

The relevant parameters for the studied gearhubs in Section 3.1 are shown in Table A.1.

**Table A.1:** Overview of different gearhub systems

| Make/Model | Housing | Internal axle | Supported Axle standards | Brake disc bolt pattern | Shifting | Driving cog | Torque arm |
|---|---|---|---|---|---|---|---|
| Kindernay XIV | Two-piece | 12mm hollow | 12x148, 12x142, 10x135mm | 7-bolt proprietary | Drive side[1] | Standard | Non-drive side |
| Kindernay VII | One-piece | 12mm hollow | 12x148, 12x142, 10x135mm | IS 6-bolt | Drive side;[1] hydraulic | Proprietary | Non-drive side[2] |
| Rohloff Speedhub | One-piece | 5mm hollow | 12x148;[3] 12x142;[3] 10x135mm | 4-bolt proprietary | Non-drive side, cable | Proprietary | Non-drive side |
| Enviolo/ Nuvinci | One-piece | 10mm solid | 10x135mm | IS 6-bolt | Drive-side, cable | Standard | Non-drive side |
| Shimano Nexus/Alfine | One-piece | 10mm solid | 10x135mm | Centerlock®[4] | Drive-side, cable | Proprietary | Non-drive side |
| Sturmey Archer | One-piece | 10mm solid | 10x135mm | IS 6-bolt | Drive-side, cable/chain | Proprietary | Non-drive side |
| SRAM G8 | One-piece | 10mm solid | 10x135mm | IS 6-bolt | Drive-side, cable | Proprietary | Non-drive side |

[1] Structural part
[2] Integrated into hub end cap
[3] Frame-dependant adapters, no thru axle
[4] Convertible to IS 6-bolt with adapter

# Appendix B

# Pictures of the finished testing rig

## B.1 ECB components

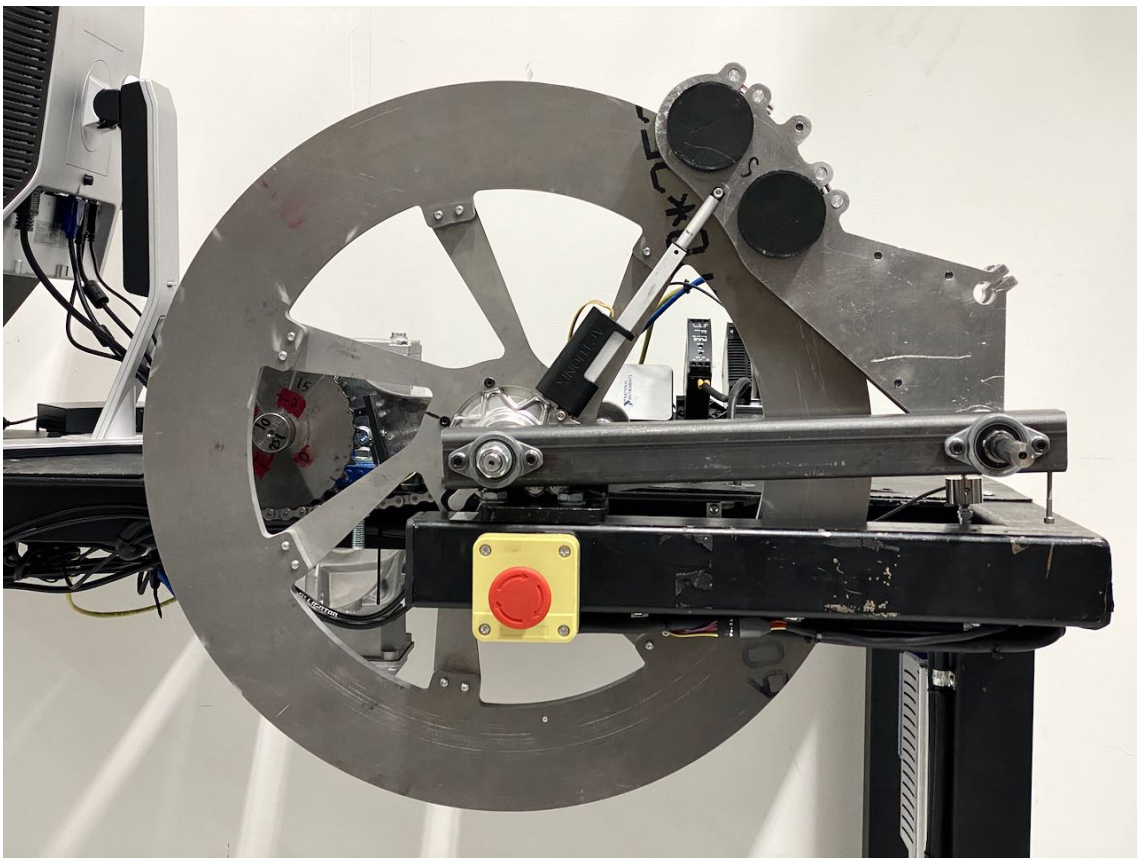

**Figure B.1:** Front view of the ECB.

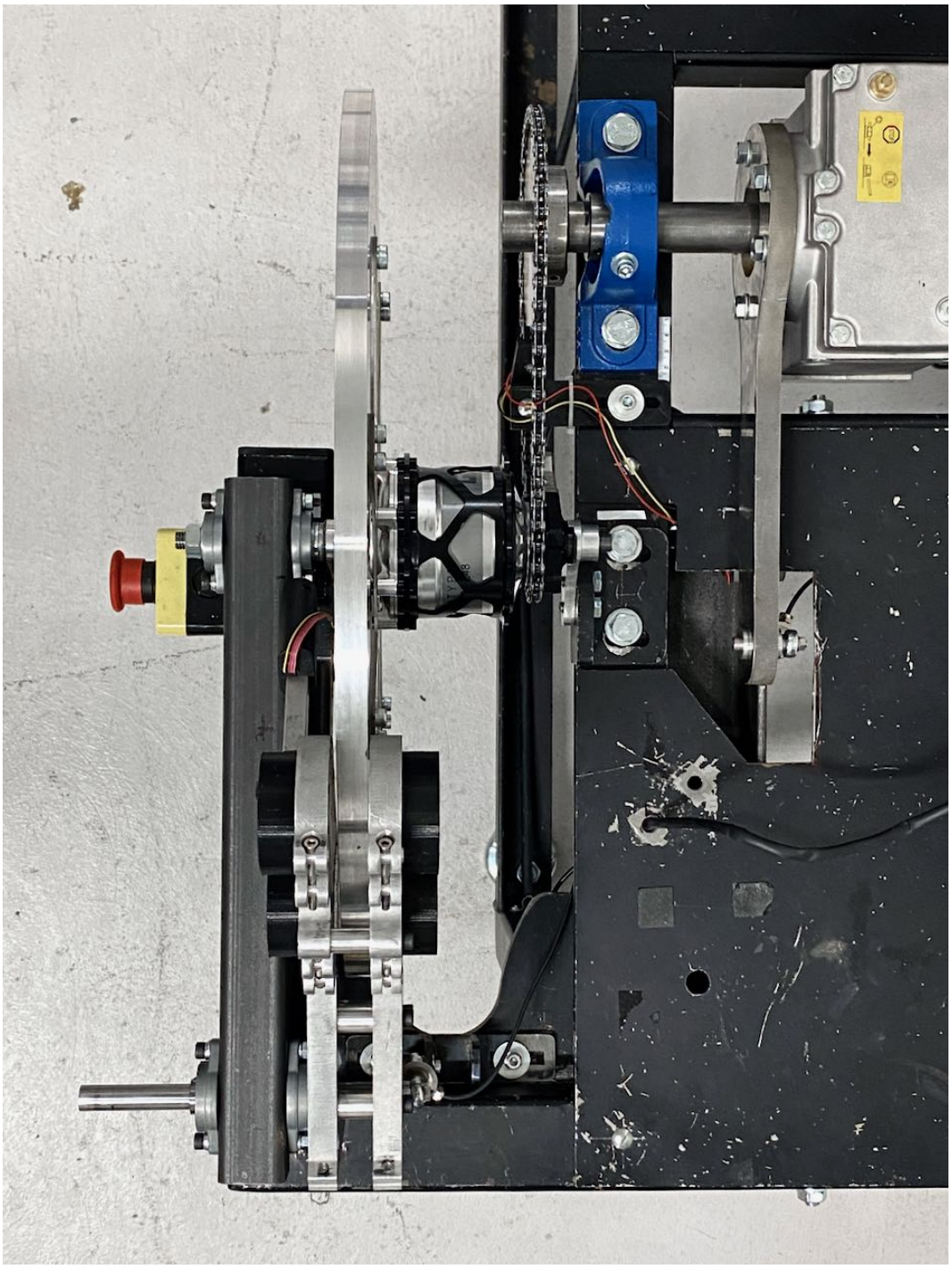

**Figure B.2:** Top view of the ECB.

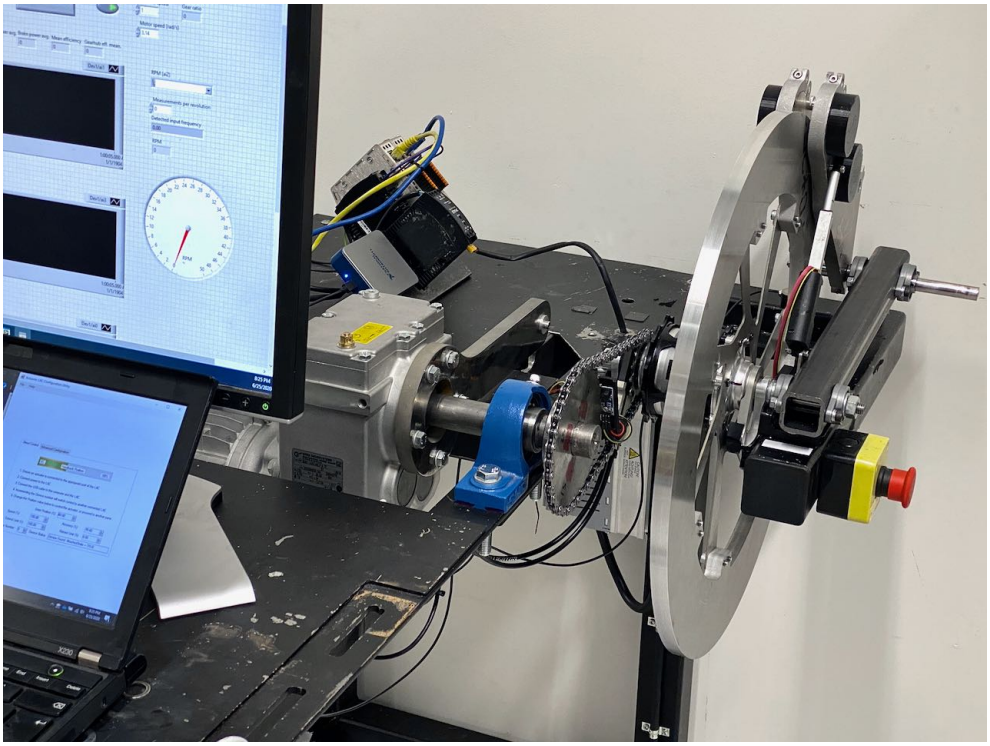

**Figure B.3:** Side-view of the ECB.

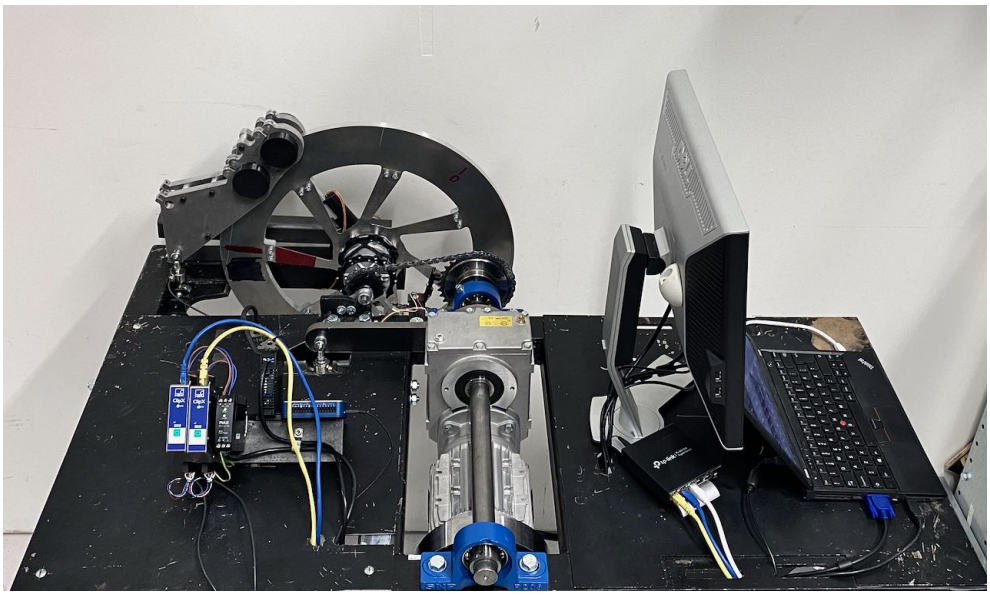

**Figure B.4:** Backside of the testing rig.

## B.2 Friction brake

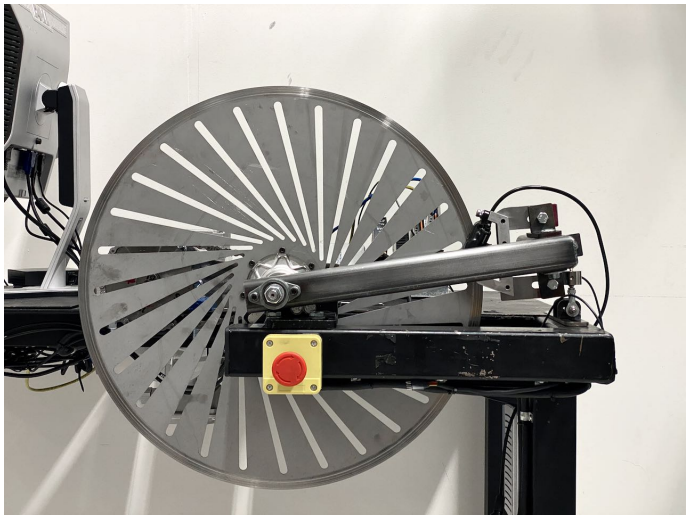

**Figure B.5:** Front view of the friction brake

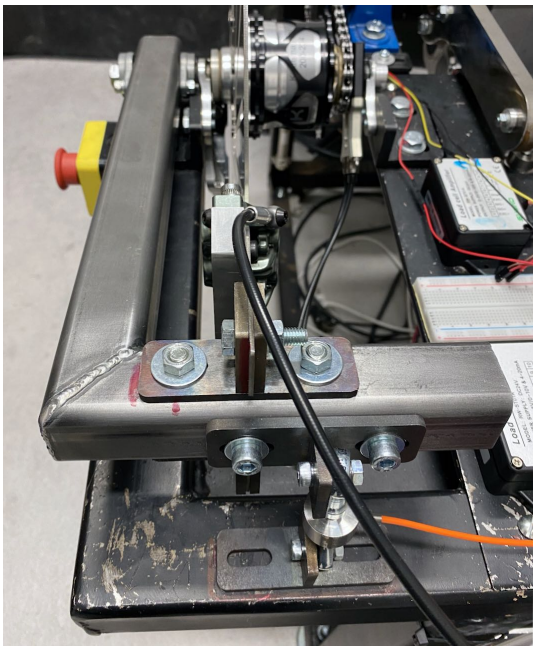

**Figure B.6:** Back view of the friction brake.

## B.3 Other testing rig components

**Figure B.7:** Shifters for the Kindernay XIV mounted to the testing rig.

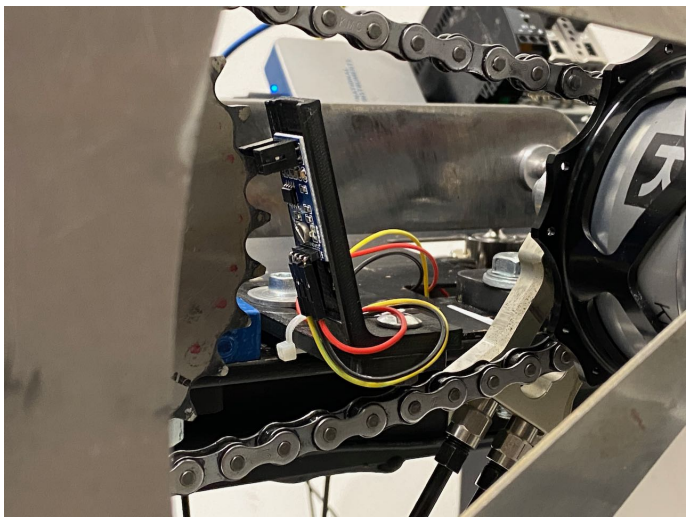

**Figure B.8:** The FC-03 IR speed sensor mounted to the testing rig frame.

# Appendix C

# Simulation results

## C.1 Friction brake arm statics analysis

The deflection in the loading direction is shown in Figure C.1.

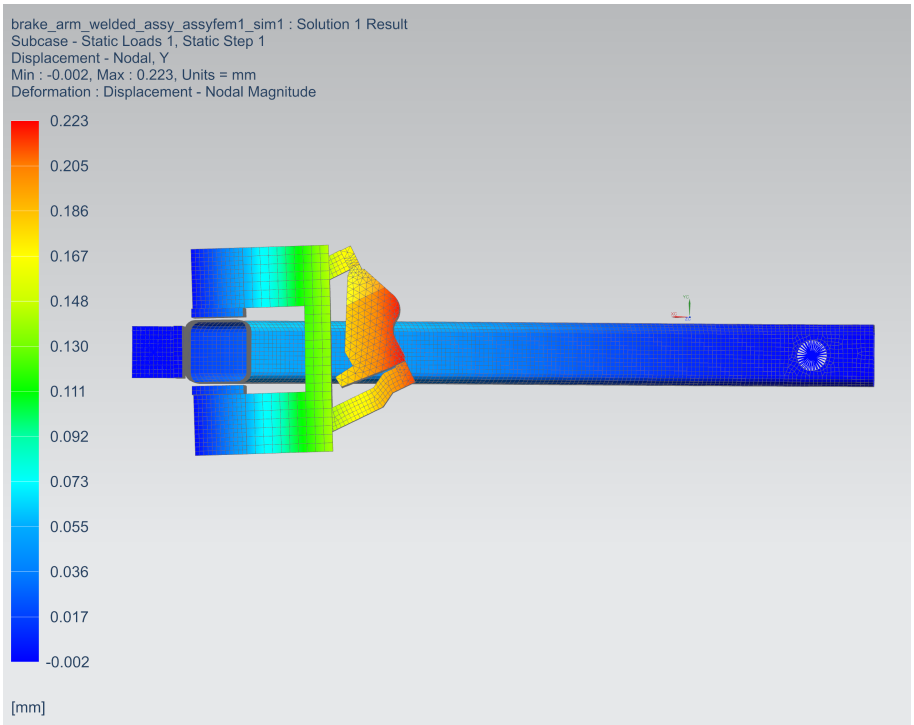


**Figure C.1:** The deflection in the loading direction, shown with 20 times multiplication

## C.2 Brake arm eigenvalue analysis

The first eigenfrequency mode is shown in Figure C.2. The mode shape is also representative for the other frequencies.

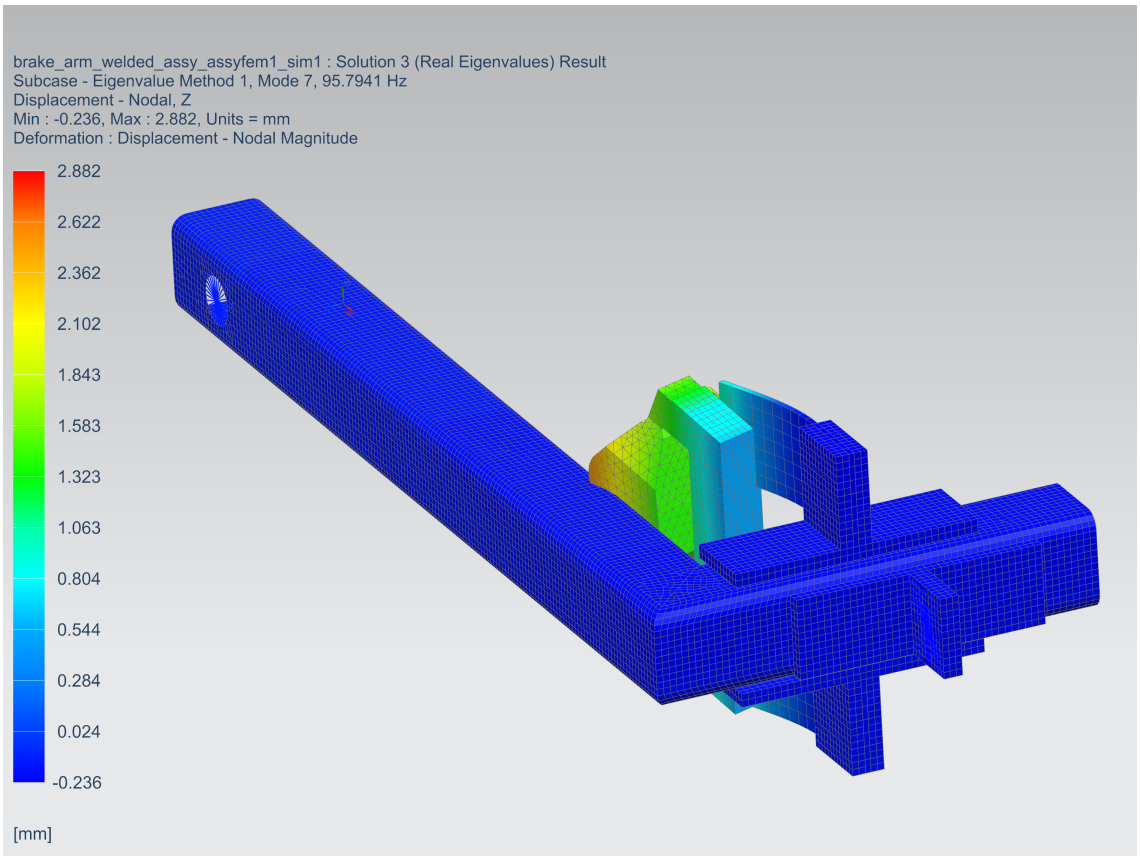


**Figure C.2:** The first eigenfrequency of 95Hz.

## C.3 Frame eigenvalue analysis

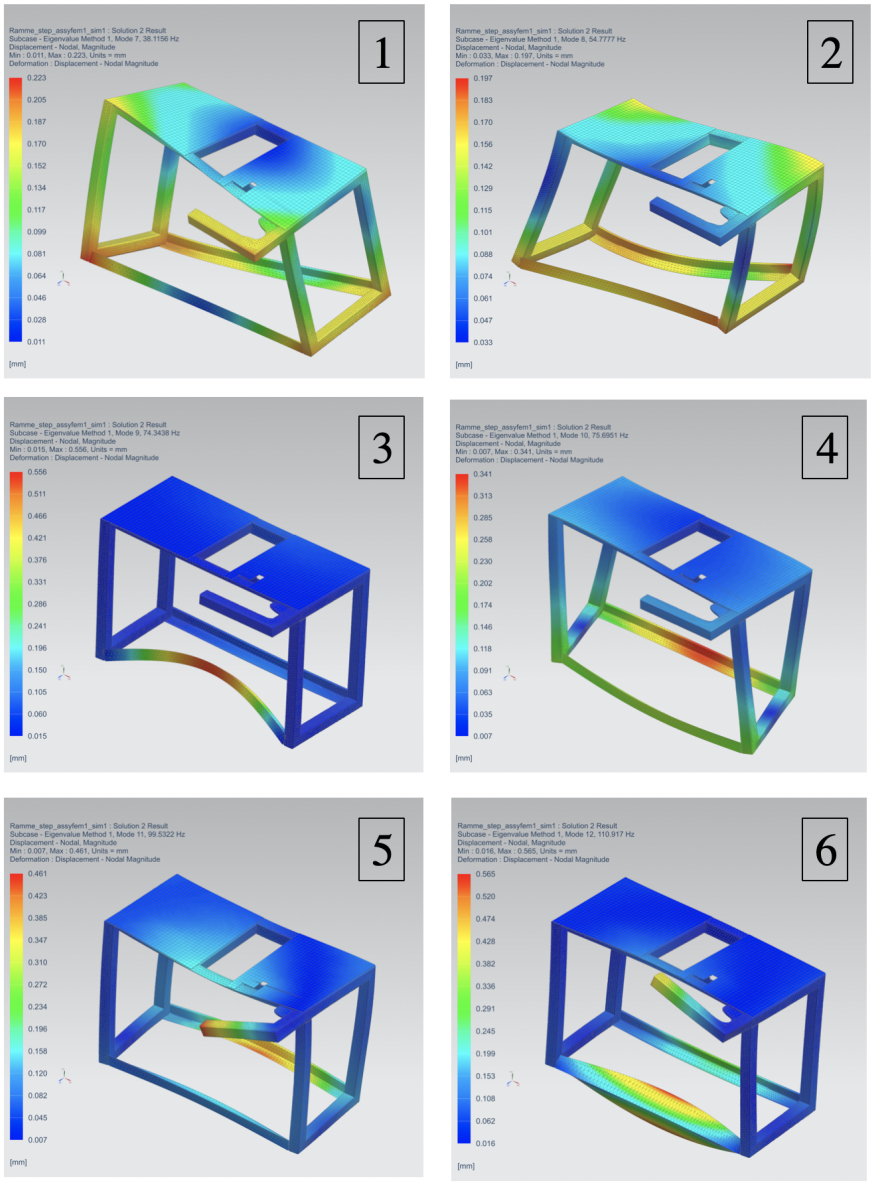


**Figure C.3:** The first six eigenmodes of the testing rig frame: Mode 1: 38Hz; Mode 2: 55Hz; Mode 3: 74Hz; Mode 4: 76Hz; Mode 5: 100Hz; Mode 6: 111Hz

# Appendix D

# LabView Code

The complete LabView code is shown on the next page in Figure D.1.

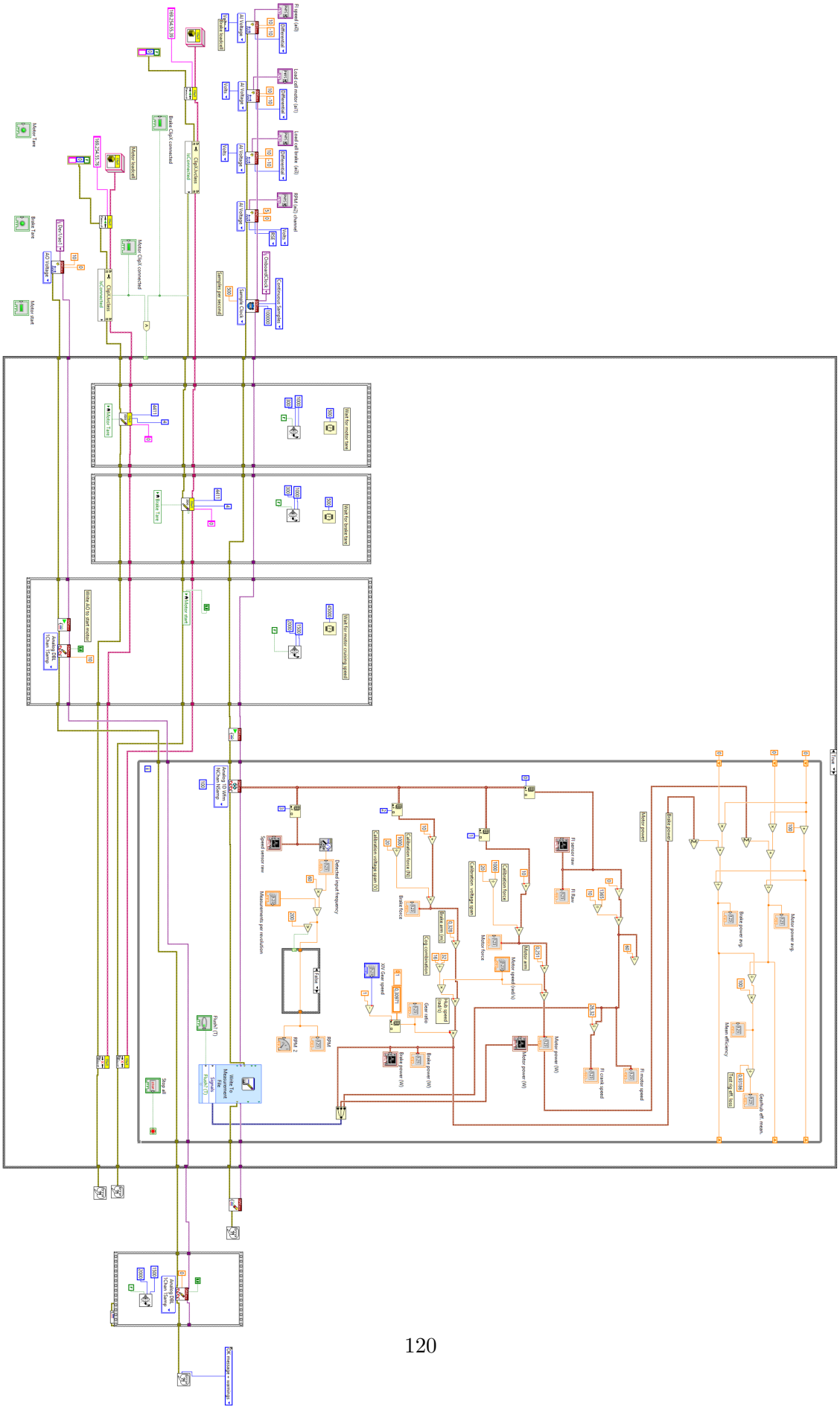

# Appendix E

# Data sheets

Data sheets for the most central parts of the control system can be found via the links below:

- HBM U9C Force Transducer: https://www.hbm.com/fileadmin/mediapool/hbmdoc/technical/B03812.pdf
- HBM ClipX Amplifier: https://www.hbm.com/fileadmin/mediapool/hbmdoc/technical/B04641.pdf
- National Instruments USB-6002 DAQ: https://www.ni.com/pdf/manuals/374371a.pdf

# Appendix F

# Parts drawings

The parts drawings for the following parts are shown on the next pages:

- 10×135 mm adapter
- Motor flywheel
- ECB caliper arm
- 520 mm brake rotor for friction brake
- Friction brake caliper arm (welded)

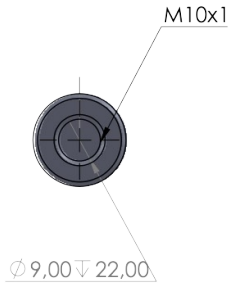


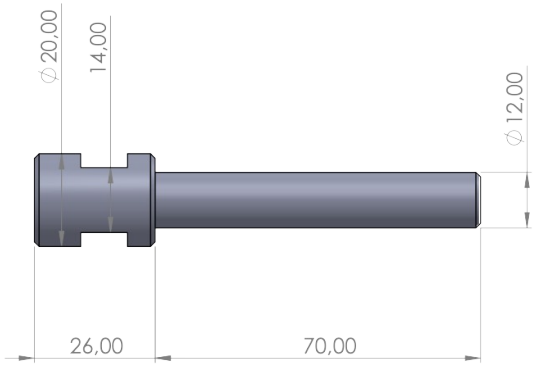


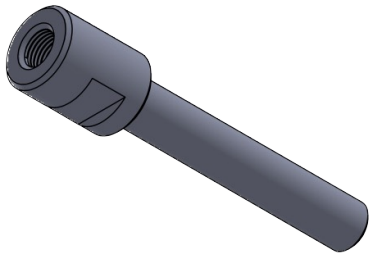

| | | | | | | | |
|---|---|---|---|---|---|---|---|
| UNLESS OTHERWISE SPECIFIED: DIMENSIONS ARE IN MILLIMETERS SURFACE FINISH: TOLERANCES: LINEAR: ANGULAR: | | FINISH: | | DEBURR AND BREAK SHARP EDGES | | DO NOT SCALE DRAWING | REVISION S01 |
| | NAME | SIGNATURE | DATE | | | TITLE: | |
| DRAWN | JDG | | | | | 10x135mm adapter for brake arm | |
| CHK'D | | | | | | | |
| APPV'D | | | | | | | |
| MFG | | | | | | | |
| Q.A | | | | MATERIAL: S355 or similar | | DWG NO. | A3 |
| | | | | WEIGHT: | | SCALE:1:1 | SHEET 1 OF 1 |

Changes in S02: Length of Ø20 H7 hole changed from 7,00 to 6,50mm

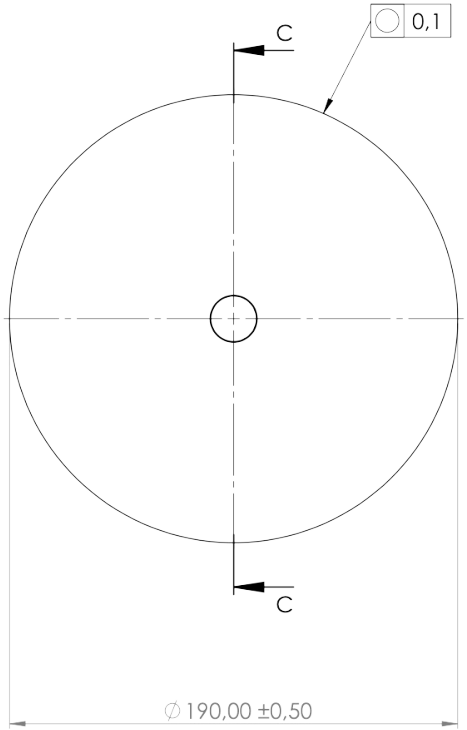


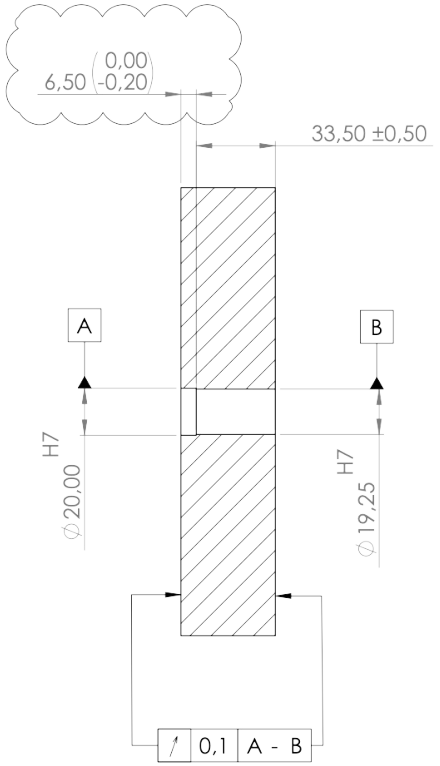


SECTION C-C

| | | | | | | |
|---|---|---|---|---|---|---|
| UNLESS OTHERWISE SPECIFIED: DIMENSIONS ARE IN MILIMETERS SURFACE FINISH: TOLERANCES: LINEAR: ANGULAR: | | FINISH: | | DEBURR AND BREAK SHARP EDGES | DO NOT SCALE DRAWING | REVISION S02 |
| | NAME | SIGNATURE | DATE | | TITLE: | |
| DRAWN | | | | | | |
| CHK'D | | | | | | |
| APPV'D | | | | | | |
| MFG | | | | | | |
| Q.A | | | | MATERIAL: Steel | DWG NO. Motor_flywheel | A3 |
| | | | | WEIGHT: | SCALE:1:2 | SHEET 1 OF 1 |


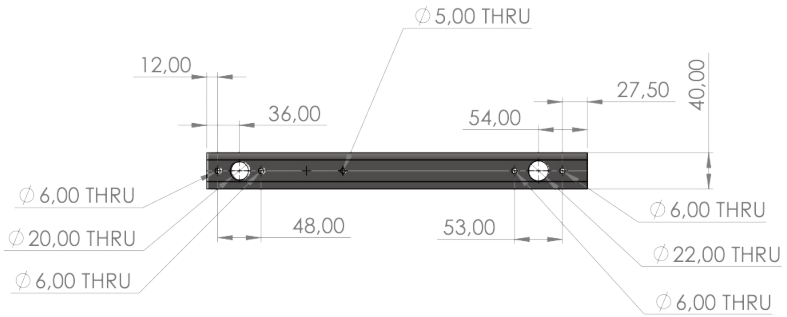


| ITEM NO. | QTY. | DESCRIPTION | LENGTH |
|---|---|---|---|
| 1 | 1 | 40 x 40 x 4.0 | 420 |

| | | | | | |
|---|---|---|---|---|---|
| UNLESS OTHERWISE SPECIFIED: DIMENSIONS ARE IN MILLIMETERS SURFACE FINISH: TOLERANCES: LINEAR: ANGULAR: | FINISH: | DEBURR AND BREAK SHARP EDGES | DO NOT SCALE DRAWING | REVISION | S01 |
| | NAME | SIGNATURE | DATE | TITLE: | |
| DRAWN | JDG | | | Caliper arm for ECB system | |
| CHK'D | | | | | |
| APPV'D | | | | | |
| MFG | | | | | |
| Q.A | | | | DWG NO. | A3 |
| | | | MATERIAL: S355 | | |
| | | | WEIGHT: | SCALE:1:2 | SHEET 1 OF 1 |

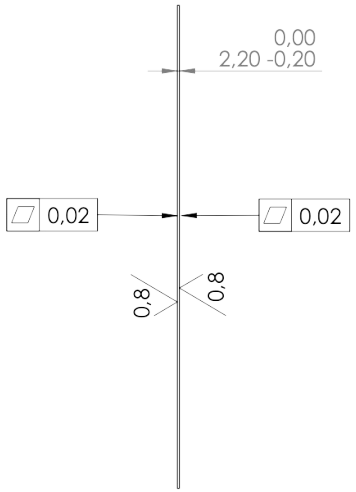


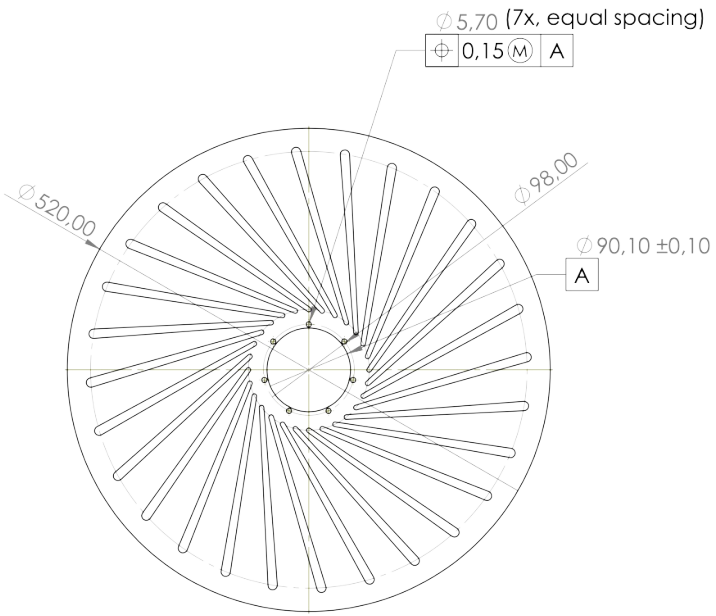


Notes

1 Hardened 35 ± 3 HRC

| | | | | | | |
|---|---|---|---|---|---|---|
| UNLESS OTHERWISE SPECIFIED: DIMENSIONS ARE IN MILLIMETERS SURFACE FINISH: TOLERANCES: ISO2768-1m LINEAR: ANGULAR: | FINISH: | | BROKEN EDGES (R all. 45 ) 0.1-0.5 | | REVISION S01 | |
| | NAME | SIGNATURE | DATE | | TITLE: | |
| DRAWN | JDG | | 4.11.19 | | Brake disc 520mm | |
| CHK'D | | | | | | |
| APPV'D | | | | | | |
| MFG | | | | | | |
| Q.A | | | | MATERIAL: | DWG NO. | A3 |
| | | | | 12Cr13, see note 1 | | |
| | | | | WEIGHT: | SCALE:1:5 | SHEET 1 OF 1 |

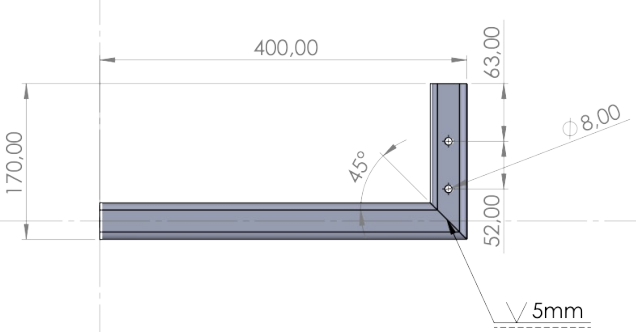


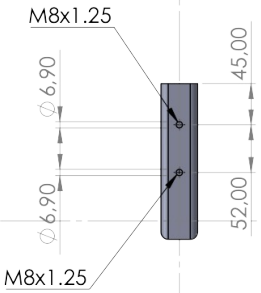


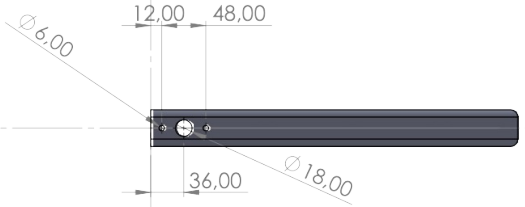


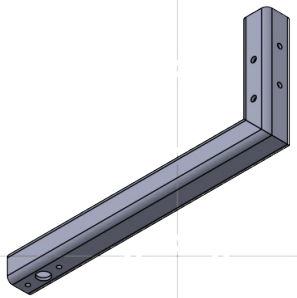

| ITEM NO. | QTY. | DESCRIPTION | LENGTH | ANGLE1 | ANGLE2 |
|---|---|---|---|---|---|
| 1 | 1 | TUBE, SQUARE 40,00 X 40,00 X 4,00 | 400 | 45° | 0° |
| 2 | 1 | TUBE, SQUARE 40,00 X 40,00 X 4,00 | 170 | 0° | 45° |

UNLESS OTHERWISE SPECIFIED:
DIMENSIONS ARE IN MILLIMETERS
SURFACE FINISH:
TOLERANCES:
LINEAR:
ANGULAR:

FINISH:

DEBURR AND BREAK SHARP EDGES

DO NOT SCALE DRAWING

REVISION S01

| | NAME | SIGNATURE | DATE |
|---|---|---|---|
| DRAWN | JDG | | |
| CHK'D | | | |
| APPV'D | | | |
| MFG | | | |
| Q.A | | | |

TITLE:

Brake arm for friction brake

MATERIAL: S355

DWG NO.

A3

WEIGHT:

SCALE:1:5

SHEET 1 OF 1

Jakob Deraas Grimsgaard

# Efficiency Testing of The Kindernay XIV Gearhub

NTNU
Norwegian University of
Science and Technology